Investigating the Photo-Induced Ultrafast Insulator-Metal Phase Transition in Organic $Cu(DCNQI)_2$ Salts by Ultrafast Electron Diffraction

by

Albert Bart Smit

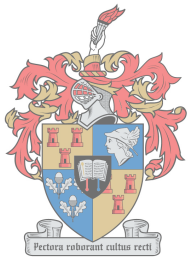

Thesis presented in partial fulfilment of the requirements for the degree of

Doctor of Philosophy

at the University of Stellenbosch

Supervisors:

Prof. Heinrich Schwoerer
Prof. Kristian Müller-Nedebock

March 2018

Declaration

By submitting this dissertation electronically, I declare that the entirety of the work contained therein is my own, original work, that I am the sole author thereof (save to the extent explicitly otherwise stated), that reproduction and publication thereof by Stellenbosch University will not infringe any third party rights and that I have not previously in its entirety or in part submitted it for obtaining any qualification.

Date: March 2018

Abstract

This work presents the structural dynamics of the organic crystal $Cu(DCNQI)_2$ (DCNQI: dicyanoquinonediimine) as it undergoes a photo-induced insulator-to-metal (I-M) transition. $Cu(DCNQI)_2$, a radical ion salt, is a special case of a large π orbital system, which is responsible for anisotropic metal-like conductivity. Such organic molecular solids with delocalised π electrons are materials of interest due to their dynamic, optical, electrical, magnetic, and electro-optical properties; many have already found applications in, for example, organic light emitting diodes (OLEDs), organic field-effect transistors (OFETs), and as future light harvesting materials.

In case of $Cu(DCNQI)_2$, an impressive discontinuous collapse of the one-dimensional conductive phase can occur upon cooling. This is due to a first-order Peierls transition in the presence of strong electron-phonon coupling, which is associated with the trimerisation of crystal layers along the conductive *c*-axis in the (microscopic) lattice structure. We demonstrate that this I-M transition, which is highly tunable by chemical alteration of the molecules' ligands, can be photoswitched within a millionth of a millionth of a second. This makes the material suitable for applications in high-speed optical sensors with outstanding signal response.

We monitor the ultrafast molecular motions responsible for the sub-picosecond lifting of the trimerisation (and therefore the destruction of the insulating phase) in 50 nm thick $Cu(Me,Br\text{-}DCNQI)_2$ single crystals using ultrafast electron diffraction (UED). To capture all lattice dynamics, ultrashort electron probe pulses ($\tau \approx 1$ ps) generated from a 30 kV DC gun are employed to obtain electron diffraction snapshots for different delay times with respect to the ultrashort laser pump pulses ($\tau \approx 150$ fs, $\lambda = 620$ nm), which initiate the transition.

To extract meaningful real-space structural information from our UED data, the effect of small alterations of the known crystalline structure on the electron diffraction patterns are simulated. By comparing these calculations with the dynamics of experimental diffraction signals, the translational movement of the cyano groups was found responsible for the initiation of the I-M phase transition. This translation is unstable, and the insulating phase is restored with a relaxation time of about 6.5 ps. However, when photoexcited close to the M-I phase boundary, an additional translation of the methyl and bromine groups – away from the aromatic ring – is observed. This increase in ligand bulkiness, which causes an internal pressure relief, optically locks the metallic state for timescales greater than 100 ps. We thereby show that an ultrafast, photo-induced, effective internal pressure decrease is required to fully photoswitch and optically lock the metallic conductivity properties. These observations disclose the distinct pathways that ultrafast molecular motions in $Cu(DCNQI)_2$ follow during the I-M transition.

Opsomming

Hierdie werk bied die strukturele dinamika van die organiese $Cu(DCNQI)_2$ (DCNQI: dicyanoquinquinediimine) kristal aan, wat 'n foto-geïnduseerde isolator-tot-metaal (I-M) oorgang ondergaan. $Cu(DCNQI)_2$, 'n radikale ioon sout, is 'n besonderse voorbeeld van 'n groot π-orbitaal stelsel wat verantwoordelik is vir anisotropiese metaal geleidingsvermoë. Sulke molekulêre vastestowwe met gedelokaliseerde π-elektrone is van belang vanweë hul dinamiese, optiese, elektriese, magnetiese en elektro-optiese eienskappe. Menige het al reeds toepassings gevind in byvoorbeeld organiese lig-uitstralende diodes (OLEDs), veld-effek transistors (OFETs) en lig-oestende materiale.

In die geval van $Cu(DCNQI)_2$, kan 'n indrukwekkende diskontinue ineenstorting van die eendimensionele geleidende fase plaasvind tydens verkoeling. Dit is as gevolg van 'n eerste-orde Peierls oorgang in die teenwoordigheid van sterk elektron-fonon-koppeling, wat verband hou met die trimerisering van kristal lae langs die geleidende c-as in die (mikroskopiese) kristalstruktuur. Ons demonstreer dat hierdie I-M-oorgang, hoogs afstelbaar deur chemiese modifikasies van die ligand van die molekule, binne een miljoenste van 'n miljoenste sekonde met lig oorgeskakel kan word. Dit maak die materiaal geskik vir toepassings in hoëspoed optiese sensors met uitstekende seinrespons.

Ons monitor die ultravinnige molekulêre bewegings wat verantwoordelik is vir die sub-pikosekonde eliminasie van die trimerisasie (en dus die vernietiging van die isolasie fase) in 50 nm dik $Cu(Me,Br\text{-}DCNQI)_2$ enkelkristalle met ultravinnige elektron diffraksie (UED). Om al die kristaldinamika op te vang, word ultra kort elektron pulse (τ = 1 ps) – wat gegenereer is in 'n 30 kV DC elektron-geweer – gebruik om elektron-diffraksie patrone te versamel vir verskillende vertragingstye relatief tot die ultra kort laserpomppulse (τ = 150 fs, λ = 620 nm), wat die oorgang begin.

Om betekenisvolle strukturele inligting uit ons UED-data te versamel, is die effek van klein veranderinge aan die bekende kristalstruktuur op die elektrondiffraksiepatrone gesimuleer. Deur hierdie berekeninge te vergelyk met die dinamika van eksperimentele diffraksie seine, is die translasie beweging van cyano groepe verantwoordelik gevind vir die inwerkingtreding van die I-M-fase-oorgang. Hierdie translasie is onstabiel en die isolerende fase word herstel met 'n ontspanningstyd van ongeveer 6.5 ps, maar wanneer die oorgang naby die M-I-fase grens ge-fotostimuleer word, word 'n addisionele translasie van die metiel- en broomgroepe – weg van die aromatiese ring – waargeneem. Hierdie toename in ligandgrootte, wat 'n interne drukvermindering veroorsaak, omsluit die metaalfase opties vir tydskale groter as 100 ps. Dit toon aan dat 'n ultravinnige, foto-geïnduseerde, effektiewe interne drukvermindering nodig is om die metaalgeleidings-eienskappe heeltemal te verander en opties te sluit. Hierdie waarnemings openbaar die unieke paaie wat die ultravinnige molekulêre bewegings in $Cu(DCNQI)_2$ volg tydens die I-M-oorgang.

Acknowledgements

I would like to acknowledge:

- Prof. Heinrich Schwoerer for his continued excellent supervision during both my MSc and PhD in the past 5 years. His enthusiasm, guidance and deep involvement created a great environment for the successful completion of this project.
- Nancy Payne, with who I did most of the experiments that are presented in this work, and who helped with proof-reading this thesis. Without her loyalty and continued programming and microtoming support, this work would not have been possible.
- Our collaborators from Würzburg (Dr. Florian Hüwe and Prof. Jens Pflaum) for synthesising the samples, and for the scientific discussions and feedback during this project.
- Dr. Stuart Hayes for introducing me to electron diffraction simulations.
- Prof. Catherine Esterhuysen for taking her valuable time to introduce me to software that can display and manipulate structure files that were obtained from X-ray crystallography.
- All UED colleagues who have come and gone over the years and have contributed to this work in some other way (Dr. Olufemi Olaoye, Andrea Rohwer, Aminat Suleiman, Max Heck, Dr. Nicolas Erasmus, Dr. Kerstin Haupt).
- My other SARChI friends who made the group fun, both academically and socially (Neway, Iulia, Essraa).
- The Laser Research Institute (LRI) for scientific support, the departmental workshop (in particular Gerhard Louwrens and Lawrence Ashworth) for technical support, and the department for administrative support.
- My family and friends and especially my parents for their continued support in every possible way.
- Lungile for her love and support.

Dedications

This thesis is dedicated to
Lungi

Contents

1. Introduction

Organic molecular solids of amorphous, ordered or crystalline composition have gained the attention of physicists in view of some of their peculiar thermal, mechanical and electronic properties. Since the first half of the 20^{th} century, a wide variety of molecular crystals have been synthesised. The remarkable ability of molecules to assemble into structures that are highly ordered, such as single crystalline materials, can for example be utilised to determine the structure of those molecules by means of X-ray crystallography experiments. A pure and three dimensionally periodic crystal is required in order to solve the structure of the arrangements of atoms within a molecule. As a result of the ongoing efforts to succesfully crystallise organic molecules, the structure of complex molecules such as proteins has been resolved. Despite the molecules being 'trapped' in crystalline forms (held together in a 'soft' solid), reliable structures of the molecules are obtainable: molecules retain their own identity due to the intermolecular forces being significantly weaker than the intramolecular forces (such as covalent bonds), resulting in bond lengths and valence angles to remain the same[1].

While structural determination is an important reason to synthesise molecular crystals, much more can be gained. Correlated arrangement of molecules in crystals aid in interactions such as hydrogen bonding, dipole-dipole interactions (e.g. the van der Waals force), Coulomb attraction, and π-orbital overlap, which in turn give rise to a variety of dynamic, optical, magnetic, electrical and electro-optical properties. In particular, the delocalised π-orbitals in planar molecules – an interaction not present in inorganic solids but unique to arranged molecular solids – are responsible for exotic phenomena.

The usefulness of conjugated π-electrons in arranged organic molecular solids is perhaps not unexpected: taking biological systems as an example, it becomes clearly evident that π systems play a crucial role. For example, arrays of proteins and chlorophyll molecules with delocalised π-orbitals in biological antenna complexes (such as light-harvesting complexes) allow for a highly efficient transfer of the energy obtained from photons to a reaction center. So undoubtedly, there is a strong case for interesting and important fundamental physics investigations in these types of materials. Moreover, the advantage of combining complex molecular physics with solid state physics, allows for an exiting area of unexplored science that benefits from a strong connection between experimental, theoretical and numerical studies. Many organic molecular solids have already found large scale commercial applications as organic light emitting diodes (OLEDs), and are increasingly used as light harvesting materials in organic materials.

Interatomic Forces Planar polyacene molecules are a good example of conjugated π-electron systems, where the 2s and 3p atomic orbitals of the carbons undergo sp^2 hybridisation to form molecular orbitals: three covalent σ-bonds in the plane of the

molecules containing carbon atoms are created (figure 1.1a), leaving the fourth orbital (p_z) – which is oriented perpendicular the plane of the molecule (figure 1.1b) – unchanged. This allows for overlap of the p_z orbitals of the carbons, leading to a π-bond with delocalised electrons along the plane of the benzene ring (figure 1.1c). The size of the π orbital grows with the size of the polyacene chain, with π electron delocalisation along the entire molecule (figure 1.1d).

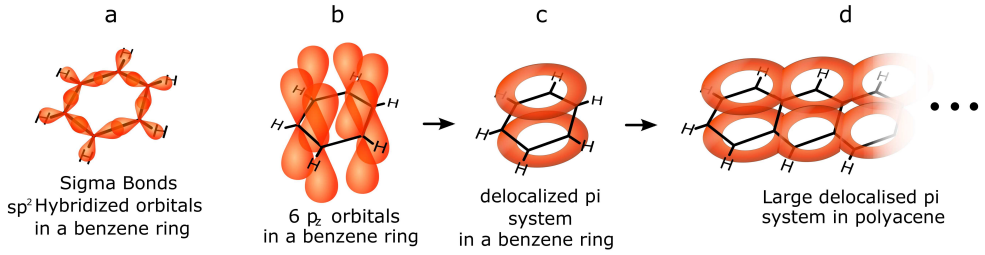

Figure 1.1: (a) Planar σ-bonds in benzene. (b) p_z orbitals sticking out perpendicular to the molecular plane. (c) The p_z orbitals overlap, forming a π orbital. (d) In polyacene (benzene, naphthalene, anthracene, tetracene, pentacene, hexacene, and heptacene for 1 – 7 rings respectively), the π electrons are delocalised along the entire molecule. This image is adapted from ref. [2].

The close packing of molecules (for example in crystals), allows interactions between many molecules with consequential properties that are not intrinsic to the isolated molecules. To understand the effects of intermolecular forces, it is important to discuss their influence on energy levels in molecules. Firstly, a schematic example of two energy levels in a molecule is given in figure 1.2a, namely the highest occupied molecular orbital (HOMO) and the lowest unoccupied molecular orbital (LUMO). In the ground state, all electrons of a molecule occupy the HOMO and the orbitals below, while the LUMO and all orbitals with higher energies are vacant. The energy level diagram in case of a semiconductor, as sketched in figure 1.2b, consists of continuous energy bands. The valence band (which is full in the ground state) and the conduction band (which is empty in the ground state) are sketched in figure 1.2b. A band gap – the difference between the valence band maximum (VBM) and the conduction band minimum (CBM) – separates the two bands. The band gap energy E_g is the minimum amount of energy required to excite electrons from the valence band into the conduction band, with the Fermi energy level E_F in between the two (by definition). Materials are semi-conducting when electrons can be thermally excited into the conduction band (i.e. $E_g \leq \mathrm{k}T$, while for insulators $E_g \gg \mathrm{k}T$). Once in the conduction band, the electrons are free and an electrical current can flow if an external electric field is applied. Lastly,

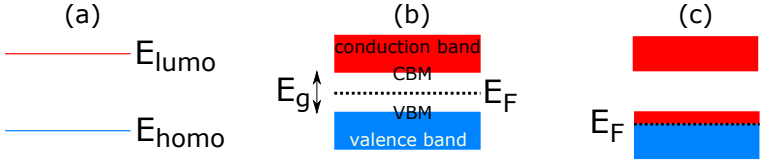

Figure 1.2: (a) Energy levels of highest occupied molecular orbital and lowest unoccupied molecular orbital for an isolated molecule. Blue indicates occupied states at T = 0 K, whereas red indicates unoccupied states. (b) The valence and conduction band in a semi-conductor, separated by a band gap. (c) The band structure of a metal, where the highest occupied band is not full.

in metallic materials (fig. 1.2c) the highest occupied band is not full and electrons can move freely. In this case, the band is filled up to E_F at T = 0 K.

To determine the orbital energy level diagrams in molecular crystals (like the example case of figure 1.2a), absorption spectroscopy in the infra-red, visible and ultraviolet range (or Raman spectroscopy) are applied. When the energy of incoming photons matches the transition energy from a lower orbital to a higher orbital, an absorption peak is observed.

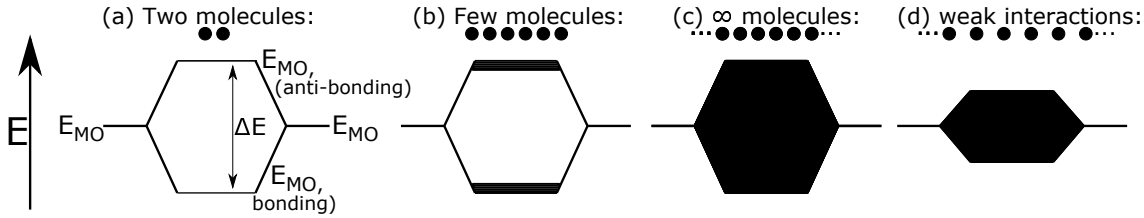

Figure 1.3: (a) Overlap of Molecular Orbitals (MO) of two molecules, resulting into orbital splitting. (b) When several molecular orbitals with the same energy level overlap, the bonding and anti-bonding levels are broadened. (c) With infinite molecules along a chain, the molecular orbital turns into a band. (d) Weaker intermolecular forces lead to narrow bands.

The HOMO energy level shown in figure 1.2(a) is a narrow line with zero bandwidth in the case of isolated molecules, as no interactions with other molecules are present. When two (identical) molecules are sufficiently close, the two corresponding molecular orbitals (with energy level E_{MO}) overlap and split into two, a concept that is displayed in figure 1.3a. The more molecules that are added to the chain, the more energy levels that are created due to hybridisation (fig 1.3b). If the number of molecules along the chain is infinite, the molecular orbital energy levels of isolated molecules turn into bands (illustrated in figure 1.3c). The width of the formed band depends on the strength of the interactions, with lower forces leading to narrower bands (figure 1.3d). The formation of bands in (inorganic) solid materials due to inter*atomic* overlap is well-known, but the formation of narrow bands due to small inter*molecular* forces, such as π orbital overlap, is unique to molecular crystals. Orbital overlap (and equivalently band formation) in molecular crystal can cause an infinitely large delocalised π orbital. In the previous example of polyacene, adding an infinite number of aromatic rings would turn the molecular orbitals into bands. Or, alternatively, when molecules are closely packed in a crystal (for example in tetracene crystals), where π orbitals of individual molecules are also able to overlap with one another, one big 'macromolecule' can essentially be formed.

The HOMO in organic molecules is generally full, leaving no state for conductivity. So the majority of organic crystals (with π-orbital overlap) are not conducting. However, if for some reason, the highest band is not full (for example in the case where an electron-donating cation partially fills the LUMO of an electron-accepting anion in an organic molecular salt), conductivity can occur.

Variability of Crystal Properties The variety of possible crystal compositions, and therefore the range of strengths of intermolecular interactions and variety of crystal properties, is huge. Crystals can be purely organic containing either molecules from the same species, or a mix of different species, or a combination of a molecule with a metallic cation (organo-metallic salts). What makes molecular crystals exciting compared to

classical inorganic counterparts is the variability of the molecular structures, such that conductivity properties (e.g. the crystal being an insulator, semiconductor, metal or superconductor) can meet certain requests. The chemical composition of molecules in a crystal is highly changeable (atoms and side chains can be changed, for example, or hydrogens can be deuterated, etc), allowing for the engineering of crystals by selecting building crystals that are suitable for applications[3].

To gain a better understanding of π systems in molecular crystals that have planar molecules as building blocks, let us take the example of the radical ion salts of Cu(2,5-R_1,R_2-Dicyanoquinonediimine[1]) (abbreviated as Cu(DCNQI)$_2$), which is the system of investigation of this thesis. Three layered DCNQI molecules – which are tetrahedrally coordinated around the copper ions – are sketched in figure 1.4 (a full structure and more properties of this material will be discussed in chapter 2). The aromatic ring, as discussed in the case of polyacene, has π-orbitals pointing perpendicular to the molecular plane. Unlike polyacene (where π electrons are delocalised *parallel* to the molecular plane), in this special case, the π electrons are delocalised along the direction *perpendicular* to the molecular plane, along the aromatic compounds stacked on top of each other. This ultimately leads to the formation of a large channel-like π-orbital that reaches through the entire crystal domain. The π electrons are delocalised mainly along the stacking direction (which in this case is the crystal c-axis) of the entire macroscopic crystal domain, which in reality are needles of up to many centimetres long. In general, salts with π-orbital overlap tend to crystallise such that the overlap of the highest occupied π-orbital with that of neighbouring molecules is maximised, promoting the creation of such large π systems.

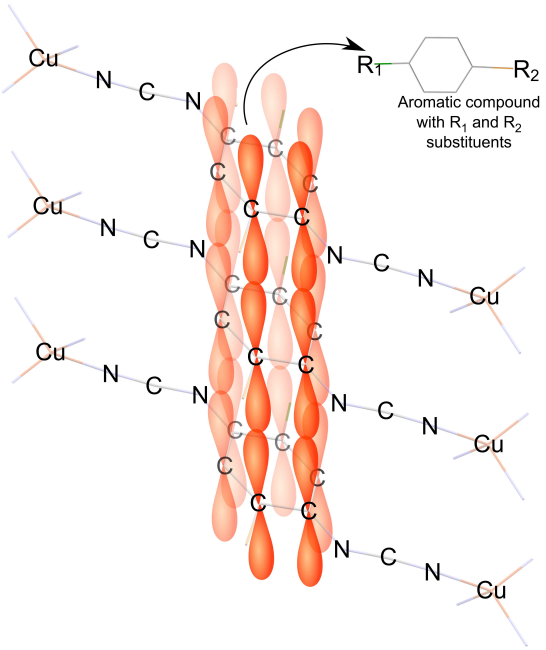

Figure 1.4: Sketch of the unhybridised π orbitals of the aromatic ring in Cu(DCNQI)$_2$. Hybridisation of these orbitals leads to a large one-dimensional, channel-like π system, that reaches through the entire crystal domain. The degree of orbital mixing can be tuned by chemically altering the R_1 and R_2 rest groups (top-right inset).

When taking the orientation of the two aromatic rings in figure 1.4 into consideration, it can be argued that near-neighbour interactions between the DCNQI molecules can be adjusted if the angle/orientation of molecules are modulated: the efficiency of the overlap of the π-orbitals perpendicular to the aromatic ring can be altered by changing chemical compounds, for example the rest groups (labelled R_1 and R_2) on the aromatic ring. This enables the 'engineering' of physical crystal properties, as the useful anisotropic conductivity (which will be discussed in chapter 2) can be tuned and tailor-made.

[1] dicyano indicates the two ·NCN wings on both sides of the benzene ring, quinone indicates the aromatic compound, and diimine indicates two (highly variable) R_1,R_2 side groups attached to the benzene ring.

Examples and Applications A few intriguing examples of peculiar properties in molecular crystals are the following. The previously discussed tetracene and pentacene are semi-conducting materials when crystallised. Excitons are generated upon absorption of photons in the visible or UV range, with high carrier mobility values[4]. The binding energy of these excitons (0.1 to 1 eV) is relatively low compared to most molecular crystals, where in many cases excitons are confined within the molecule. These so-called Frenkel excitons in tetracene and pentacene thus have larger exciton mobilities. This makes the materials competitive with silicon micro-electronics, with possible applications in thin-film transistors and organic field-effect transistors (OFETs).

Phthalocyanine (Pc) and derivatives, which are aromatic macrocyclic compounds, are used as artificial organic pigments because of their high absorption in the visible to near-infrared range, and the flexibility to change the absorption wavelength by adjustment of ligands. CuPc, for example, is used in textile dyeing and paper industry, or as a pigment for other artistic purposes. Due to efficient charge and energy transfer between π-orbitals in their ordered layers, Pcs also operate as donor materials in molecular electronics, such as OFETs, organic solar cells and they find applications in optical devices like light emitting diodes (OLEDs)[5].

Molecular crystals may also exhibit ferromagnetic properties below a critical temperature, in for instance molecule based metal-organic magnets that bear unpaired electron spins in the d or f orbitals of the isolated metal atoms, or p orbitals of the organic species. Metal-organic compounds related to Prussian Blue (Fe_7CN_{18}), a dark blue pigment, are known to exhibit these properties[6]. Some Prussian Blue derivatives show photo-induced magnetism[7], an interesting subject for ultrafast studies. Purely organic metal-free magnets can also show ferro-magnetism, like p-nitrophenyl nitronyl nitroxide ($C_{13}H_{16}N_3O_4$)[8].

The typically weak cohesion energies of molecular crystals enhance the likelihood of the crystals to adopt different structures. The phenomenon called conformational polymorphism[9] is the ability of the same building blocks of a crystal to manifest in different crystalline ordering. For example, the standard Bechgaard-Fabre Salts (BFS) is triclinic, but for certain synthesis conditions, the monoclinic phase can be obtained. It is usually not predictable which space group a crystal will take up for which synthesis procedure. It is not unusual that a crystal structure has been reported in literature, but subsequently 'disappeared', as no one has been able to reproduce it. Different structures of the same crystal may also be reversibly accessible by inducing a phase transition by changing external conditions such as temperature, pressure, and exposure to photons.

Molecular Metals Molecular crystals may also exhibit high (metal-like) conductivities. In 1911, McCoy and WC Moore predicted the possibility of preparing composite metallic substances from non-metallic constituent elements when they produced promising results on tetramethylammonium-mercury amalgams[10]. The first stable complex with high conductivities (1 $\Omega^{-1}cm^{-1}$) was the perylene-bromine complex synthesised in 1954[11]. This example marks the beginning of an extraordinarily interesting ongoing research effort in conducting organic materials, inciting research interests with good results. Much of the work directly following that, until to date, is on conductive perylene, with many derivatives successfully synthesised and thoroughly characterised. To date, there is only one single-component (crystal made up of a single building block) metallic molecular crystal: $Ni(tmdt)_2$[12].

Besides metallic, molecular organic superconductors (all below 15K) also exist, the first one being $(TMTSF)_2PF_6$ discovered in 1980[13]. Ever since, numerous molecular superconductors have been reported, such as the previously mentioned BFS, which is superconducting at high pressure and low temperature conditions.

As mentioned, when one crystal building block in a molecular crystal with π-orbital overlap acts as an electron donor, and another as an electron acceptor, charge transfer can promote crystallic conductivity[14]. A well studied organic conductor is monoclinic TTF-TCNQ, a charge transfer salt first synthesised in 1973[15]. The planar molecules themselves are insulating, but one dimensional conductivity occurs due to partial charge transfer from the TTF HOMO to the TCNQ LUMO, combined with π-orbital mixing along the stacked planar molecules. The charge transfer facilitates the separation of electrons and electron holes, such that they can travel along the TCNQ and TTF columns.

$Cu(DCNQI)_2$ The previously discussed $Cu(DCNQI)_2$ is also a good example of a 1D conductor, due to its delocalised electrons along the crystal *c* axis (figure 1.4). As will be discussed in chapter 2, the DCNQI LUMO is partially filled by the Cu 3d, resulting in high conductivity. With (undeuterated) methyls as R_1 and R_2 rest groups, $Cu(DMe\text{-}DCNQI)_2$ is metallic down to 5 K with a conductivity up to 500.000 S cm^{-1}[16], similar to the room temperature conductivity in copper ($6{\cdot}10^5$ S cm^{-1}), one of the best organic conductors. By replacing the methyls at the R_1 and R_2 positions with smaller units such as deuterated methyl, Br, Cl, or combinations, the crystal exhibits a dramatic phase transition whereby the conductive phase collapses upon cooling. This first order Peierls transition causes an enormous discontinuous drop in conductivity of more than 11 orders of magnitude (in the most extreme case). This very special property, particularly pronounced in $Cu(DCNQI)_2$, is a phenomenon that will be discussed in depth in chapter 2.

The impressive phase transition involves an alteration of electronic band structure as well as atomic structure, and is tunable by external and internal pressure, and it can be triggered by absorption of light. In this thesis, we show that when photo-excited with a light pulse, a $Cu(DCNQI)_2$ crystal can be switched from a glass-like insulating system to being a good conductor, within a millionth of a millionth of a second. This remarkable behaviour provides potential for applications in opto-molecular electronics and poses fundamental questions concerning the driving forces, the selectivity and the ultimate speed of these macroscopic transitions. To answer some of these questions, we apply ultrafast, time resolved electron diffraction in the picosecond range to the photo-induced insulator-to-metal transition in $Cu(Me,Br\text{-}DCNQI)_2$, allowing us to observe the structural degrees of freedom while the system undergoes the phase transition.

Chapter 2 of this thesis starts off with an in-depth review of $Cu(DCNQI)_2$. Chapter 3 continues by describing our preferred experimental method for investigating the photoinduced ultrafast structural changes, namely ultrafast electron diffraction (UED). The experimental conditions and a characterisation of experimental specifications are given. Subsequently, chapter 4 aims to present the results of our experiments and the analysis procedures and methods used to interpret the data. Here, our interpretation of the results is presented. To conclude, a summary and an outlook on future structural molecular dynamics experiments is given in chapter 5.

2. The Organic Radical Ion Salt M(R_1,R_2-Dicyanoquinonediimine)$_2$

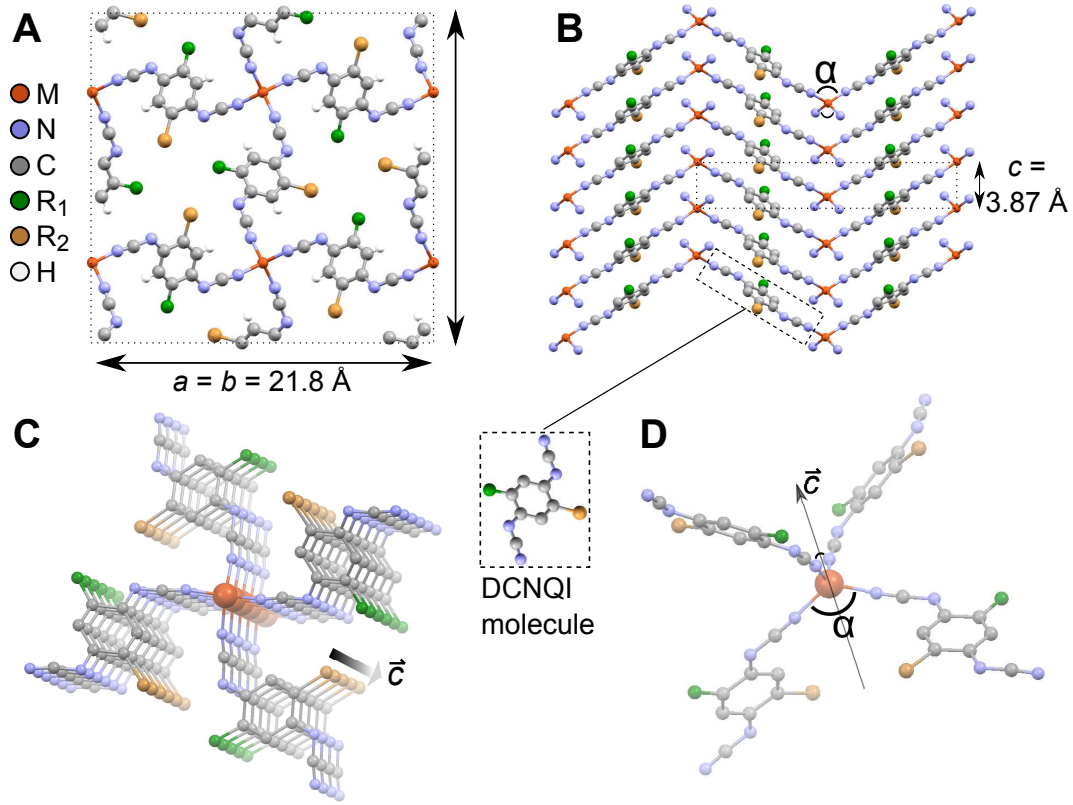

Figure 2.1: (a) Top view (a,b plane) and (b) side view (a,c = b,c plane) of the Cu(DCNQI)$_2$ crystal structure. (c) 3D view of the stacking along $\vec{c}$ (into the page) of the tetrahedral planes (d).

2.1 Introduction

M(R_1,R_2-Dicyanoquinonediimine)$_2$ (abbreviated M(R_1,R_2-DCNQI)$_2$ or simply M(DCNQI)$_2$) is an organic radical ion salt. A top view of the crystal structure along the a and b crystal axes is shown in figure 2.1a. Here, the negatively charged molecular DCNQI anions are coordinated around a central positively charged metallic ion M in a slightly distorted tetrahedral fashion. The stacking of these crystal layers along the a,c (or equivalently b,c) direction, with layers separated by the crystal constant c, is shown in figure 2.1b. Two three-dimensional views of the distorted tetrahedral structure are shown in figure 2.1c and d. The most important distortion parameter, the N–Cu–N angle α, is shown in figure 2.1b and d. For a perfect tetrahedron, $\alpha = 109.5°$, whereas for M(DCNQI)$_2$ $\alpha \approx 122 - 127°$.

Compounds of M(R_1,R_2-DCNQI)$_2$ can consist of M = Cu, Ag, Li, Na, K, Tl and NH_4, while restgroups R_1 and R_2 can consist of CH_3 (= Me), MeO, Cl, Br and I, or combinations thereof. Although the chemical variability of this material is huge, all compounds are isomorphous (space group $I4_1/a$), with the changing of ligands only leading to minor deformations. Here, the variability of the α angle for different compositions (and temperature, and external pressures) turns out to be the important parameter governing the interesting electronic properties of these salts.

The first M(R_1,R_2-DCNQI)$_2$ compound that was synthesised was Cu(2,5-DM-DCNQI)$_2$ – where DM stands for di-methyl – in 1986 by Aumüller et. al.[16]. The material received a lot of attention as being the best organic conductor at the time (σ = 500.000 S cm^{-1} at 3.5 K). As was previously shown in figure 1.4, the large anisotropic conductivity is facilitated by the delocalisation of π electrons along the c axis of the entire crystal domain.

In the years following the discovery of the material, numerous papers on a wide range of new physical properties of M(R_1,R_2-DCNQI)$_2$ salts were published, by synthesis of many chemical compounds. Thereby, full advantage of the large variability of the metallic cation and the variability of the R_1,R_2 substituents on the DCNQI acceptor molecule was taken. Of particular interest are the M = Cu compounds [Cu(DCNQI)$_2$], as some of these show dramatic first-order metal-to-insulator phase transitions upon cooling or under pressure (while the M≠Cu salts show a second-order transition, see appendix A.1 for more information). In the extreme case of figure 2.2, the conductivity discontinuously drops many orders of magnitude upon cooling. In this particular example, the crystal even shows a reentry to the conductive phase at lower temperature. The hysteresis (that is the shift in transition temperature for heating compared to cooling) is indicative of the first-order character of this transition.

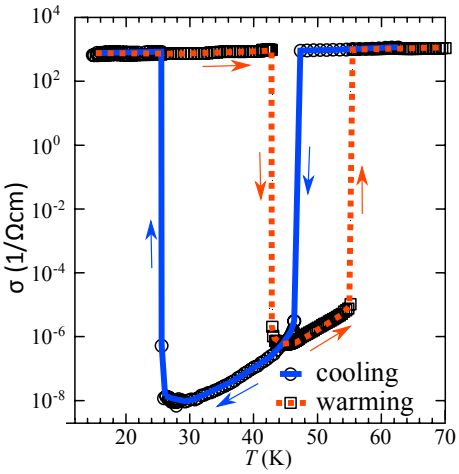

Figure 2.2: Temperature dependent conductivity of Cu(DMe-DCNQI)$_2$ (30% of the hydrogens on DMe are deuterium), taken from ref [17].

The dramatic drop in conductivity of some M(R_1,R_2-DCNQI)$_2$ compounds (a macroscopic property) is associated with a change in the atomic crystal structure (a microscopic property), namely the doubling of the unit cell along the c-crystal axis for M ≠ Cu (figure 2.3a), and the tripling of the unit cell for M = Cu (figure 2.3b).

In diffraction experiments, the reciprocal space of the lattice structure is detected. Therefore, the dimerisation and trimerisation, leading an additional (longer) period in real space, is observed in a diffraction pattern by an additional shorter period. In our home-built electron diffractometer (which will be characterised in chapter 3), we have observed the superstructure in the case of a trimerisation in Cu(Me,Br-DCNQI)$_2$ by the appearance of $c^*/3$ satellite peaks below T=155 K, which is shown in figure 2.3c. The dimerisation and trimerisation in M(DCNQI)$_2$ compounds were first observed in X-ray diffraction experiments[18, 19].

The existence of these $2c$ and $3c$ superstructures are due to the formation of a Charge Density Wave (CDW) and Periodic Lattice Distortion (PLD), which is discussed next.

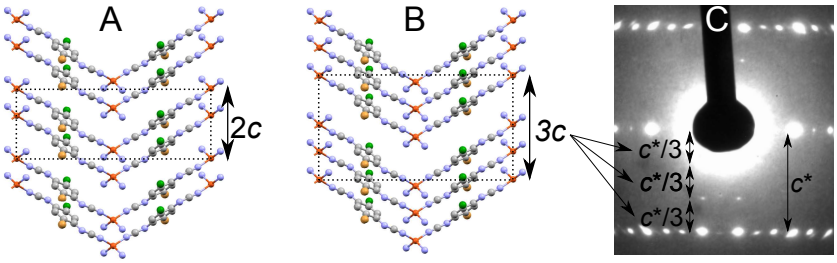

Figure 2.3: (a) Sketch of a $M(DCNQI)_2$ dimer for M $\neq$ Cu, and (b) a trimer for M = Cu. Note that superstructures are illustrative and do not represent the real low temperature structures (as they are unknown). (c) In our home-built electron diffractometer, the trimer in $Cu(Me,Br\text{-}DCNQI)_2$ is observed by $c^*/3$ satellite peaks.

2.2 Charge Density Wave formation

The formation of a CDW/PLD is a rather complex process. Despite 40 years of ongoing research about the origin, and the structural and electronic properties of the CDW/PLD formation, their formation can not be accurately predicted[20]. However, fortunately, an intuitive explanation for their formation can be given based on simple models. The *free electron model* (or Drude model) is used to describe properties of metals. In this model, a 'sea' of free electrons within a metal do not interact with each other, the periodic lattice of the cores of the atoms, or anything else (i.e. the potential, $U(x)$ is zero). The solution of the Schrödinger equation for such a free electron is a plane wave, with its kinetic energy given by:

$$E = \frac{\hbar k^2}{2m}. \tag{2.1}$$

This solution for the energy in reciprocal k-space, which is a parabola, is sketched by the dashed line in figure 2.4c. This simple model successfully explains properties such as heat capacity, electric and thermal conductivity, but fails to explain phenomena like insulation and semi-conductivity. To include these phenomena, the concept of energy bands needs to be introduced, as was previously discussed in the introduction of this thesis (in particular in figure 1.2). This is successfully done by extending the model to the *nearly-free electron model* (Drude-Sommerfeld model), which introduces a periodic potential to which the 'sea' of electrons are subjected. The potential arising from a one-dimensional chain of atoms, with period c – sketched in figure 2.4a – would be $U(x) = U(x + c)$. The electron density distribution (ρ) is assumed to be uniform (fig. 2.4b). Now, a correlation between the lattice and the free electrons is introduced, which causes the energy dispersion curve to be repeated along k, with a period of $2\pi/c$ (Bloch's theorem)[21]. This is shown by the dotted plots in figure 2.4c, where three parabolas are repeated in k-space with a period of $2\pi/c$. At $k = \pi/c + n$ (where n is an integer), states would overlap in energy and would therefore be *degenerate*. In the approximate solution near such a zone boundary, this degeneracy is lifted by – firstly – the raising of energy for states above the overlap, and – secondly – the lowering of energy below the overlap in the dispersion curve (shown in the figure 2.4c with the solid line). The result is an energy region with no available state, indicated with the shaded area. Electrons are forbidden to occupy energies in this band, which is the previously introduced *bandgap*.

In the energy dispersion curve shown in figure 2.4c, the Fermi energy level (E_F) is

indicated. In k-space, the k-value where the dispersion curve crosses E_F is defined as k_F. The vector pointing along positive k with magnitude k_F, indicated with the blue arrow, is defined as the Fermi vector, $\vec{k_F}$.

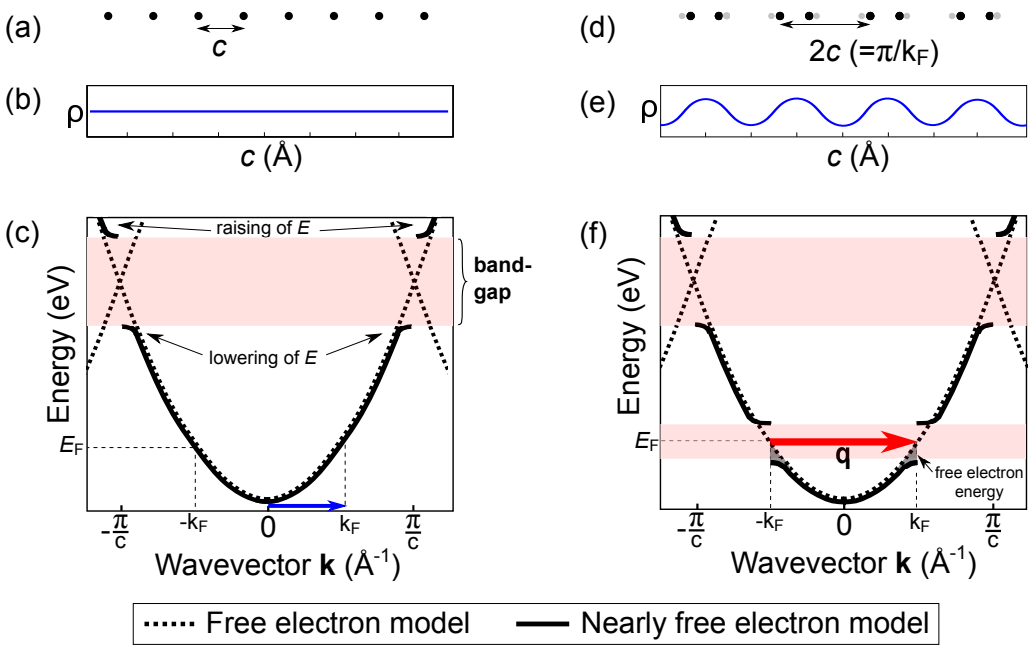

Figure 2.4: (a) A one-dimensional chain of atoms, separated by period c, with (b) a uniform electron distribution ρ along the chain axis c. (c) The energy dispersion curve of the free electron model is a parabola (dotted line), with degeneracies lifted in the nearly free electron model (solid line), leading to the formation of a band-gap (shaded area). (d) The Periodic Lattice Distortion of the one-dimensional chain of atoms, with a superstructure of period $2c$ on top of the main c-periodicity. (e) Charge Density Wave formation in the electron density ρ. The additional periodicity leads to (f) the opening of an additional bandgap at $k = \pm\, \pi/(2c)$, with the lowering of the energy of the electrons below the bandgap indicated with the grey areas. Here, $\vec{q}$ is the nesting vector.

Peierls Transition The dimerisation of $M(DCNQI)_2$, that was illustrated in figure 2.3a and schematically sketched in figure 2.4d, introduces an additional – but much weaker – periodic potential of $U(x) = U(x + 2c)$ (which is the Periodic Lattice Distortion – PLD). Associated with the PLD is a modulation in the electron density, called a Charge Density Wave (CDW), which is illustrated in fig. 2.4e. The two co-exist, are strongly correlated and only occur in materials with strong electron-phonon coupling. A direct consequence of the introduced additional periodicity due to the CDW/PLD formation is the opening of a band gap at the periodicity of the CDW/PLD. The opening of the additional bandgap is shown in figure 2.4f, where the energy states below the gap are lowered.

Let us consider the case where the formed band gap overlaps with the Fermi energy level, E_F. In other words, the introduced superstructure with wave vector $\vec{q}$ (called the 'nesting vector', shown with red arrow in figure 2.4f), fulfils the condition:

$$\vec{q} = 2\vec{k}_F \tag{2.2}$$

In this case, the energy of the highest energy electrons (just below the Fermi level) are lowered, which lowers the total energy of the system. If the resulting electron band

energy gain is larger than the Coulomb and elastic energy it costs to physically move the atoms, the formation of the CDW and PLD is energetically favourable and therefore self-sustaining. This distortion, induced by the lowering of the total energy of a system, was first theorised by Peierls and referred to as a *Peierls transition*[22]. To explain why this transition occurs in certain materials, and not in others, the concept of the Fermi surface is used.

Fermi Surface In the one-dimensional dispersion curve of figure 2.4f, it is easy to imagine that the nesting vector $\vec{q}$ overlaps with the *Fermi surface*, which – in one dimension – is the energy level of E_F in k-space. In multidimensional crystals, Fermi surfaces are also multidimensional. For example, let us imagine the energy dispersion in figure 2.4f, but for two dimensions instead of one, where any interactions along the second dimension are excluded. Now, electrons can only flow along the c-direction ($v_{a,b} = 0$, $v_c \neq 0$), and the two-dimensional energy dispersion will look like the 'stretched' parabola in figure 2.5a. Here, the Fermi surface would be the equi-energy line at $E = E_F$, as indicated with the red line, with nesting vector $\vec{q}$ shown. Shown in figure 2.5b is the 'top-view' of this graph. In this case, any piece of the Fermi surface can be translated by an infinite number of nesting vectors $\vec{q}_n$, such that it overlaps with another piece of the Fermi surface (shown by the blue arrows). When (weak) interactions along the b, c direction are included, the Fermi surface will look something like figure 2.5c. Now, one nesting vector $\vec{q}$ successfully translates all sections of one Fermi surface to the next. In the perfect three-dimensional case ($v_a = v_b = v_c \neq 0$), only one section of the Fermi surface is translated to the next at only one position (figure 2.5d).

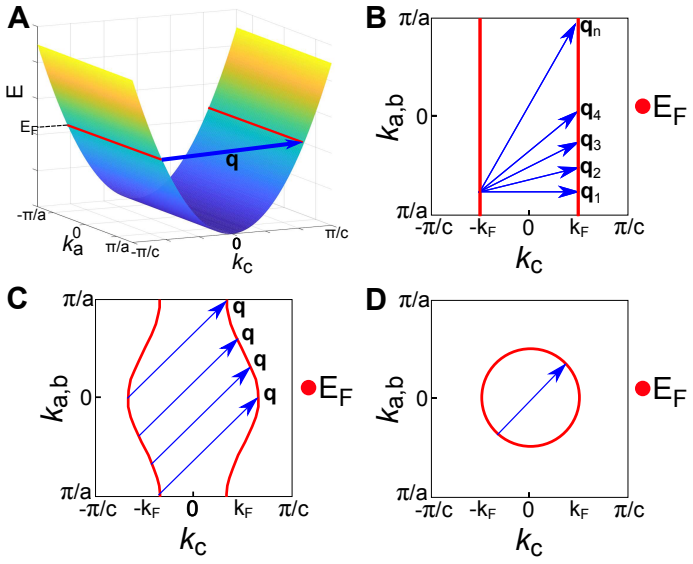

Figure 2.5: (a) A 2D Fermi Surface, with no interactions along a. (b) Fermi surface nesting conditions for the one-dimensional system of (a), with an infinite number of nesting vectors $\vec{q}_n$ succesfully translating the left equi-energy line on top of the right one. (c) Fermi surface nesting conditions with weak interactions along a included. One nesting vector $\vec{q}$ translates all sections of the Fermi surface to the next. (d) Fermi surface nesting conditions for the three dimensional case, with only one nesting vector succesfully translates one section of the Fermi surface to the next. Figure adjusted from ref [1].

These figures illustrate that systems with lower dimensionality (electronic anisotropy) are better 'nested'. Nesting conditions in the case of figure 2.5b and c can favour the formation of a CDW/PLD, whereas the case of figure 2.5 d is poorly nested.

Metallic systems with a nested Fermi surface are electronically unstable. Therefore, the insulating phase opens a bandgap at E_F, which destroys the Fermi Surface.

At high temperatures, electrons can be more easily thermally excited over such a bandgap. Therefore, the lowering of the electrons across the gap is less favourable at high temperatures, which is why CDW phases are observable below a material-specific transition temperature.

Band Filling In the above example, the case of a dimerisation was discussed. The energy at which a bandgap opens, however, depends on the filling of the band (N_{at}). Pauli's exclusion principle states that an energy state can only be occupied by two electrons of opposing spin, so the band is full when each molecule contributes two electrons to the highest band. The band filling, N_{at}, is related to k_F, the Fermi vector, through:

$$N_{at}\frac{\pi}{c} = 2k_F. \tag{2.3}$$

So, if the band is full, a gap opening is expected at $2k_F = 2\pi/c$ (which is the normal crystal periodicity). If the band is half full, a gap opening is expected at $2k_F = \pi/c$ (which is a dimerisation, as discussed above). Evidently, the band filling determines the periodicity of the CDW in CDW materials. If the superstructure is an integer times larger than the crystal structure (e.g. a dimerisation, trimerisation, tetramerisation, etc), the CDW is *commensurate*, whereas for a non-integer it is *incommensurate*.

2.3 Cooperation between Electronic and Structural Properties in Cu(DCNQI)$_2$

2.3.1 Mixed Valency of Cu(DCNQI)$_2$

The occurrence of the CDW/PLD transition in Cu(DCNQI)$_2$ salts depends on their chemical composition. The salts can be divided into three groups. Figure 2.6 shows an example of group I materials (which are metallic down to low temperatures), group II materials (which are metallic at high temperatures, showcasing a Metal-Insulator transition upon cooling) and group III materials (which are metallic at high temperatures, exhibit a Metal-Insulator transition upon cooling, and a Insulator-Metal re-entry upon further cooling).

In the case of monovalent copper ions (Cu^{1+}), the formal charge of the DCNQI anion would be -1/2, which corresponds to a quarter-filled band (which is the case for salts with M $\neq$ Cu, see appendix A.1). The expected CDW/PLD formation for this case would be a tetramerisation. For divalent Cu (Cu^{2+}), the half-filled band would lead to a dimerised CDW/PLD phase. The observation of the trimerisation for Cu(DCNQI)$_2$ compounds, however, is an indication of a one-third band filling, which suggests a mixed valency state of copper: $Cu^{\frac{4}{3}+}(DCNQI^{\frac{2}{3}-})_2$.

The explanation for the existence of the mixed valency state of Cu is the following: the highest 3d orbitals of Cu (which, as an atom, has electron configuration $[Ar]3d^{10}4s^1$, but due to ionisation in the Cu(DCNQI)$_2$ salt, the s-shell is empty) have a similar en-

ergy as the π band of the DCNQIs. The five 3d energy levels – which usually are similar in energy – form two energetically separated groups in a tetrahedral structure[23], as illustrated in figure 2.7a. Here, one group of three 3d orbitals (d_{xy}, d_{yz} and d_{xz}, called T_{2g}) lies higher in energy, whereas the remaining group of two 3d orbitals (d_{xz} and d_{yz}, called E_g) lie lower in energy. In the case of the symmetry for a *distorted* tetrahedron, the set of T_{2g} levels splits (figure 2.7b), whereby d_{xy} is raised in energy, while the degenerate d_{xz} and d_{yz} orbitals are lowered in energy. The amount of splitting (ΔE) in this case depends on the amount of distortion of the tetrahedron.

Calculations by Kobayashi et. al.[18] revealed that for low splitting (corresponding to an undistorted tetrahedron), the interaction of the p_π orbital with all three Cu d_{xy}, d_{xz}, d_{yz} orbitals leads to a "multi Fermi surface" character, which has poor nesting conditions. As previously discussed, this makes the CDW/PLD phase unstable. However, in the case of sufficient splitting of the copper energy levels (for a highly distorted tetrahedron), only the Cu d_{xy} orbital interacts with the p_π band of the DCNQI, leading to a much simpler Fermi surface. Here, nesting is achieved by $q = c^*/3$, thereby stabilising the $2k_F = 2\pi/(3c)$ (trimerised) CDW/PLD formation.

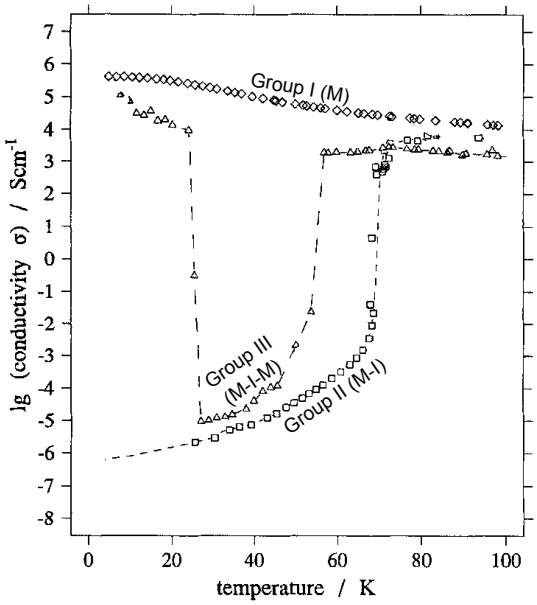

Figure 2.6: Temperature dependent conductivity of Cu(DMe-DCNQI)$_2$ (group I), Cu(DMe$_3$-DCNQI)$_2$ where all hydrogens in the material are deuterated (group II) and Cu(h$_8$/d$_6$-DCNQI)$_2$, where 50% of the DCNQI's restgroup is DMe (CH_3), and the other 50% CD_3 (where D is deuterium, group III). Figure adjusted from ref [24].

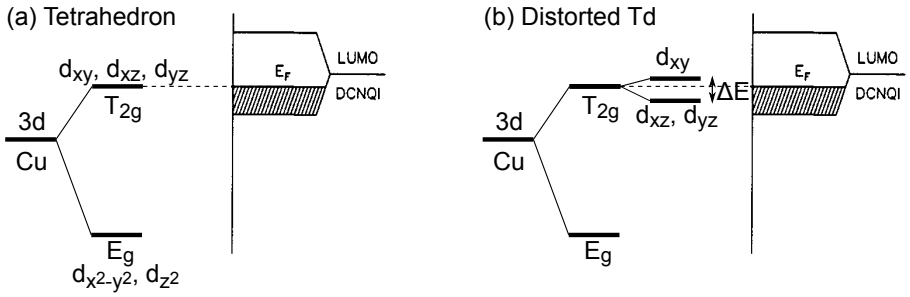

Figure 2.7: Schematic energy diagrams of the orbital overlap of Cu with the DCNQI LUMO (Fermi level indicated) for an (a) undistorted tetrahedron and a (b) distorted tetrahedron. In the latter case, the tetragonal distortion splits the T_{2g} state. Figure adjusted from refs [25] and [18].

N–C–N Angle (α), Overlap of p_π-Band and d_{xy}-Orbital, Charge Transfer from Cu to DCNQI, and Stability of the CDW Phase The distortion of α in the tetrahedron is highly variable, with numerous studies (on different compounds or compounds under pressure) revealing the interplay between structural changes and the material's electronic properties.

Before presenting the results of these respective studies, their main conclusions (taken from [26]) are stated below:

1. *When $Cu(DCNQI)_2$ is in the metallic state, the average valence of Cu is slightly below +4/3 (which destabilises a [commensurate] trimerisation). For the transition to the insulating phase to occur, the average valence of Cu needs to increase to +4/3 (Cu^{+}:Cu^{2+} = 2:1).*
2. *By applying pressure to $Cu(DCNQI)_2$, or equivalently, by (1) having smaller R_1,R_2 substituents on the DCNQI molecules or (2) by reducing temperature, the distortion of the tetrahedron is enhanced (i.e. α is increased).*
3. *The enhancement of the tetrahedron distortion raises the highest-lying d_{xy} orbital. The raising of this orbital induces extra charge transfer from Cu to DCNQI (this is schematically shown in figure 2.8).*
4. *Once the extra charge transfer is large enough such that the average valence state of copper is +4/3 (at a critical angle of α = 126 – 127°), a first-order M-I transition is provoked. Now, a CDW is formed in the presence of a strong correlation, with a static charge ordering $\cdots Cu^{+}Cu^{2+}Cu^{+}\cdots$.*

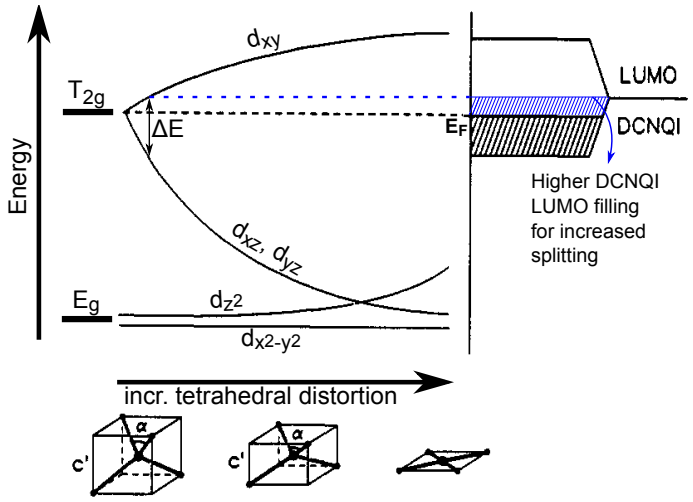

Figure 2.8: Illustration of how the splitting of energies ΔE evolves for increasing tetrahedral distortion. The lifting of the d_{xy} orbital of the copper for larger distortions, enhances charge transfer to the DCNQI LUMO. Figure adjusted from ref [25].

In the next sections, the results of previous studies will be presented (not necessarily in chronological order) to support these statements.

2.4 Previous Studies on $Cu(DCNQI)_2$

X-ray Photoemission Spectroscopy X-ray photoelectron specroscopy (XPS) studies on $Cu(DCNQI)_2$ have shed light on the mixed valency property of $Cu(DCNQI)_2$. In XPS, the energy of photo-electrically emitted core-electrons (by incoming X-ray photons) are measured in order to determine the binding energies of the electrons. In the case of XPS on Cu, the binding energy of the 2p core level can for example be detected. Depending on the chemical environment of Cu (e.g. whether its valence is +1 or +2), small shifts in the photoelectron spectrum are observable. The first XPS results on the 2p core level of Cu in $Cu(DCNQI)_2$ initially lead to a controvosy, when Schmeisser et. al.[27] only observed binding energies of Cu 2p electrons in XPS spectra that are related to Cu^{1+}, while shifts of XPS signals related to mixed valency were absent. Furthermore, the XPS spectra that they obtained for R_1,R_2 = BrMe; ClMe; and DMe were identical, suggesting that there is no variation in the mixed valency state depending on chemical composition. Thereby, monovalency for all compounds was claimed, in contradiction with the observation of $c^*/3$ peaks in X-ray diffraction measurements, which suggests a mixed valence of $\sim$ 1:2.

The fact that XPS is highly surface sensitive should, however, be taken into account, as results (like those of Schmeisser et. al.) are highly affected by surface contaminations. Therefore, in an XPS follow-up study done by Ioune et. al.[28], surface layers were gently scraped in an ultra high vacuum with a diamond file, enabling the investigation of a clean and fresh surface layer during XPS experiments. The XPS spectra obtained from these surfaces could be decomposed into three contributions that are spectrally shifted w.r.t. each other (as shown in figure 2.9): a contribution from Cu^{1+}, and 2 contributions from Cu^{2+} (main and satellite peaks). Here, the Cu^{1+}:Cu^{2+} contribution ratio is approximately 2:0.9$\pm$0.1, demonstrating a mixed-fluctuating valence state of Cu in the metallic phase, with an average valence slightly below +4/3.

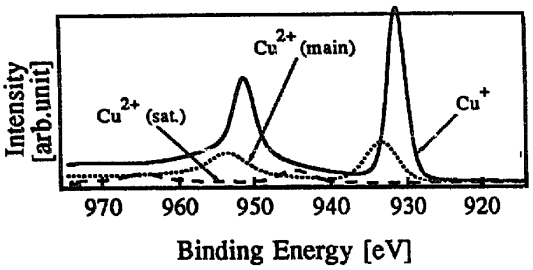

Figure 2.9: The three contributions from Cu^{1+}, Cu^{2+} (main) and Cu^{2+} (sattelites) in an XPS spectrum of Cu 2p in $Cu(DMe\text{-}DCNQI)_2$. Taken from [28].

Table 2.1: Transition temperature, average valence of Cu ions, and the N–Cu–N angle for four different compounds (from ref [29]).

Compound	T_{MI} (K)	Average Valence	α (°)
$Cu(MeCl\text{-}DCNQI)_2$	210	+1.31	126.2
$Cu(MeBr\text{-}DCNQI)_2$	160	+1.32	125.3
$Cu(DMe\text{-}DCNQI)_2$	–	+1.28	124.5
$Cu(DI\text{-}DCNQI)_2$	–	+1.22	122.3

In a later study, room temperature XPS spectra on a variety of compounds were obtained by Akaki et. al.[29]. The valence of these compounds is shown in table 2.1. The R_1,R_2 = DMe and DI compounds – which are group I salts (no insulating phase)

– have the lowest valence. As evident from table 2.1, the relationship between the average room temperature valence of copper and the metal-to-insulator phase transition temperature (T_{MI}) indicates that a deviation away from +4/3 destabilises the insulating phase. It should also be noted that, indeed, an increase in the N–Cu–N α angle in the structure of the material (third column of the table, data from X-ray crystallography) – which lifts the d_{xy} orbital of Cu – leads to a larger charge transfer from Cu to the DCNQI p_π band. Furthermore, XPS spectra taken for the MeCl compound in the conductive and insulating phase (300 K and 170 K, transition at 210 K) showed a shift in valence from +1.31 to +1.33. On the other hand, the MeBr compound shows a temperature-independent valence of +1.32 in the conductive phase from 300 K and 170 K (transition at 160 K). These findings support that a tetrahedral distortion is required to push the Cu valence up to +4/3, such that a transition into the insulating phase can occur.

Varying R_1,R_2 Substituents As previously mentioned, Cu(R_1,R_2-DCNQI)$_2$ compounds with varying R_1,R_2 substituents can be divided into three characteristic conductivity behaviour groups. In general, R_1,R_2 of group I – which is the family of compounds with no insulating phase – are the more bulkier substituents. For group II materials, the substituents are less bulky, with smaller substituents having a higher metal-to-insulator temperature (T_{MI}). This is shown in table 2.2, where Cl<Br<Me. Again, the N–Cu–N angle (α) is indicated in the third column of the table. All group I materials (not shown in the table) have an α angle below 124.7°.

Table 2.2: The phase transition temperature and α at 300 K for group II compounds. Data from [26].

Compound	T_{MI} (K)	α at 300 K (°)
Cu(MeBr-DCNQI)$_2$	155	125.3
Cu(DBr-DCNQI)$_2$	160	125.3
Cu(MeCl-DCNQI)$_2$	210	126.2
Cu(BrCl-DCNQI)$_2$	213	126.1
Cu(DCl-DCNQI)$_2$	230	127.1

The nearly linear relationship between T_{MI} and α (where the α increase causes the lifting of the highest Cu 3d orbital and therefore an increase in Cu valency) at 300 K is shown in figure 2.10 (same data as table 2.2). This suggests a strong relation between the tetrahedral distortion – due to substituent bulkiness – and the thermal stability of the insulating phase.

The α increase for smaller R_1,R_2 substituents (observed with X-ray experiments), corresponding with larger charge transfer from the Cu d_{xy} to the DCNQI LUMO (observed with XPS data), are consistent with each other. It would also be interesting to track the α dependence on the temperature. This was

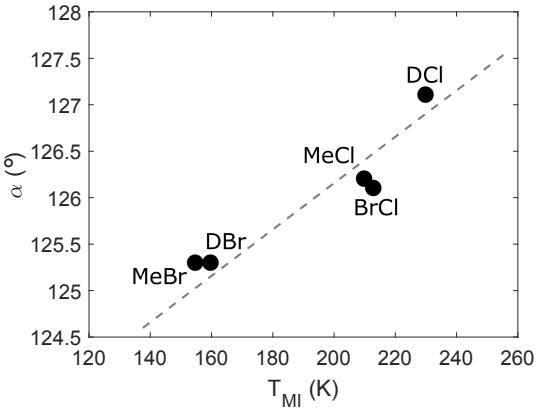

Figure 2.10: The correlation the N–Cu–N angle α and the phase transition temperature T_{MI}.

done by means of X-ray experiments on Cu(Me,Br-DCNQI)$_2$, of which the results are shown in figure 2.11a. A clearly discontinuous α increase is observed at T_{MI} (which corresponds to the average Cu valence getting closer to +4/3). This agrees well with the contraction of the crystal c axis of Cu(Me,Br-DCNQI)$_2$ upon cooling, which shows a discontinuous step at the same temperature (figure 2.11b, other compounds are also shown). In these X-ray experiments, the $c^*/3$ peaks – indicative of the trimerised PLD/CDW phase, as previously shown in an electron diffraction pattern in figure 2.3c – appear at a temperature right below the step[1] (figure 2.11c). The discontinuous appearance of the trimerised phase, whose intensity does not increase upon further cooling, emphasises the first-order character of the transition. Furthermore, the simultaneous $c^*/3$ appearance and α increase emphasises the cooperativity between the electronic and structural properties.

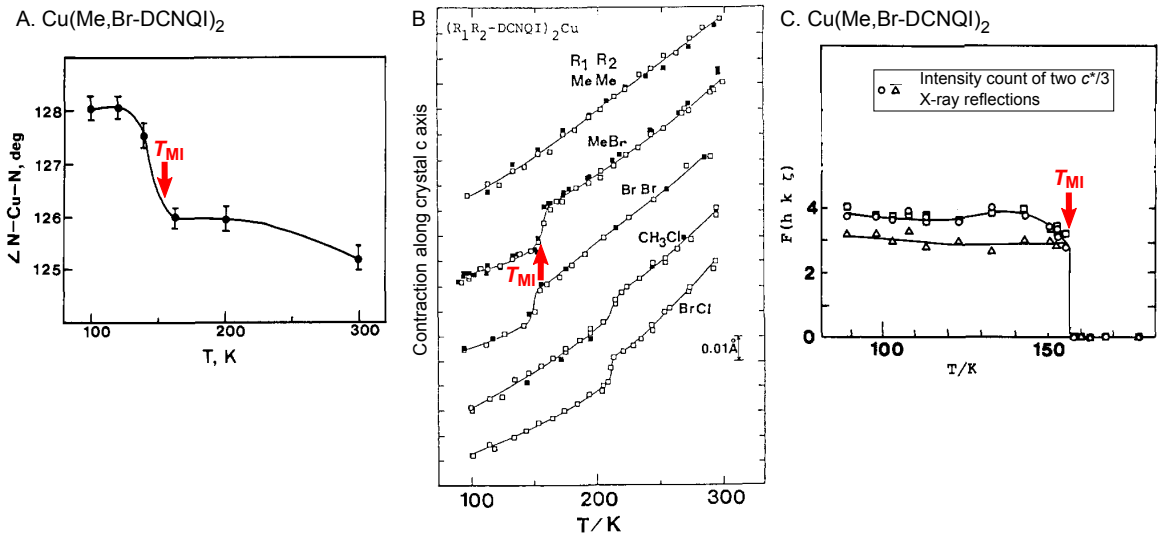

Figure 2.11: The discontinuous increase of α in Cu(Me,Br-DCNQI)$_2$ at T_{MI} (a) corresponds well with the discontinuous contraction along the crystal c-axis right above T_{MI} (b, other compounds also shown), as well as the discontinuous appearance of $c^*/3$ reflections at T_{MI} (c). Taken from [23] and [30].

Applying External Pressure When Tomic et. al. performed temperature dependent resistivity measurements on Cu(DM-DCNQI)$_2$ crystals (group I) under pressure, they observed that increased pressure conditions can provoke the metal-to-insulator transition (effectively turning the material into a group II or group III member)[31]. By only applying a pressure of as little as 110 bar, a metal-to-insulator phase transition upon cooling is observed at $T_{MI} = 55$ K (figure 2.12a), which is lifted to higher temperatures for higher pressures. This suggests that Cu(DM-DCNQI)$_2$ is a 'border-line' group I/II/III member, making it a suitable 'toy-model' for minor alterations by, for example, deuteration (see next paragraph). A sufficiently sampled p,T phase diagram (for increasing and decreasing pressure) is shown in figure 2.12b. Interestingly, in the pressure regime from ∼100 – 300 bar, the second insulator-to-metal transition is also inducible, which is a group III characteristic.

[1] In section 4.1, it will be shown that this is consistent with our own electron diffraction cool-down data on Cu(Me,Br-DCNQI)$_2$.

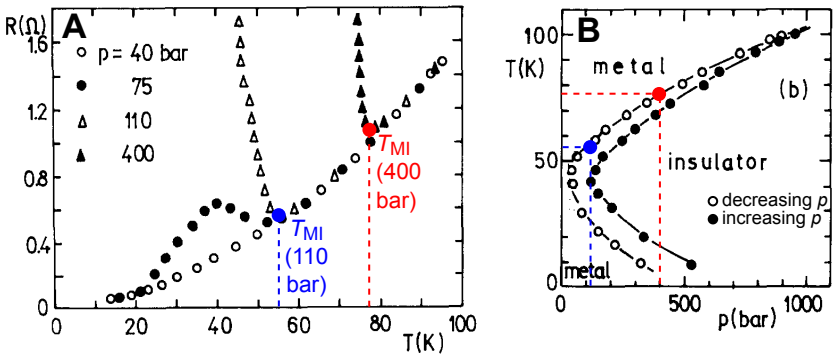

Figure 2.12: (a) Temperature-dependent resistance upon cooling for selected pressures applied to Cu(DM-DCNQI)$_2$. (a) The p,T phase diagram obtained for varying p. Corresponding data points between (a) and (b) are indicated. Figure adjusted from [31].

An investigation of the temperature dependent Cu(Me,Br-DCNQI)$_2$ (T_{MI} = 155 K at 1 bar), resistivity under pressure showed a similar trend (figure 2.13a), whereby T_{MI} increases for increasing pressure. Furthermore, the first-order character of the transition is suppressed for increasing pressure. Because of the similarity in the temperature dependent resistivity for – firstly – smaller R_1,R_2 substituents and – secondly – increasing "external" pressure, the substituent effect is often referred to as "internal pressure" or "chemical pressure". A study of the Cu(DM-DCNQI)$_2$ structure for increasing pressure (i.e. the effect of pressure on α) has been performed[32], where – as expected – an increased tetrahedral distortion for increasing pressure is observed (figure 2.13b). This trend – due to external pressure – corresponds well with that of chemical pressure.

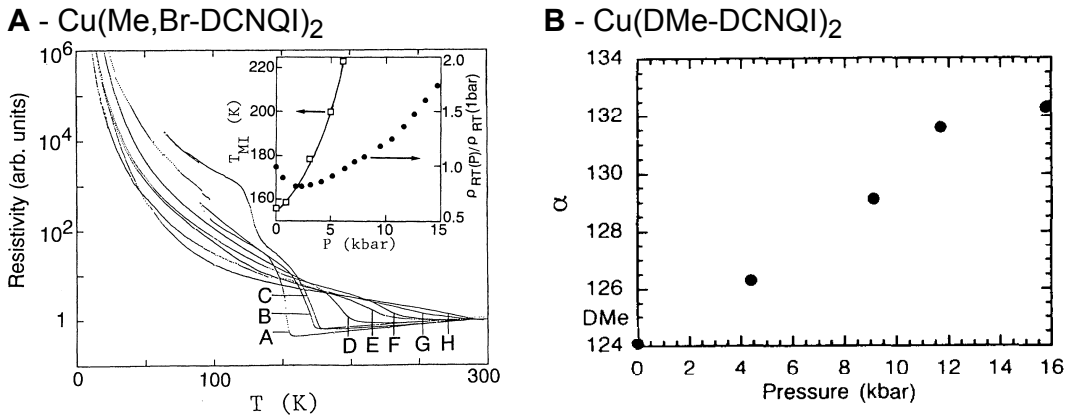

Figure 2.13: (A) Temperature dependent resistivity of Cu(Me,Br-DCNQI)$_2$ for p = 1 kbar (A); 3 kbar (B); 3 kbar (C, heating); 4 kbar (D); 6 kbar (E); 6 kbar (F, heating); 10 kbar (G); 15 kbar (H). Inset shows p dependence of T_{MI} and the p change of resistivity at 300 K. Taken from [33]. (B) Evolution of α for increased pressure for Cu(DMe-DCNQI)$_2$. Taken from [32].

Deuteration of Hydrogens in Cu(DM-DCNQI)$_2$ A remarkable advancement in the predictability of Cu(DCNQI)$_2$ conductivity properties came about when Hünig et. al. first observed that the DMe compound (group I) undergoes a phase transition upon deuteration of hydrogens[34]. Furthermore, compounds with at least two deuterated hydrogens on the two CH_3 substituents exhibit a giant insulator-to-metal re-entry at lower temperatures[35] (a group III characteristic), previously only observed under

increased pressure conditions. The exact temperatures of (both) transition(s) depends very sensitively on the amount of deuteration[25], making the engineering of desired properties (as motivated in chapter 1) possible. The temperature dependent conductivity behaviour of several (of many synthesised) deuterated DMe compounds – chemical formula Cu(d_n[a_1;a_2;a_3]-DCNQI)$_2$ – are shown in figure 2.14b. Here, the pattern of deuteration is denoted by d_n[a_1;a_2;b] (figure 2.14a), where a_1 and a_2 stands for number of deuterons on 2-Me and 5-Me respectively (between 0 – 3), where b stand for for the number of deuterons on the benzene ring (between 0 – 2). n in d_n is the total number of deuterons: a_1 + a_2 + b (between 0 – 8).

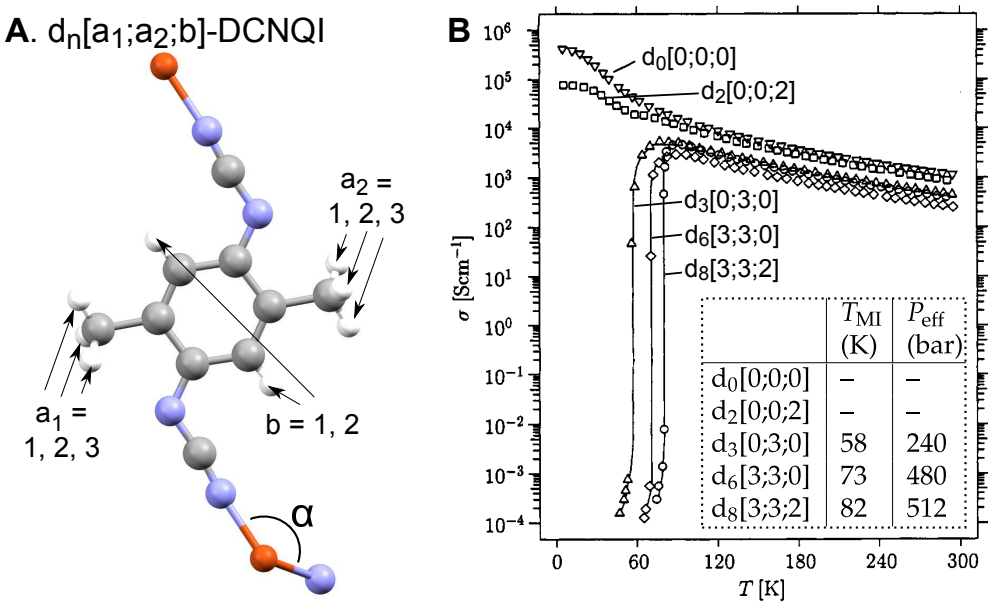

Figure 2.14: (a) Name-giving of deuterated Cu(DMe-DCNQI)$_2$, with a_1 and a_2 the number of deuterons on the R_1 and R_2 methyl group respectively, and b the number of deuterons on the benzene ring. (b) Temperature dependent conductivity for selected Cu(d_n[a_1;a_2;b]-DCNQI)$_2$s, indicative of a higher T_{MI} and larger P_{eff} (calculated with equation 2.4) for increasing deuteration. Graph from [25], data in inset (b) from [35].

The ability to carefully tune T_{MI} (as was previously done with pressure), and the existence of a re-entry transition (previously only observed under high pressure conditions), suggests that the amount of deuteration can be expressed as effective pressure. The linear relationship found was[26]:

$$P_{eff} \approx 80 \cdot \{(a_1 + a_2) + 0.2b\} \text{ bar} \tag{2.4}$$

The effective pressures shown in the table of figure 2.14b are calculated from this simple equation. The increase of P_{eff} (and therefore T_{MI}) for increased deuteration is due to the reduction of substituent volume (as the C-D bond length is ∼0.005 Å shorter than the C-H bond), making the substituent less bulky. This reduced bulkiness is reinforced by the reduction of the c-crystal constant upon larger deuteration, observed in X-ray crystallography measurements[36]. Unfortunately, these X-ray crystallography measurements were not of sufficient quality to obtain the extraction of possible significant changes in tetrahedral distortion parameter α for varying deuteration. However, as was previously shown in figure 2.11a and b, the contraction of c for an increasing number of deuterons is indicative of an increase in α.

The sensitivity of perturbation in the coordination around Cu was also observed when the carbons closest to the coppers (–***C***≡N) were substituted with ^{13}C-isotopes, and the nitrogens closest to the coppers with ^{15}N-isotopes[37]. Both provoke the M-I and I-M transition upon cooling in Cu(d_0-DMe-DCNQI)$_2$ and Cu(d_1-DMe-DCNQI)$_2$ (which have zero and one deuterons on each methyl group, respectively), turning them from a group I into a group III material. Furthermore, both ^{13}C and ^{15}N substitutions increased the transition temperature T_{MI} of Cu(d_2-DMe-DCNQI)$_2$, and turns them from a group II into a group III salt, while increasing T_{MI}. In all cases, a contraction of the crystal *c*-axis was observed for the ^{13}C and ^{15}N compounds (corresponding to an increased chemical pressure) in comparison with the 'normal' ^{12}C and ^{14}N counterparts.

Alloys of Chemical Compositions A large variety of 37 alloys of copper salts have been prepared, where a salt consists of a mixture of two different types of R_1,R_2-DCNQI molecules[38]. This is denoted as Cu[(R_1,R_2-DCNQI)$_{1-x}$(R_3,R_4-DCNQI)$_x$]$_2$, $0 \leq x \leq 1$. Alloys from compounds with and without phase transitions are of particular interest, e.g. that of DMe (group I) and MeBr (group II)[39]. Here, increasing the fraction of MeBr in Cu(DMe/MeBr-DCNQI)$_2$ has a similar effect as that of increasing pressure[33].

As DMe compounds are easy to grow, large mono-crystalline needles are easily obtained. Furthermore, their conductivity properties for deuterated d_n-DCNQI compounds are incredibly predictable and desired material characteristics can be easily tailor-made. Therefore, alloys of Cu(d_n-DMe-DCNQI)$_2$ are a suitable material for extensive study. Temperature dependent conductivity and magnetic susceptibility measurements were done on h_8/d_8-DCNQI alloys (a mixture of none [h_8] and all [d_8] hydrogens in DMe-DCNQI deuterated)[41]. Futhermore, electronic spin resonance (ESR) measurements on different percentage mixtures on d_6/h_8 compounds were done, as will be discussed later[42]. Lastly, the first compounds that were photo-switched from the insulating to the metallic phase by Karutz et. al. in 1998 were done on d_6/h_8 alloys[43], which will be discussed in chapter 4.

Besides alloys of the DCNQI-molecule, Cu(DCNQI)$_2$ can also be doped with different metallic cations. Lithium-doped Cu(DCNQI)$_2$ has been extensively studied, as the similarity in effective radii of monovalent Cu^+ (55 pm) and Li^+ (62 pm) – with Li(DCNQI)$_2$ and Cu(DCNQI)$_2$ being isostructural – are indicative of minor structural disturbance[38]. As is explained in appendix A.1, there is no orbital mixing between Li and DCNQI. The +1 valency of the doped lithium cations therefore leads to a lowering of the average valence of the cations.

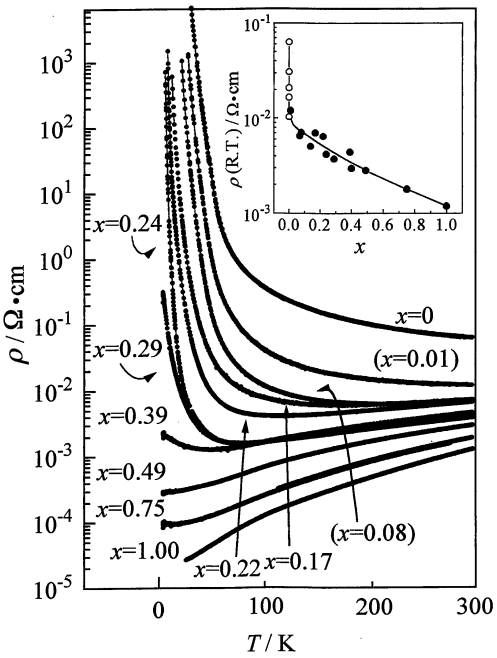

Figure 2.15: Temperature dependent resistivity for $Cu_{1-x}Li_x$(Me,Br-DCNQI)$_2$, $0 \leq x \leq 1$. Increased doping (corresponding to a decreased charge transfer from the cation to DCNQI) destablises the insulating phase. Inset: resistivity x dependence (open circles for $x = 0$). Taken from [40].

As was previously concluded from XPS results, the lowering of cation valence is expected to destabilise the insulating phase. A study on $Cu_{1-x}Li_x(Me,Br\text{-}DCNQI)_2$ ($0.25 < x < 0.5$) confirmed the suppression of the insulating phase for increased lithium doping [39]. Later measurements of the temperature dependent conductivity obtained for a wider range of x values are shown in figure 2.15[40]. Doping with divalent Zn^{2+}, on the other hand, has the effect of positive pressure. By increasing the average cation valence to values closer to +4/3 due to a larger fraction of Zn^{2+}, T_{MI} can be raised[44].

In conclusion, control over the phase transition properties in $Cu(DCNQI)_2$ is achieved by the synthesis of DCNQI alloys and cation doping. Hereby, predictable and systematic changes in conductivity behaviour are accessible.

Photoemission Spectroscopy near E_F Photoemission spectroscopy performed in the Fermi energy level range (UV range) demonstrated that the signal in the vicinity of the Fermi level decreases upon cooling above T_{MI}, called a 'pseudo-gap' formation[45]. The gap opening continues across T_{MI}, causing the metal-to-insulator transition. Shown in figure 2.16 are photoelectron spectra taken at 30 K and 300 K (a compound with T_{MI} = 60 K was used), showing the signal decrease at E_F for $T = 30$ K. Furthermore, the spectral feature at higher binding energies becomes narrower at lower temperatures, with photoemission signal shifting from a narrow energy range around E_F to a broad energy range at higher binding energies. As was mentioned, due to the valency mixing, interactions perpendicular to the π channels are possible, with the copper acting as bridges. Both the redistribution of photoemission signal over a broad energy range and the pseudo-gap formation at high temperature are attributed the reduction of inter-π channel interactions due to strong electron-electron interactions, thereby enhancing the one-dimensional properties (and therefore Fermi surface nesting conditions) when approaching T_{MI} upon cooling.

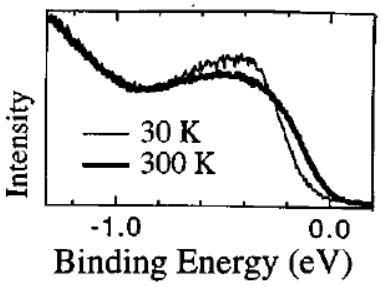

Figure 2.16: 30 K ($< T_{MI}$) and 300 K photoemission spectra near E_F. The leading edge is shifted with $\sim$ 100 meV, with spectral weight transferred to higher energies. Taken from ref [45].

Infrared Spectroscopy In a study by Yamakita et. al.[46], infrared spectra at room temperature were obtained from the following powdered samples in a KBr disk: (1) neutral DBr-DCNQI and DMe-DCNQI molecules, (2) monovalent Li salts of DCNQI (charge transfer $\rho = -0.5e$), (3) divalent Ba salts of DCNQI ($\rho = -1.0e$), and (4) mixed valency Cu salts of DCNQI (ρ = unknown). In these spectra, the bands of the C=N and C=C stretching modes (among many other modes) are identified. The DCNQI LUMO has an anti-bonding character with these two bonds, meaning that a higher filling of the LUMO will weaken them. Therefore, a shift of these two stretching modes to lower frequencies is observed for the above-mentioned increased charge transfer. The known charge transfer from the neutral molecules and Li,Ba salts enabled the correlation of the frequencies at which the absorption bands are observed ($\tilde{\nu}_i$) with the degree of charge transfer from the Cu d_{xy} orbital to the DCNQI LUMO (ρ). By using one-dimensional regression analyses, a linear $\tilde{\nu}_i, \rho$ relationship was obtained. Hereby, a charge transfer

of $\rho = -0.67e$ was obtained for the copper salt, as was previously concluded from X-ray diffraction and XPS.

Subsequently, temperature dependent infrared spectra of Cu(DBr-DCNQI)$_2$ (T_{MI} = 160 K) were taken upon cooling, with two clear changes emerging at $T < T_{MI}$. Firstly, the absorption bands split into three. This is due to the "freezing" of the CDW, associated with the static charge ordering of the coppers: $Cu^{+}Cu^{2+}Cu^{+}$. Secondly, new "electron-molecular vibration" (EMV) bands (linked to electron-molecular vibration coupling, observable in Raman spectra of neutral MeBr-DCNQI) appear in IR spectra at $T < T_{MI}$. This is indicative of a structural change at T_{MI}, whereby DCNQI molecules deviate from inversion symmetry points in the crystal at $T < T_{MI}$.

The appearance of EMV bands, as well as the splitting of normal bands into three, occurs gradually in these experiments. As the transition is known to have a first-order character, Yamakita et. al. argued that the fluctuating Cu^{2+}:Cu^{+} (1:2) states discontinuously locks into the static ordered state at $T = T_{MI}$, while the CDW follows gradually and increases in magnitude upon cooling. However, a follow-up study by Tajima et. al. on stress-free single crystal needles observed the discontinuous appearance of EMV bands and the splitting of 'normal' bands into three at $T = T_{MI}$, with little changes occurring upon further cooling below T_{MI}[47]. This revealed the true first-order character of both the structural changes as well as the CDW formation at $T = T_{MI}$. The 'smeared out' changes observed by Yamakita et. al. are explained by the local-stress effect in the powder in the KBr disk, leading to a co-existence of both phases around T_{MI}.

ESR Electron spin resonance (ESR) is a method used to characterise electronic structures of materials with unpaired spins. In ESR measurements, an external magnetic field is applied to the sample under investigation, which splits the electronic spin states of unpaired electrons into two. On top of that, electromagnetic microwaves (in the GHz regime) are applied, and the frequency is swept. When the frequency of the microwaves matches the energy splitting of the spin states, energy of the microwave signal is absorbed and an absorption peak can be observed. Here, the g-factor – which refers to the amount of splitting – highly depends on the interactions of the electron with its surroundings, allowing the identification of electron species. For example, for ESR measurements on Cu(DCNQI)$_2$ compounds, the g-factors are as high as 2.4, which indicates that the ESR signal originates from Cu^{2+}[30] (which has an unpaired electron in the highest 3d level, and is therefore ESR active). The observed ESR intensities are consistent with the Cu^{+}:Cu^{2+} ratio = 2:1.

The linewidth of an ESR signal is influenced by interactions between neighbouring atoms, with narrow linewidths being indicative of isolated spin states. In the case of Cu(DCNQI)$_2$, the material has magnetic susceptibility in the metallic phase ($\chi \approx 5 \cdot 10^{-4}$ emu/mole, shown in figure 2.17a for the case of Cu(d$_8$-DCNQI)$_2$). However, the three-dimensional movement of electrons in the hot temperature phase – combined with spin-orbit coupling and exchange between π conduction electrons and Cu 3d electrons – leads to extreme linewidth broadening of ESR signals. Therefore, no ESR signal is observed in the metallic phase at $T > T_{MI}$ (figure 2.17b). As previously mentioned, in the low temperature phase ($T < T_{MI}$), coppers occupy a static charge ordering of $\cdot Cu^{+}Cu^{2+}Cu^{+}\cdot$. In that case, Cu 3d electrons with unpaired spins are localised, leading to narrowing of the linewidth at $T < T_{MI}$ for decreasing temperature[48] (fig-

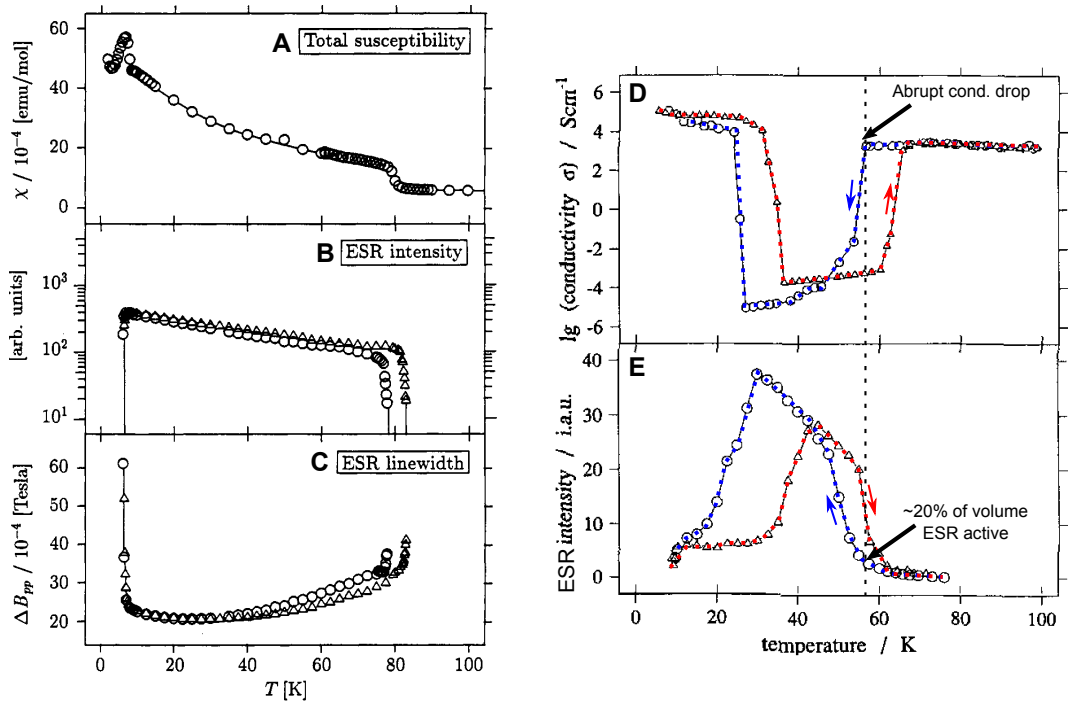

Figure 2.17: (a) The magnetic susceptibility, (b) ESR intenstiy and (c) ESR linewidth for Cu(d_8-DCNQI)$_2$. (d) The temperature dependent conductivity and (e) ESR intensity for cooling (blue) and heating (red) for Cu(70%:30%-h_8/d_6-DCNQI)$_2$. Taken from [25] and [24] respectively.

ure 2.17c). Therefore, the material becomes ESR active at $T < T_{MI}$[49][2]. Furthermore, a discontinuous jump in χ is observed at T_{MI} (fig 2.17a). The sudden magnetic susceptibility increase suggests the simultaneous disappearance of π conduction electrons and the appearance of local magnetic moments on the Cu sites[50]. In other words, the picture of the fluctuating Cu^{2+} and Cu^{+} states at high temperatures transitioning to static localised states (corresponding to lower dimensionality) upon cooling, are supported by ESR through the observation of confined electrons at $T < T_{MI}$[51]. So, besides the dramatic conductivity changes at $T = T_{MI}$ for group II and group III compounds, these metal-to-insulator transitions are also characterised by an abrupt change in magnetic properties.

As ESR is sensitive to isolated Cu^{2+} throughout an entire sample volume, the ESR intensity is an excellent indicator to determine which fraction of the sample has undergone the phase transition. Shown in figure 2.17d and e are the temperature dependent conductivity and ESR intensity. In the transitional temperature region, corresponding to a steep discontinuous conductivity change, the change in ESR intensity is a rather smooth one. This indicates that upon cooling, the static charge ordering starts in small domains, despite the strong first-order character of the conductivity. The insulating domains start growing upon cooling[42] (here, the insulating and conducting domains co-exist), and eventually close up. The conductivity breaks down when about 20% of the volume is switched to the insulating phase (indicated with dashed line in figure 2.17c and d). Below this critical volume, conducting domains of the material are still "interconnected", but they are interrupted below. Therefore, a full conductivity drop is achieved within an extremely narrow temperature range.

[2]The broadening and eventual vanishing of ESR signal at lower temperatures as noticable at 8 K in figure 2.17b and c is caused by antiferromagnetic ordering.

2.4.1 Conclusion

The results of all the above studies on pressure- and temperature- dependent conductivities on a large variety of $Cu(DCNQI)_2$ salts are summarised in the rough generalised phase diagram shown in figure 2.18. Compounds with bulky R_1,R_2 substituents are group I materials (e.g. R_1,R_2 = DI, DMe, indicated in the diagram with red dotted lines), which are metallic down to low temperatures. By increasing pressure, deuteration of hydrogens, or by substituting with ^{13}C or ^{15}N, group III or group II properties (with first-order M-I and I-M transitions, and only the M-I transition, respectively) are provoked. All these mentioned external influences increase the N–Cu–N α angle, causing a larger charge transfer to DCNQI. An increase in Zn^{2+} doping or a decrease in Li^{+} doping has the same effect on the charge transfer. This increased charge transfer stabilises the entry into the insulating phase, which occurs at a formal charge of $-2/3e$ on the DCNQIs.

The above influences are effectively the same as what a decrease of bulkiness of the R_1,R_2 substituents would bring about. This is shown with the red dotted lines in figure 2.18 for h_8/d_6-DMe (non-deuterated/deuterated alloy) > Me,Br > Cl,Cl.

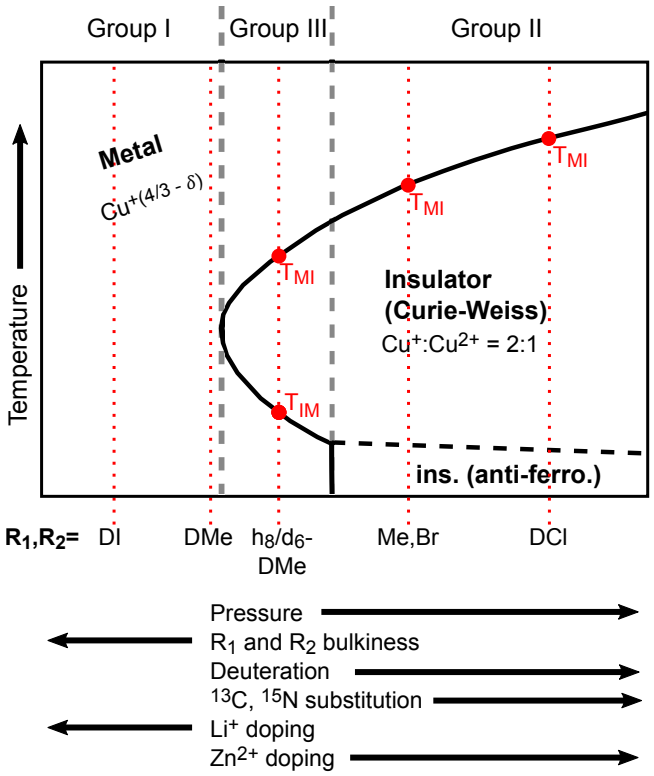

Figure 2.18: Schematic pressure-temperature diagram, displaying the effect of "effective pressure" by external influences. Figure adjusted from [26].

2.5 Switching by Light

When the metal-to-insulator phase transition is induced by pressure or temperature, strong hysteresis is typically observed. Conductivity measurement in this hysteresis temperature window (which, depending on from which 'direction' you come – whether you come from increasing or from decreasing temperature/pressure – can exhibit both the metallic and insulating phase) were performed under increasing and decreasing pressure and light intensity conditions[52]. Samples under constant light illumination experience transition temperatures at lower temperatures, as light can be considered as additional heating. The ability to fine-tune light intensity to which samples are exposed with high accuracy, allows the investigation of this narrow temperature hysteresis loop. Shown in figure 2.19 is a hysteresis loop of Cu(d_6-DCNQI)$_2$ at $T = 61$ K ($T_{MI} = 60$ K). Here, pressure is firstly increased (right hand side of graph, start point A), upon which the crystal is switched to its insulating phase. Secondly, upon decreasing pressure, the material remains insulating. Thirdly, the crystal is re-set to its conductive phase by increasing light intensity (left hand side of graph in figure 2.19, start point B). Although the intensity increase is highly controllable, no stable state between the insulating and conducting phase is accessible. Finally, upon decreasing the light intensity, the material remains conducting.

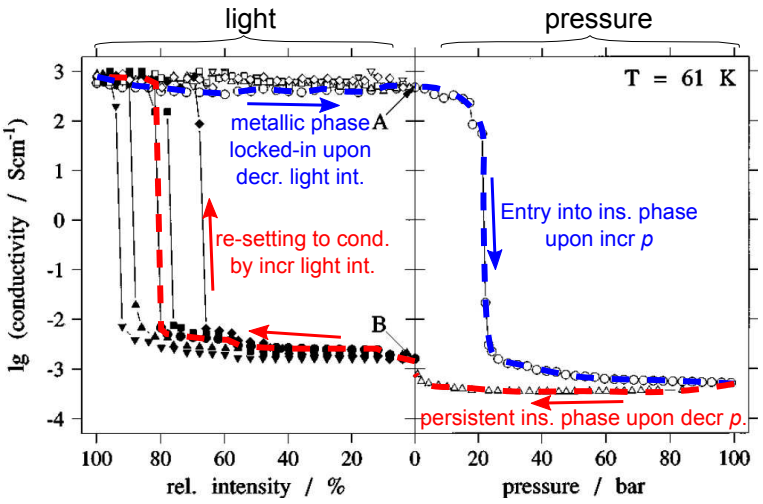

Figure 2.19: (right) Starting at A, Cu(d_6-DCNQI)$_2$ is switched to an insulator by increasing pressure. Upon lowering pressure, the insulating phase is persistent. (left) The sample was then switched back to the conducting phase by increasing light intensity (shown for multiple wavelengths), where switching with higher frequencies is 'easier' due to increasing optical penetration depth. Figure adjusted from [52].

As the penetration depth of light into Cu(DCNQI)$_2$ for shorter wavelengths is larger, the transition in the bulk needles is more easily provoked at shorter wavelength. The observation of the switching of a bulk needle in figure 2.19 to the fully conductive phase (needle thickness ∼100 µm) by photoexciting only the first 100 nm, is indicative of a domino-effect upon photo-switching[53].

Von Schütz et. al. further explored the hysteresis temperature window (where the conducting and insulating phase co-exist) by tracking time-dependent conductivity and ESR signals upon exposing Cu(d_6-DCNQI)$_2$ crystals at $T = 61.3$ K to pressure and light pulses[54]. A pressure pulse provokes the persistently stable insulating phase at $t = 50$ s (figure 2.20a), which corresponds to an increase in ESR signal (figure 2.20b),

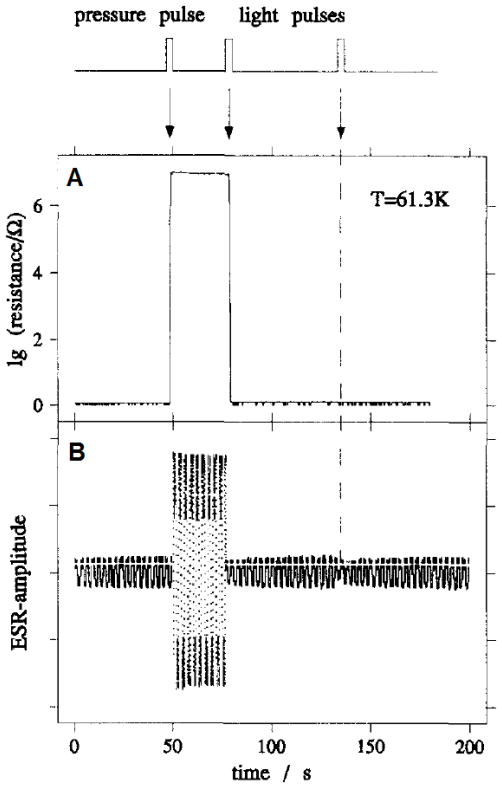

Figure 2.20: Switching of (a) the resistance and (b) ESR-amplitude in Cu(d_6-DCNQI)$_2$ at $T = 61.3$ K with pressure and light pulses. Taken from [54].

indicative of isolated Cu^{2+} states. About 25 seconds later, while still in the insulating phase, a light pulse successfully switches off the resistance, as well as the ESR signal. A further light pulse about one minute later has no further effect, as the crystal remains in the conductive phase.

Lastly, time-dependent conductivity measurements by Karutz. et. al. demonstrated that exposure to an ultrashort (35 ps) laser pulse can switch DCNQI salts from their insulating phase to their conducting phase, within their 35 ps temporal resolution[43]. When photo-switched just below the phase transition temperature (but still within the narrow hysteresis temperature window), this increase in conductivity – which goes up to the full conductive phase – is long-lived (persistent), despite the fact that only the first $\sim$1% of the material is switched. This is again indicative of a domino-effect (as previously shown in figure 2.19). These transient ultrafast conductivity results mark the first observation of the ultrafast photo-induced insulator-to-metal transition in Cu(DCNQI)$_2$, and expose the suitability of the material to find applications in opto-molecular electronics as ultrafast switches. However, fundamental questions concerning the driving forces, selectivity, and the ultimate speed of this light-induced phase transition remain unanswered. Here, a study on the ultrafast microscopic structural (lattice) dynamics, thereby exposing the molecular switching mechanisms, would be desirable. In the work of this thesis, the ultrafast structural dynamics in Cu(DCNQI)$_2$ upon photo-excitation are studied using Ultrafast Electron Diffraction (UED). The experimental method will be introduced in the next chapter. A more comprehensive discussion of the results obtained by Karutz et. al. will be presented in section 4.2.

3. Ultrafast Electron Diffraction

Currently, the preferred method for ultrafast structural dynamics experiments on complex systems, such as organic molecular crystals, is Ultrafast Electron Diffraction (UED). The suitability of UED is attained by the fact that the electron diffraction efficiency is high, combined with a relatively flat Ewald sphere, which results in the provision of access to a large reciprocal space volume. This chapter describes the relevant specifications of our home-built Ultrafast Electron Diffractometer, which is optimised for transmission mode, and its implementation to study the ultrafast photo-induced structural insulator-to-metal phase transition in $Cu(DCNQI)_2$. The details on the development and the full characterisation of the set-up have been previously reported in my MSc thesis [55].

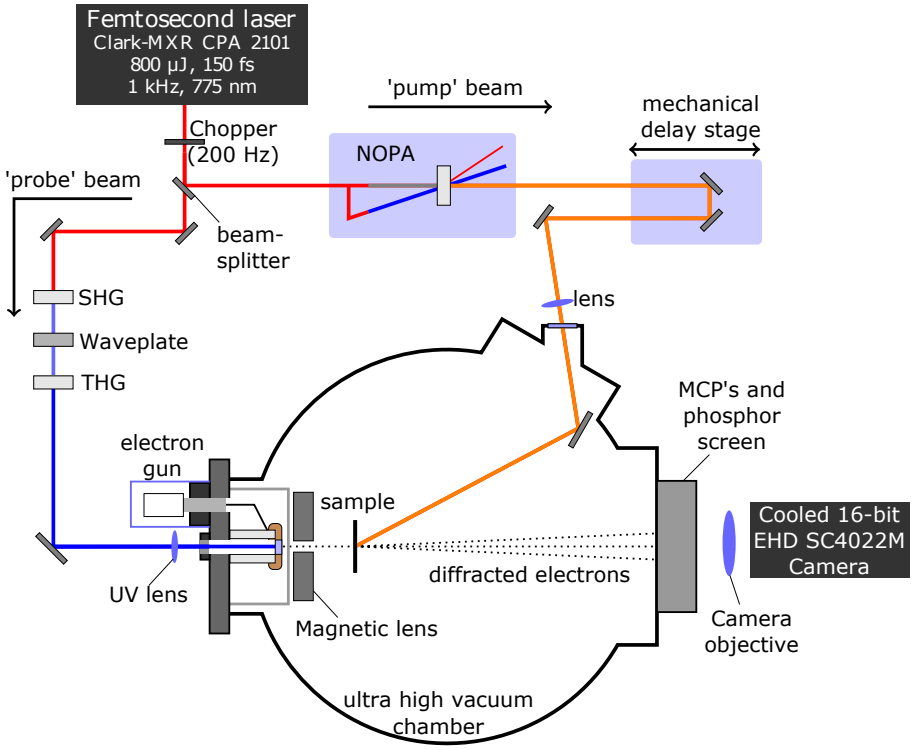

Figure 3.1: The UED set-up, which consists of a femtosecond laser, whose output is split into a pump and a probe beam path. Both paths meet at the sample position, but are temporally separated by a delay time which is determined by the mechanical delay stage position.

In short, pulses from a femtosecond laser are split into a pump and a probe beam by a beamsplitter (labelled in figure 3.1). Ultrashort visible laser pump pulses deposit energy into the sample, thereby optically driving the insulator-to-metal phase transition. Concurrently, optically delayed electron probe pulses capture the structural changes

of the sample by the generation of electron diffraction 'snapshots'. By repeating the experiment for a range of optical delay times (achieved by changing the position of the mechanical delay stage, as labelled in figure 3.1), a full transient of the structural dynamics occurring in the sample upon photo-excitation is captured.

The ability to study the atomic or molecular structure of substances in highly non-equilibrium configurations, allows for the observation of electronic and structural degrees of freedom while a system undergoes a transition. This enables the study of the pathways and driving forces of the transition (or in other words, the potential energy surface governing the direction and final product of the transition). Furthermore, (unexpected) intermediate transient states, that are not accessible in equilibrium structural determination, may also be observed.

In most samples studied with UED, including $Cu(DCNQI)_2$, the sample recovers back to its initial state after photo-excitation. This means that a sample can be exposed to many pump-probe shots, and full transient acquisitions are achievable from a single sample, provided that photo-damage is manageable. The latter imposes additional challenges when UED is performed on organic substances. Molecular solids have poor heat conduction, thermal lability and weak scattering centres. These challenges reduce the upper limit for (1) the repetition rate, (2) pump fluences and (3) number of shots at which the experiment can be performed, ultimately decreasing the obtainable signal strengths. Nonetheless, successful UED experiments on organic crystalline substances have been published, of which examples will be discussed in the first section of this chapter. Section 3.2 and 3.3 will then provide details of our pump and probe beam lines respectively, followed by section 3.4, which is on the preparation of $Cu(DCNQI)_2$ for implementation in UED in transmission mode. Lastly, this chapter will conclude with the experimental procedures followed when performing UED on $Cu(DCNQI)_2$, discussed in section 3.5.

Below, all relevant specifications of the machine are stated (as characterised in the rest of this chapter):

- Operating laser repetition rate: f_{rep} = 200 Hz
- Pump pulse duration: τ_{vis} = 150 fs
- Pump pulse wavelength λ from visible to near-infrared
- Electron energy: E_{kin} = 30 keV
- Electron pulse duration at target: $\tau_e \approx 1$ ps
- Electron beam transverse coherence length at target: $\xi_s \geq 19$ nm
- Electron pulse charge: Q_e = 1.6 fC
- Intensity sensitivity: $\sim 10^{-3}$
- Sample temperature range: T_s = 16 – 355 K
- Sample thickness: 50 – 70 nm
- Final pressure of vacuum at 300 K: $p_{\text{vac}} = 10^{-9}$ mbar

3.1 Ultrafast Electron Diffraction on Organic Crystalline Substances

UED has been able to uncover interesting dynamics in a variety of organic substances, while details to explain macroscopic behaviour were determined. The examples are:

(EDO-TTF)$_2$PF$_6$ The ultrafast molecular motions leading to a charge delocalisation in (EDO-TTF)$_2$PF$_6$, captured with ultrashort electron bunches, was published in 2013[56]. The material is an organic charge transfer salt with a metal-to-insulator phase transition at T = 280 K, which can be photo-induced. By detecting the time-dependent changes of Bragg reflections upon photo-excitation at low temperature, the molecular motions were mapped. From these data, the ultrafast destruction of the low temperature phase ($\sim$ 1 ps), the formation of a transient intermediate state (until $\sim$ 15 ps), and the relaxation to the ground state ($\sim$ 100 ps), have been inferred. Extraction of the responsible molecular motions from UED data was achieved by taking the previously determined hot and cold structures by X-ray crystallography. Structural refinement algorithms were applied to this structure, and calculated structure factors were compared with the experimental intensity maps. By using this method, three independent motions were determined: the flattening of bent EDO-TTF molecules, the shifting of PF_6 molecules, and the sliding of flat EDO-TTF molecules. The sliding of two flat EDO-TTF molecules combined with shifting PF_6 molecules were found to be responsible for the insulator-to-metal phase transition. A follow up UED study on (EDO-TTF)$_2$SbF$_6$ — an EDO-TTF derivative with a larger counter-ion — was published in 2017. In this case, only two of the three motions were recorded, with the motion of the (heavier) counterion not ocurring. As this motion is considered a key mode to enter the metallic phase, an explanation as to why the material is unable to enter the metallic phase upon photo-excitation was uncovered[57].

Diarylethene UED experiments on the a photo-induced ring-closing reaction in diarylethene were published 2013[58]. In order to extract structural information from diffraction patterns, diarylethene molecules were crystallised. Despite their confinement in a crystal, the molecules still showed their characteristic photochromic behaviour. To identify the motions associated with the ring opening and ring closing reaction, again electron diffraction simulations were performed. By again taking steady-state structures obtained with X-ray crystallography as the starting phase and final product, the thiophene rings were found to rotate upon photo-excitation, which opens the ring ($\sim$ 200 fs), leading to a distance decrease between the reactive carbon atoms. The carbon atoms then exhibit localised torsional motions ($\sim$ 5 ps), which leads to the (thermally irreversible) closing of the ring. A second laser pulse pumping the sample was required to recover the starting product, before it could be pumped again, making this work the first UED study on a thermally irreversible transition.

Me$_4$[Pt(dmit)$_2$]$_2$ The molecular motions associated with a photoinduced charge transfer transition were reported in 2015[59]. The stacked planar molecular sheets of P[Pt(dmit)$_2$]$_2$ form dimers, interleaved with Me$_4$P cation planes. When cooled, charge transfer processes lead to the doubling of the a and b unit cell size (at T = 218 K for the investigated compound). Using UED, the molecular motions of the photo-induced

transition from the cold to the hot phase were reconstructed, revealing that in this case, the photo-induced transition is similar to the thermal transition, with three distinct motions (the neutral dimer molecular distance expansion, the molecule flattening, and the simultaneous tilting of dimers) identified. The large size of the unit cell in this work (c = 37.4 Å) demonstrates the potential of UED to investigate ultrafast photoinduced dynamics in large complex systems such as proteins.

[Fe(PM-AzA)$_2$](NCS)$_2$ More recently, the photo-induced ultrafast transformation of the molecular structure of [Fe(PM-AzA)$_2$](NCS)$_2$, a spin crossover (SCO) complex, was published in 2017[60]. The optically excited transition between the low-spin and high-spin state (thermal transition occurring at T = 184 K), both associated with their own molecular arrangement, were studied with UED. Like in previous work, the structure factor changes for selected Bragg peaks were calculated, in an attempt to identify modes responsible for the photo-induced cold to hot structural transition. In this case, two dynamical models were considered, and the best fit model was taken as the most fitting solution to the experimental data. In the chosen model, three independent dynamic groups (a Fe-N bond elongation, coupled to a local unit cell expansion and ligand motion, all happening at the same 2.3 ps time constant) are claimed to represent the photo-induced structural dynamics associated with the spin crossover transition.

In all the above cases, the general approach to interpret time-dependent changes in diffraction signals, is the consideration of the priorly known crystalline structure (from crystallography data) before excitation. The subsequent analysis of small alterations in diffractions pattern during the non-equilibrium phase after excitation then uncovers the pathway towards the final state. We have used a similar approach to interpret our results (chapter 4).

3.2 Optical Pump Beam Characterisation

For our set-up, we use one-third (300 µJ pulse energy) of the the total laser output of a Ti:Sapphire laser (model Clark-MXR CPA-2101), which produces ultrashort near-IR laser pulses (τ = 150 fs, λ = 775 nm) at a repetition rate of 1 kHz. 70% of the laser power available to us goes to our pump beam arm. Displayed in figure 3.2 is the extinction coefficient for $DCNQI^-$ ions in solution, demonstrating the unsuitability of our fundamental wavelength to pump our sample (indicated by the red dashed line). By employing a λ = 620 nm laser pulse (orange dashed line), the sample is optically pumped within the resonance of the molecular $DCNQI^-$ cation. Initial UED experiments that we performed, where samples were pumped at the fundamental laser wavelength (λ = 775 nm), demonstrated that the damage threshold of the sample at this wavelength is lower than the energy needed to drive the metal-to-insulator phase transition in $Cu(DCNQI)_2$ (due to heating of the copper mesh on which the sample is mounted, see section 3.4). To achieve photo-excitation in the orange wavelength range, the output of a Noncollinear Optical Parametric Amplifier (labelled 'NOPA' in figure 3.1) is utilised.

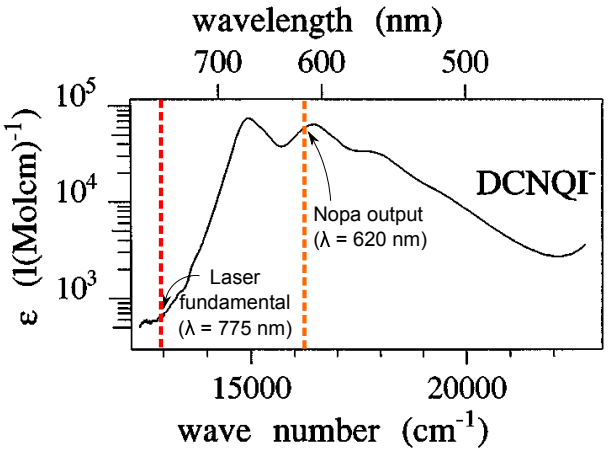

Figure 3.2: The molecular extinction ϵ of $DCNQI^-$ anions in CH_3CN solution, taken at 300 K, indicating higher absorption at orange wavelengths (orange dashed line) compared to near-IR wavelengths (red dashed line). Figure adjusted from ref [43].

The Noncollinear Optical Parametric Amplifier (NOPA) To tune the fundamental wavelength to the desired optical pump wavelength, the NOPA – as depicted in figure 3.3 – is used. The incoming fundamental nIR beam is split by a beamsplitter into P1 and P2. A sapphire crystal generates a white light pulse from the fundamental beam in P1. In the spectrally broadened pulse, spectral components are temporally spread out (i.e. the pulse is *chirped*, not compressed to the Fourier limit). This white light seeds a β-Barium borate (BBO) crystal (labelled BBO 2). Concurrently, in path P2, the fundamental is frequency doubled in another BBO crystal (labelled BBO 1), with the generated λ = 387.5 nm pulses pumping the same BBO 2 crystal that was seeded by the white light from path P1. By tuning the delay stage in path P2 (labelled in figure 3.3), the pump pulse (with frequency ν_{pump}) is spatially overlapped with a selected spectral component of the temporally broadened seed pulse (frequency ν_{seed}). The output idler beam (labelled 'idler') then has a frequency of:

$$\nu_{idler} = \nu_{pump} - \nu_{seed}. \tag{3.1}$$

The NOPA input pulse length is 150 fs, so it is reasonable to assume that the idler is not much longer. Therefore, a significantly longer electron pulse duration ($\tau \approx 1$ ps) in our UED experiment (section 3.3), the pump pulses exciting our sample are not considered the limiting contributor to the temporal resolution in our UED experiments.

Below, it will be discussed that a maximum pulse energy from the NOPA of 0.2 µJ is required to photo-excite the phase transition of $Cu(DCNQI)_2$. Our NOPA can provide a (stable) pulse energy of at least 2 µJ (up to 4 µJ), which is beyond sufficient.

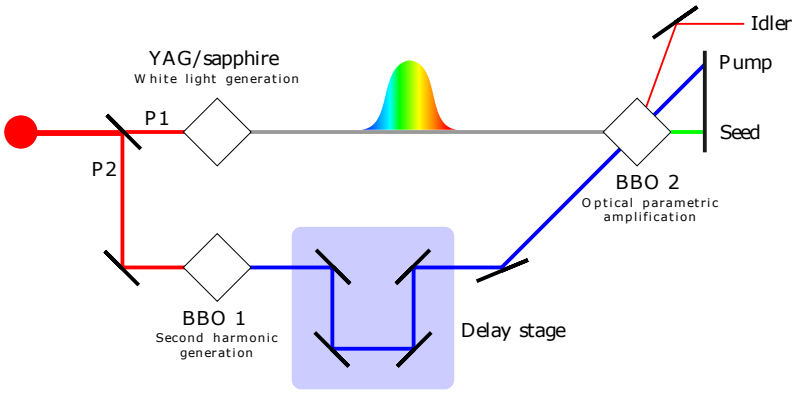

Figure 3.3: Close-up of the in figure 3.1 depicted NOPA, used to generate ultrashort λ = 620 nm pump pulses. Graphic kindly provided by ref. [61].

Pump Beam Fluence Exposing delicate samples to fluences exceeding the damage threshold – known to be low for organic matter[56], and from our experience around $< 2\ mJ/cm^2$ for $Cu(DCNQI)_2$ – destroys the sample, making all preparatory work to start an experiment fruitless. On the other hand, sufficient energy needs to be absorbed by the sample in order to drive the insulator-to-metal transition. Furthermore, knowledge of the energy deposited (and the corresponding approximation of the temperature rise of the sample that this would induce) gives an indication whether a transition is purely thermally driven, or if other selected degrees of freedom (electrons or phonons) are responsible for the transition. So, careful control of the pump fluence received by the sample is crucial. The fluence (F) can be simply determined by:

$$F = \frac{E_{\text{pulse}}}{A_{\text{focus}}}, \tag{3.2}$$

where E_{pulse} is the pulse energy and A_{focus} is the area of the pump beam spot at the sample position. The energy of a single laser pulse E_{pulse} can be easily determined by measuring the average laser power (P_{av}) to which the sample is exposed:

$$E_{\text{pulse}} = \frac{P_{\text{av}}}{f_{\text{rep}}}, \tag{3.3}$$

where f_{rep} is the pulse repetition frequency (or rate), which is 1 kHz for our laser system, which can be reduced by the chopper wheel. The remaining unknown to determine the pump fluence in equation 3.2 is the spotsize area of the pump beam at the sample position A_{focus}. A 1000 mm focal length lens (labelled 'lens' in figure 3.1) is used to focus the pump beam on our sample. We opted to put the sample **in** the focus, so that the spotsize of the beam at the sample position is known in the most accurate way. As this focus is deep inside the vacuum, at a position that is hardly accessible, placing the target within the focal length is not trivial. To find the focus on the sample, photo-electrons from a dense (400 lines/inch) tunnelling electron microscope (TEM) grid, mounted at the sample position, are generated. A shadow image of the grid,

generated using our defocused electron probe beam (with pulses arriving at the grid position *after* the optical pump pulses), is then acquired. Photo-electrons that are generated from the grid as a consequence of the pump pulses, distort the shadow image that is taken, as shown in figure 3.4a. By taking an undistorted (unpumped) TEM grid shadow image, and subtracting the undistorted image from the distorted (pumped) image ($I_\Delta = I_{\text{distorted}} - I_{\text{undistorted}}$), the affected area of the grid is easily exposed (figure 3.4b-e). In this way, the focus position is can be accurately determined well within a single cm.

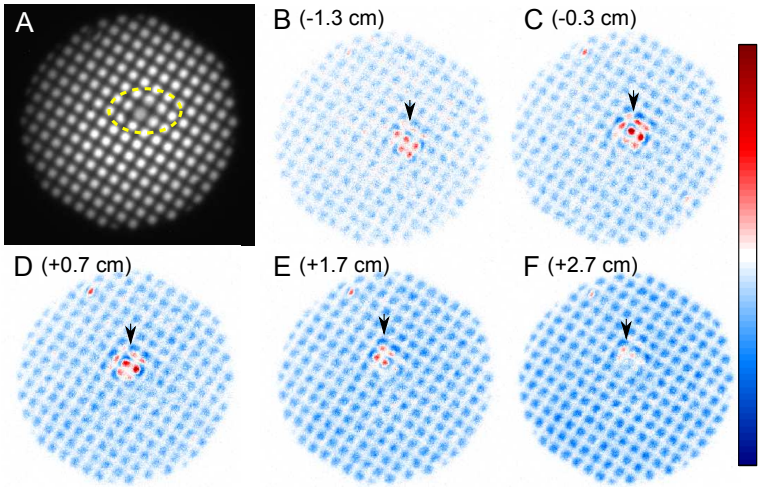

Figure 3.4: (a) Unedited shadow electron image of a mesh, indicating the area distorted by laser-generated photo-electrons. (b-f) Difference images between distorted and undistorted shadow image of mesh, taken at different positions of the lens w.r.t. the focus (indicated in cm).

Now that the sample has been accurately placed in the focus of the laser beam, the spotsize area of the focus, A_{focus}, needs to be determined. The theoretical beam waist in the focus w_0 is given by[62]:

$$w_0 = \frac{\lambda}{\pi\theta}, \tag{3.4}$$

where λ is the wavelength (620 nm) and θ the angular spread, which (for a $\sim$ 5 mm beam waist of the NOPA output, and a focal length of 1000 mm) is approximately 0.005 rad. So, a theoretical beam waist of $\sim$ 40 µm is obtained, corresponding to a theoretical spotsize area of $\sim$ 5000 µm^2. The theoretical Rayleigh length Z_R of this focussing beam is given by:

$$Z_R = \frac{\pi w_0^2}{\lambda} = \frac{\lambda}{\pi\theta^2}. \tag{3.5}$$

The obtained Rayleigh length for our beam is $Z_R \approx 8$ mm. The accuracy of our determination of focal position of figure 3.4 is well within 0.8 cm, which means that a determined spotsize area of the beam focus is an accurate reflection of the spotsize area at the sample position. However, the output of our NOPA is not a perfectly round beam, and the beam is not 100% collimated. So, the theoretical beam waist estimation of the NOPA output is inherently inaccurate. To unequivocally determine the real spotsize of our imperfect experimental beam, a CCD camera should be placed in the focus of the beam. However, as was mentioned, the focus in the vacuum is inaccessible.

Therefore, a reflection from the vacuum laser feedthrough window (after the focussing lens) was taken as a virtual target outside the vacuum. The focus of this reflected beam can be accurately found on the CCD camera by translating the camera along the duplicate pump beam line outside the vacuum (while tracking the beam observed on the camera) in order to find the spotsize minimum. An image of the spotsize minimum of the pump beam is shown in figure 3.5. From this image, an experimental FWHM area of the focus of 8000 μm^2 is determined.

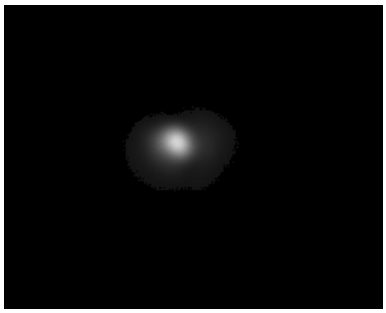

Figure 3.5: CCD camera picture of the pump beam focus.

With A_{focus} known, equations 3.2 and 3.3 can be used to determine the pump fluence. We found a damage threshold for the pump fluence of about 2 mJ/cm^2 (for pumping a 50 nm Cu(Me,Br-DCNQI)$_2$ crystal slice on a 300 lines/inch grid at λ = 620 nm, with 150 fs pulses at a repetition rate of 200 Hz). This damage threshold was found the "hard" way: for numerous experimental attempts, samples melted before the acquisition of the experiment. To pump at the damage fluence of 2 mJ/cm^2, the pulse energy to which the sample should be exposed is 0.16 µJ. With all metal mirrors and a vacuum laser feedthrough after the power meter absorbing 25% of the power, the NOPA output pulse energy should be set to 0.20 µJ. With the maximum output of the NOPA being 2 µJ, such pulse energies are easily accessible.

Energy Absorbed by Cu(DCNQI)$_2$ By using a photodiode to compare the NOPA output power through an empty grid hole, with a grid hole covered with a free-standing 50 nm thin Cu(DCNQI)$_2$ slices (sample preparation will be discussed in section 3.4), the optical transmission of the sample was determined to be 70 $\pm$ 6% for λ = 620 nm. Here, neglectable sample reflectivity was assumed. With a sample area (A_{sample}) of 55 µm $\times$ 55 µm (= 3025 μm^2, see figure 3.6), the absorbed energy E_{abs} by the sample upon photo-excitation corresponds to:

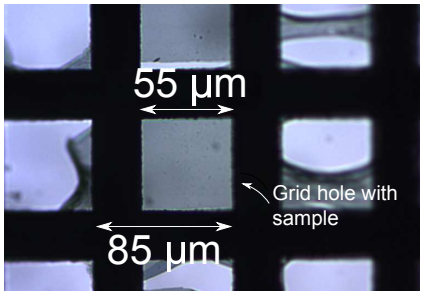

Figure 3.6: a Cu(DCNQI)$_2$ crystal slice, covering a grid hole area.

$$E_{abs} = 30\% \cdot \frac{A_{sample}}{A_{focus}} \cdot E_{pulse,FWHM}. \tag{3.6}$$

Here, within the FWHM of the beam, the beam profile is approximated to have a flat-top energy distribution. To determine the flat-top energy within the FWHM area of the beam, the energy outside the FWHM is neglected. In other words, $E_{pulse,FWHM}$ in equation 3.6 is 78% of E_{pulse} in equations 3.2 and 3.3.

With only 30% of the light absorbed by the sample upon photo-excitation (corresponding to a $1/e$ length of $\sim$140 nm while the sample thickness is 50 nm), and with the laser spotsize being three times larger than the sample area, it is reasonable to assume that the entire sample volume is photo-excited approximately homogeneously.

To get an intuitive feeling of how 'hard' our Cu(DCNQI)$_2$ samples are pumped, an estimate of the number of photons absorbed per unit cell is calculated. In the experiment where our sample is pumped the hardest (results are discussed in chapter 4), the total absorbed pulse energy E_{abs} is 13.7 nJ. The energy of a single photon is:

$$E_{\lambda=620} = \frac{hc}{\lambda} = 2eV (= 3 \cdot 10^{-19} J), \tag{3.7}$$

meaning that the total number of absorbed photons is 13.7 nJ / 3· 10^{-19} J = 4.56 · 10^{10} photons. The sample shown in figure 3.6 has a thickness of 50 nm (as will be discussed in section 3.4), making the total sample volume 55µm × 55µm × 50 nm = 1.51 · 10^{-19} m^3. The volume of our unit cell is 21.9 Å× 21.9 Å× 3.8 Å= 1.51 · 10^{-16} m^3. So, the total number of unit cells within our sample volume, obtained by dividing these two values, is 8.3·10^{10}. Conclusively, the number of photons absorbed by a single unit cell is:

$$\frac{4.56 \cdot 10^{10} \text{ photons}}{8.3 \cdot 10^{10} \text{ units}} = 0.55. \tag{3.8}$$

By combining the determined absorbed pulse energy upon photo-excitation (E_{abs}) with the known molar heat capacity of $Cu(DCNQI)_2$ (C), an eventual temperature rise (T_{rise}) as consequence of pumping at a certain fluence can be estimated. Shown in figure 3.7 is the temperature dependent molar heat capacity of $Cu(DCNQI)_2$[63]. As this graph behaves approximately linear, especially at narrow temperature ranges over which we would pump the samples, the average of the molar heat capacity at the starting temperature (before pumping) and the final temperature (after pumping) must be taken.

$Cu(DCNQI)_2$ has a molar mass (M), of 562 g/mol, while it has a volumetric mass density (ρ) of 2.072 g/cm^3. So, the total mass of material within the grid hole of figure 3.6 is $m_{sample} = \rho \cdot V_{sample}$ = 3.13·10^{-10} g, corresponding to n = m_{sample} / M = 5.64 · 10^{-13} mol. Conclusively, the estimated temperature rise of our crystal is:

$$T_{rise} = \frac{E_{abs}}{n \cdot C}, \tag{3.9}$$

where E_{abs} is the same as in equation 3.6.

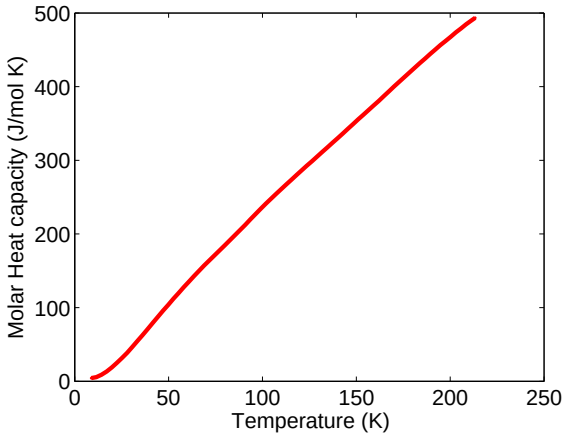

Figure 3.7: Molar heat capacity of $Cu(DCNQI)_2$. Data provided by [63].

When pumping the sample through the phase transition, the latent heat across the transition needs to be taken into account, which was determined to be Q_{lat} = 950 J/mol for $Cu(Me,Br\text{-}DCNQI)_2$[63]. When our sample is pumped through the phase transition, the energy consumed by latent heat is $Q_{lat} \cdot n$, which is 5.0·10^{-10} J. In other words, 2.5 K needs to be subtracted from T_{rise} when pumping through the phase transition:

$$T_{rise} = \frac{E_{abs}}{n \cdot C} - \frac{Q_{lat}}{C}. \tag{3.10}$$

In conclusion, by using the calculations above, an estimated temperature rise for the experiments performed at 1.02 mJ/cm^2 and 1.93 mJ/cm^2 (chapter 4) are 36 K and 70 K respectively.

3.3 Electron Probe Beam Characterisation

The electron pulses, which are probing the ultrafast photo-induced transition, must be capable of resolving the atomic structure of $Cu(DCNQI)_2$, and must have sensitivity to small sub-Angström atomic displacements that are associated with the transition. Figure 2.3d in the previous chapter, showing $Cu(DCNQI)_2$ in the low temperature trimerised phase, revealed that we indeed have sufficient spatial resolution to capture both phases (and the transition from the one to the other upon photo-excitation, as will be shown in chapter 4). How the spatial sensitivity requirements are met by the ultrashort electron pulses will be discussed in section 3.3.2. Furthermore, to track ultrafast processes such as transfer of energy from the electronic to the lattice structure, high temporal resolution is needed. Section 3.3.2 aims to numerically and experimentally characterise the temporal resolution of our system, showing that our pulses have a temporal duration of $\sim$1 ps. This chapter will start by discussing the generation of ultrashort electron pulses in the probe path of figure 3.1.

3.3.1 Ultrashort Electron Pulse Generation

To convert ultrashort laser pulses into ultrashort electron pulses, the photo-electric effect is utilised on a 10 nm gold film in a 30 kV DC electron gun. In a previous characterisation of a pulsed electron gun, the Fermi energy level E_F of a gold film was 5.5 eV, with an estimated effective work function Φ_{eff} of 4.2 eV[64]. When photo-electrons on such a gold foil are generated in a 1-photon process (i.e. by matching the photon energy with Φ_{eff}), the shot-to-shot charge fluctuations of electron pulses are proportional to fluctuations of the laser pulses $\propto I$. If we would have generated electrons at our fundamental (E_p = 1.6 eV), three photons would have been needed to generate one electron, which would the electron charge fluctuations with $\propto I^3$. Furthermore, by not letting the photon energy exceed the work function, generated electrons have a lower initial energy spread (typical excess photon energy around 0.5 eV above the work function for our system[65]). This minimises the spread in spatial and temporal directions when the electron bunches drift through a vacuum after acceleration in an electric field (in this case still neglecting space charge effects). To minimise electron pulse charge fluctuations and initial electron energy spread, we utilise the tripled of the fundamental frequency for photo-electron generation, with E_p = 4.8 eV being a close match to the work function of our cathode.

Third Harmonic Generation To generate the third harmonic in the probe beam (as indicated in figure 3.1), Second Harmonic Generation (SHG) is firstly achieved in a BBO crystal. The polarisation of the SHG pulses are then rotated so that it matches the polarisation of the co-existing fundamental pulses. This ensures phase matching conditions in a second BBO crystal, resulting in Third Harmonic Generation (THG, see figure 3.1), achieved by taking the sum frequency of the fundamental and the second harmonic. The product is the third harmonic – a pulsed UV beam (λ = 258 nm) – which is focussed onto the cathode in the electron gun, of which a sketch is shown in figure 3.8. As the gold layer is mostly transparent to the UV beam, photo-electrons are generated throughout the whole gold layer. However, the excess energy of the electrons is low ($\ll$ 1 eV), meaning that only the electrons generated at the surface of the film make it out of the material[65]. Therefore, the initial pulse duration of the generated

electron pulses is identical to that of the UV laser pulses[66]. The cathode at which the 150 fs electron bunches are generated is at -30 kV, which results in the acceleration of the electron bunches towards a grounded anode, see figure 3.8. The electric field strength in the cathode-to-anode region is approximately uniform (as the cathode and anode have a flat shape), with $E = 6$ MV/m. The electron pulses leave the gun through the anode extraction hole, enter the drift region with $E_{kin} = 30$ keV (with the speed of the electrons corresponding to $v_e \approx c_0/3$, where c_0 is the speed of light). A magnetic lens (which is a copper coil through which an electric current can flow) ensures that the beam is focussed onto the detector. The sample under investigation is placed in the electron beam path.

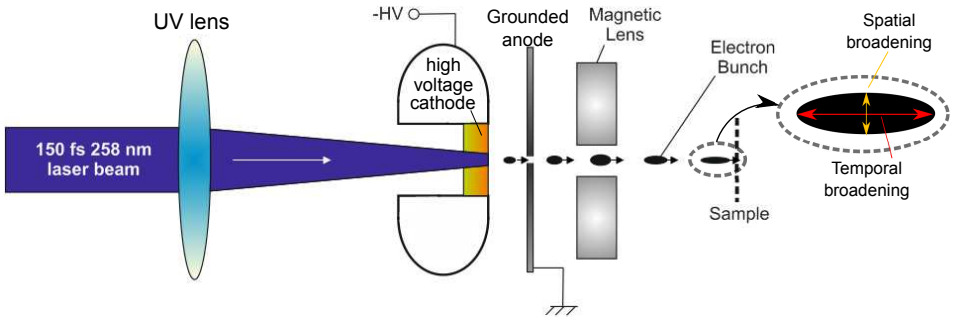

Figure 3.8: Zoom-in of electron generation in probe beam line in figure 3.1. UV pulses are focussed on a gold film at -30 kV, thereby photo-electrically generating electron pulses. These are accelerated in a high electric field, focussed by a magnetic lens. They subsequently drift through the sample, while they are debunching in both spatial (orange arrow) and temporal (red arrow) direction.

Illustrated in the dashed region of figure 3.8 is the temporal (red arrow) and spatial (orange arrow) pulse broadening due to space charge effects. The spatial and temporal broadening due to Coulomb repulsion between electrons squished in a short pulse, worsens the specifications of UED machines.

Alternative Electron Sources With space charge effects being a big limiting factor for UED, alternative electron sources have been developed. Firstly, Coulomb repulsion is eliminated when using single-electron pulses[67]. However, temporal resolution is still limited by jitter ($\sim$100 fs). Furthermore, at least $\sim 10^6$ electrons are needed to obtain a reasonable diffraction pattern. This means that a million shots (and therefore repetitions) at each temporal position needs to be taken for the single electron approach (which is about 1000 times more than our experiment in chapter 4). This greatly increases the experimental acquisition time, and delicate organic samples may not survive for this many shots. Organic materials also take a longer time to go back to the ground state after photoexcitation, greatly limiting the upper limit of the repetition rate. The single electron approach could be suitable for UED experiments on gasses, although there the scattering probability is much lower.

Secondly, short electron beams with ultra high coherence can be generated from nanotips [68–71]. Such guns were in the proof-of-principle phase, but very recently the first experiment on a phase transition in inorganic 1T-TaS_2 has been published, demonstrating the large transverse coherence length at sample position ($\xi_s = 21$ nm) of such sources, but still limited temporal resolution ($\tau = 16$ ps)[72].

Thirdly, to reduce the effective electron temperatures of electron bunches, an ultracold electron source was developed. Here, a coherence length of 20 nm was obtained[73]. The pulse direction was ps, but post-generation compression can still improve this[74]. However, no time resolved experiments on the ultrafast dynamics in samples using this technique have been reported.

Lastly, operating at relativistic MeV electron energies negates space charge debunching[75–77]. Furthermore, using relativistic electron bunches solves the problem of the velocity mismatch between the electron probe and laser pump that is present in the case of 'slow' electron bunches. This enables the possibility to do experiments on thick samples (such as samples in the gas phase). MeV electron beams are generated in a gigahertz RF photocathode electron gun, in which field strenghts can go up to 100 MV/m, thereby producing electron pulses that are short (102 fs RMS), bright (60 fC) and coherent (normalised emittance 18 nm-rad)[78]. These impressive machine specifications untie the potential to perform single shot UED experiments on samples, as – for example – was recently done in an experiment that investigated the atomic structural changes of warm dense matter, generated from a single-crystal gold foil by laser-excitation[79]. Before that, the melting of single crystalline gold, using 3.5 MeV relativistic ultrabright 100 fs electron bunches, had already been published [80]. Furthermore, very recently the electron-lattice energy relaxation in thin film Au-insulator heterostructures was investigated with 3.7 MeV electron pulses[81].

Although, clearly, UED machines employing MeV electron bunches are capable of obtaining high quality data, they are not table-top set-ups, but large collaborative projects which are technologically and financially expensive. Furthermore, until now, all UED experiments on complex organic molecular systems (as was discussed in section 3.1), employ the more straightforward non-relativistic UED approach, as – for now – the simplicity of this technique makes it more suitable to investigate such complex systems.

Taking relativistic electron energies one step further, relativistic GeV electron bunches generated from laser-induced plasma-waves have been reported[82], which are possibly suitable for ultrafast structural dynamics experiments in the future.

First Generation DC Guns and RF Compressors Although results from the mentioned variety of methods for ultrashort electron bunch generation are promising, and the sustainable progress of ultrafast structural dynamics investigations relies on the continued development thereof, in this thesis the technological simplicity of a 'first generation' DC electron gun is chosen as the preferred method. Many of these UED machines employ post-acceleration compression of debunched electron pulses by an RF compressor[83] to counteract space charge effects and improve temporal resolution. RF compression utilises the perfectly linear chirp properties manifested by debunched electron pulses[84], making them suitable for recompression. Here, the idea is that a rapidly changing electric field acts as a temporal lens, by decelerating the (fastest) electrons at the front, and accelerate the (slowest) electrons at the back of the electron bunch. The sample should then be placed in the temporal focus. Highly bright electron sources with high temporal resolution (430 fs and 334 fs for 200fC and 100 fC in ref. [85] and [86] respectively) are currently operational using these techniques.

Fitting a gun with an RF compressor, however, adds experimental difficulties as the RF compressor needs to, for example, be perfectly synchronised with the laser source, and it is prone to jitter issues. For our set-up we opted to not use a (financially and ex-

perimentally) expensive compressor for signal improvement, but we rather depend on the reliability and simplicity of the generation of electron pulses of lower brightness in a first generation compact DC-gun without compressor. Furthermore, it turns out that the study on $Cu(DCNQI)_2$ in our set-up requires a full optimisation of the coherence length (this will be discussed in section 3.3.2), as the diffraction signals related to the superstructure in our material under investigation are close to the noise level. Temporally compressing electron pulses increases debunching in spatial direction, meaning that our coherence length would have worsened in case of post-acceleration electron compression, would have complicated the observation of the $3c$ superstructure in $Cu(DCNQI)_2$.

To still ensure best possible spatial and temporal specifications in uncompressed electron bunches, there is a great incentive to increase the operation voltage of DC guns. Working at high voltages effectuates a larger gun acceleration region, with higher field strengths, effectively negating debunching effects[87]. However, working at extremely high voltages, and working close to the practical field strength limit of 10 MV/m, does unquestionably introduce technological challenges. Our gun operation voltage is 30 kV, with an anode-cathode separation distance of 5 mm, corresponding to a field strength of about 6 MV/m. Our sample is placed as close to the gun as possible (but still after the magnetic lens), such that the drift region (and therefore bunch broadening) is minimised. Furthermore, the electron bunch charge is kept to low values, which reduces debunching, but unfortunately also diminishes signal strengths.

Electron Diffraction Detection In our set-up, the electron bunches drift for about 40 cm after diffracting from the sample. They subsequently hit a chevron pair of Micro Channel Plates (MCPs, see label in figure 3.1), with an open-area-ratio of 60%, which amplifies the electron signal with $> 10^8$. To reduce background noise coming from scattered pump laser light, the front MCP plate is coated with an aluminium layer, which blocks light while transmitting electrons. To eliminate background noise coming from (low energy) photo-electrons generated by the pump laser beam, the potential of the front MCP plate is set to -30 V, thereby repelling low energy electrons while still transmitting diffracted 30 keV electrons. The amplified electron signal is then accelerated towards a phosphorescent screen (mounted on a vacuum window), which converts the electrons into photons (with a conversion efficiency of $\eta = 0.063$ photons/eV/electron), making the generated diffraction patterns visible to the outside. This light is collected by a camera objective (as labelled in figure 3.1), and photographs of these patterns are taken by a 16-bit cooled CCD camera.

3.3.2 Spatial Resolution

To be sensitive to atomic structure, the de Broglie wavelength of the electron beam needs to be shorter than the shortest lattice parameter, such that the diffraction limit is surpassed. The de Broglie wavelength λ for non-relativistic electrons is given by:

$$\lambda_{dB} = \frac{\mathrm{h}}{\sqrt{2\mathrm{m}_e E_k}}. \tag{3.11}$$

Here, h is Plancks' constant, m_e the rest mass of an electron, and E_k the kinetic energy of the electron. In our case of $E_k = 30$ keV, this corresponds to a sufficiently low effective wavelength of 0.071 Å.

Additionally, the coherence properties of the electron pulse need to be sufficient. The transverse coherence length, which characterises the ability of the beam to constructively interfere from two scattering centres that are far apart, is a measure commonly used in UED to characterise spatial resolution. The transverse coherence length should overlap with at least the longest lattice constant under investigation – which is 21.8 Å for $Cu(DCNQI)_2$ – to achieve collection of the required structural information.

The lower limit of the transverse coherence length at the sample position ξ_s of an electron beam is given by[88]:

$$\xi_s \leq \xi_i \frac{w_s}{w_i}, \tag{3.12}$$

where ξ_i is the initial transverse coherence length. To optimise for spatial coherence, the initial spotsize of the electron beam generated at the cathode, w_i, should be minimised. Furthermore, having a smaller initial spotsize increases the spotsize at the sample position, w_s, which further improves ξ_s. The initial spotsize w_i is determined by the spotsize of the UV beam on the cathode. By using the shortest focal length UV lens possible to focus the UV pulses on the cathode (f = 100 mm) and by having the cathode in the focus, a minimum spotsize FWHM diameter of 3.3 µm is obtained (figure 5.2 in reference [55]). As electron bunch duration and spatial resolution are a complex interplay, where a trade-off between the two needs to be made, our small initial spotsize does unfortunately lower the temporal resolution[1].

Transverse coherence length determination The intensity distribution $I(\theta)$ from a N-slit diffraction pattern (generated by a monochromatic plane wave), can be derived using geometrical optics[62]:

$$I(\theta) \propto \frac{\sin^2[\pi N(d/\lambda)\sin(\theta)]}{\sin^2[\pi(d/\lambda)\sin\theta]}, \tag{3.13}$$

where N is the number of slits, d the slit separation and θ the diffraction angle. An example case for $N = 7$ and $d/\lambda = 5$ is shown in figure 3.9. It can be shown that $N = x/\Delta x$, where x is the distance between two diffraction peaks and Δx the FWHM of a peak. The coherence length is then given by $d \cdot x/\Delta x$. The equivalent for the transverse coherence length of the electron beam at sample position is given by:

$$\xi_s \geq a \cdot \frac{x_{a*}}{\Delta x_{a*}}. \tag{3.14}$$

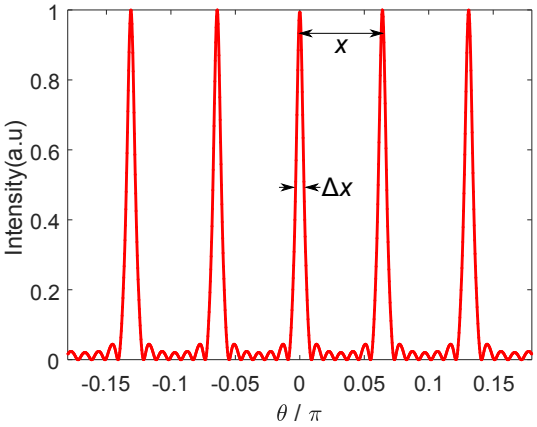

Figure 3.9: Multiple slit intensity distribution for 7 slits, with peak width Δx and peak separation x indicated.

So, when the crystal constant a is known, the transverse coherence length ξ_s can be directly extracted from an acquired electron diffraction pattern by determining the peak-to-peak separation along a^* (Δx_{a*}) and the FWHM width of the peak along a^* (x_{a*}). The obtained

[1] A full experimental and numerical characterisation of the interplay between transverse coherence length and temporal resolution is given in figure 12 of ref [88]. In this thesis, however, only the temporal resolution after coherence length optimisation is characterised (section 3.3.3)

value from a diffraction pattern serves as a lower limit of the transverse coherence length, as imperfect samples (such as the sample having a 'wavy' surface) leads to peak broadening. Furthermore, the Debye-Waller effect also broadens the diffraction peaks for $T > 0$ K. In other words, the highest lower bound of the transverse coherence length from a pattern acquired in our diffractometer – ever – should be considered. In our case, the longest coherence length was observed on inorganic WS_2, which has a hexagonal crystal structure, of which the diffraction pattern is shown in figure 3.10 (left). The probed sample area consists of microcrystals on a carbon coated mesh. In this pattern, many single crystals – with uncorrelated orientation – are probed at the same time, hence a ring diffraction pattern is observed. However, the single peak hexagonal diffraction patterns can still be identified (indicated by circles in figure 3.10). The orange box drawn in the pattern indicates where an intensity line-out of the pattern, shown on the right, is taken. Δx and x are indicated in the line-out intensity profile. With $a = 3.126$ Å for WS_2, the obtained transverse coherence length for this diffraction pattern is to 19 nm, which to our knowledge is one of the best transverse coherence lengths from ultrafast electron guns in UED. As 19 nm $\gg$ 21.8 Å (the latter being our largest crystal constant under investigation), the coherence length in our electron diffractometer is sufficient.

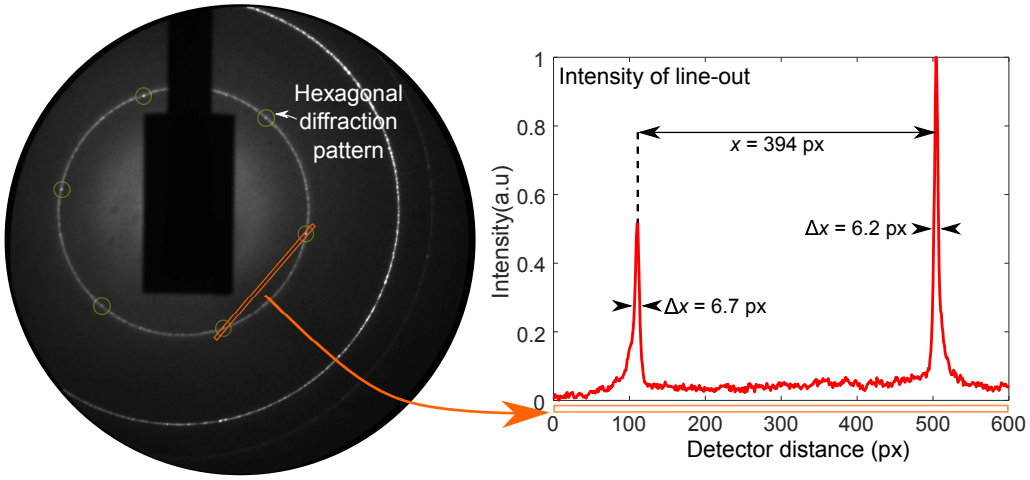

Figure 3.10: Diffraction pattern of inorganic WS_2, with hexagonal pattern identified (left). Intensity of the indicated line-out in the diffraction pattern (right).

Transverse coherence length optimisation It was mentioned that in order to obtain best possible coherence length, the UV lens (which focusses the UV pulses onto the cathode for photo-generation) should be put at the position along the beamline, where the beam spot on the cathode is smallest. To obtain optimised coherence length (and thus lowest Δx_{a*}), the diffraction spot widths should be minimised. Figure 3.11 shows a diffraction peak from WS_2 for three different UV lens positions, each 1 mm apart. Clearly, the beam is focussed on the cathode for the situation in the middle figure. As we opt to perform UED experiments at optimised transverse coherence conditions, the lens position should be kept at this position.

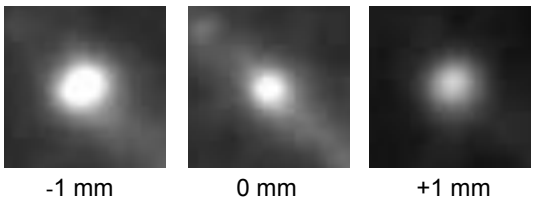

Figure 3.11: An electron beam, diffracted of WS_2, for three UV lens positions.

3.3.3 Temporal Resolution

The temporal system response of our UED system is determined by:

- The laser pump pulse duration (150 fs),
- The stepsize accuracy of the delay stage. One step corresponds to 17 fs (see section 3.5.2), so the uncertainty in delay time arising from stepsize inaccuracy will be much less than that,
- Jitter of the electron beam due to minor high voltage fluctuations ($\sim$ 50 fs),
- The electron probe pulse duration.

The electron pulse duration, to be determined in this section, has by far the largest contribution to the overall temporal resolution and therefore determines the system response.

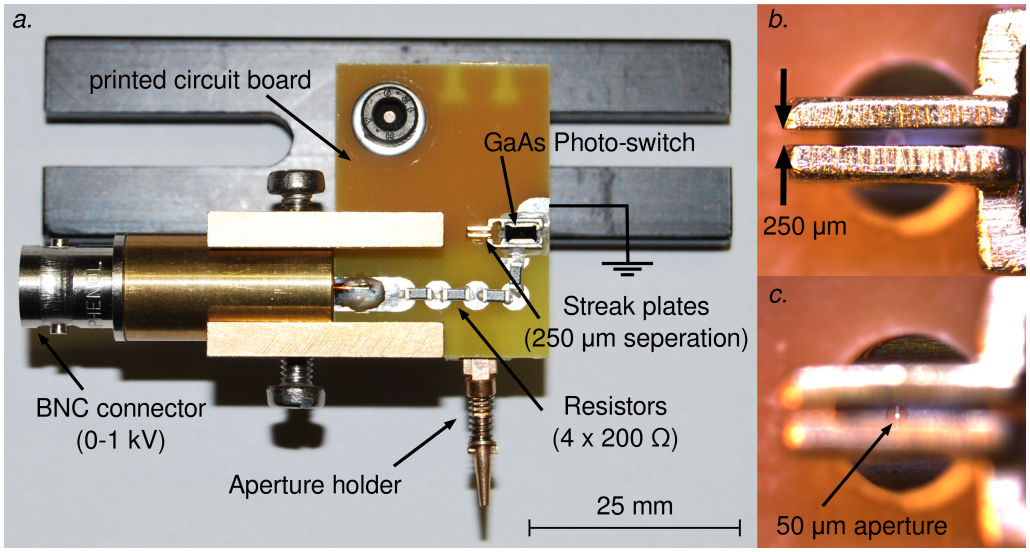

Figure 3.12: (a) The compact streak camera. (b) The streaking plates. (c) The pinhole, used for electron bunch alignment.

The most direct way to observe the (upper limit) of the electron pulse duration, is to temporally map out the ultrafast dynamics in a sample. The electron pulse duration can not be longer than the extracted time constant from such a measurement, but it can be shorter if the ultrafast dynamics are slower than the electron pulse duration. Alternatively, by employing the ponderomitive force exerted on electrons by electron-laser pulse cross correlation, the electron pulse duration can be effectively determined within 100 fs accuracy[89]. However, due to the effort required to set up a ponderomotive scattering measurement, it is unpractical to – during a time resolved measurement on a sample – use the technique to swiftly determine pulse duration without major disruptions. Therefore, a compact streak camera – able to measure electron pulse durations with 150 fs accuracy – was developed by Dr. Günther Kassier in our group[66]. The apparatus, shown in figure 3.12a, consists of two electrodes (figure 3.12b). One of the electrodes is charged (500 V), but is electronically decoupled from the other electrode by an insulating GaAs photo conductive semiconductor switch, whose conductivity is triggered by a laser pulse. When the circuit is closed by laser excitation, a RC circuit establishes a damped oscillation of f = 5 GHz, causing the

strong electric field between the two streaking plates to oscillate. When an electron beam is aligned through the plates (by using an aperture, figure 3.12c), this strongly changing electric field spatially streaks the temporally broadened pulse, provided that the timing of the oscillation is correct. The arrival time of the laser pulse on the GaAs switch is chosen such that when the electron bunch passes through the streaking plates, the voltage ramp is maximum ($\Delta V/\Delta t = 8\,\mathrm{kV/ns}$). This is simply done by selecting the temporal part of the oscillation with the largest slope. By having maximised the electric field change ($\Delta E/\Delta t$), the largest possible spatial streaking of a temporally broadened electron pulse is achieved. This is the case when the streaked beam is centered around the unstreaked beam. With the streak camera ramp rate known, the electron bunch duration can then be calculated from the length of the streak observed on the detector. An example of streaked electron beams are displayed in figure 3.13, clearly demonstrating increased electron pulse duration for larger bunch charge.

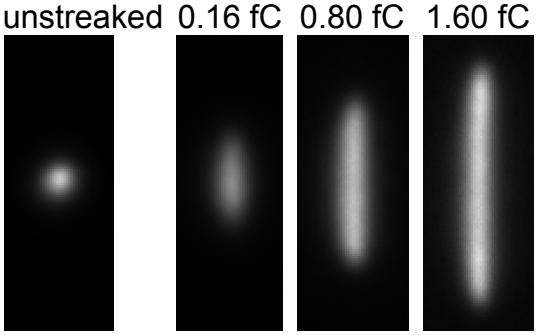

Figure 3.13: An unstreaked and three streaked electron beams, for increasing bunch charge. Figure adapted from [90]

To determine temporal resolution in our ultrafast electron diffractometer, results from the compact streak camera are supplemented with numerical results. Numerical electron debunching calculations are performed using ASTRA (abbreviation for A Space TRacking Algorithm, developed by Klaus Floettmann at DESY[91]). The electric potential from the gun and the magnetic field from the magnetic lens – both calculated using Poisson/Superfish[92] – are fed into the space charge simulations to calculate the electron debunching properties for the conditions in our electron gun (a full explanation of simulation procedures is documented in chapter 4 of reference [55]). Previously performed streak camera measurements and space charge simulations showed the good agreement between electron pulse durations obtained from streak

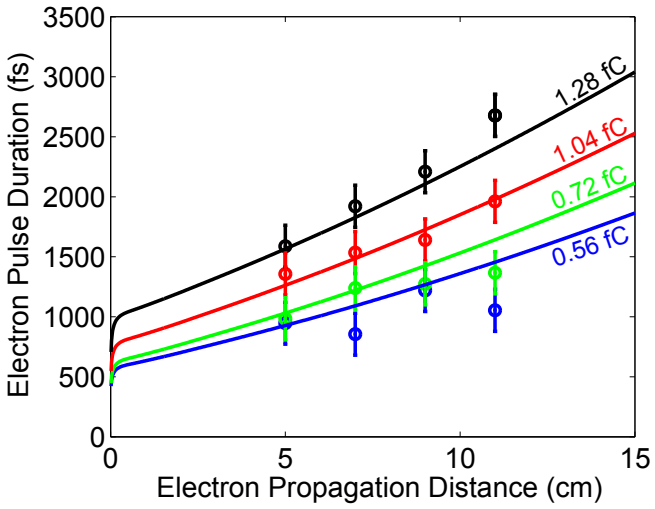

Figure 3.14: Previously determined pulse durations by streak camera measurements (circles) and ASTRA simulations (lines) for increasing bunch charge.

camera measurements and numerical calculations (figure 3.14).

To estimate the electron pulse duration for the conditions under which the results in chapter 4 are measured, a simulation for the real experimental conditions was performed, which are the following:

- A cathode-anode separation distance of 5 mm, corresponding to an electric field of 6 MV/m (for V = 30 kV),
- An initial spotsize of 5 µm,
- An initial electron bunch duration of 150 fs,
- A bunch charge of 1 fC, corresponding to 6000 electrons, which is the bunch charge used in our measurements of chapter 4. This is measured with a simple Faraday cup and a picoamp-meter with a resolution of 10 fA (which for a repetition rate of 1 kHz corresponds to a sensitivity of 0.01 fC per pulse).

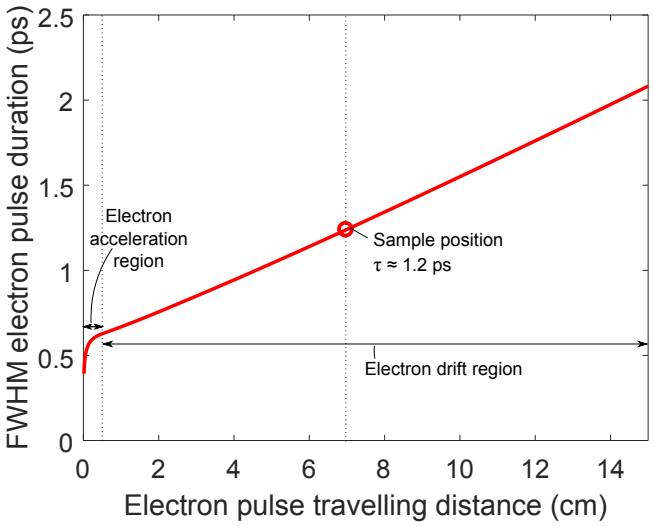

Figure 3.15: An ASTRA simulation, performed for our estimated experimental conditions (see text), demonstrating a predicted temporal resolution of ∼1.2 ps.

The result of this simulation is shown in figure 3.15. With an estimated cathode-to-sample separation of ∼70 mm, our estimated system response is approximately 1.2 ps, as shown in the graph. This value of our system response is used for the data fitting procedure in section 4.2.

3.4 Sample Preparation

To enable adequate probing of an entire sample volume, UED is performed in transmission mode. For electrons with E_{kin} = 30 keV, this inevitably requires ultrathin samples. We found that samples of 50 – 70 nm thickness generate the best diffraction patterns. Bulk needles (figure 3.16a) were grown using electro-crystallisation by Dr. Florian Hüwe in the group of Prof. Dr. Jens Pflaum (Experimentelle Physik 6, Würzburg University). These needles are approximately 100µm thick and wide, corresponding to the *a*,*b* crystal axes. The long conductive *c*-axis of the needle can be up to several

centimetres long. To prepare the samples for feasible UED implementation, they are sliced into 50 nm thin cuts with an ultra-microtome along the *a*,*c* (=*b*,*c*) axis, such that sensitivity to the superstructure formed along the *c*-axis in the low temperature phase is maximised.

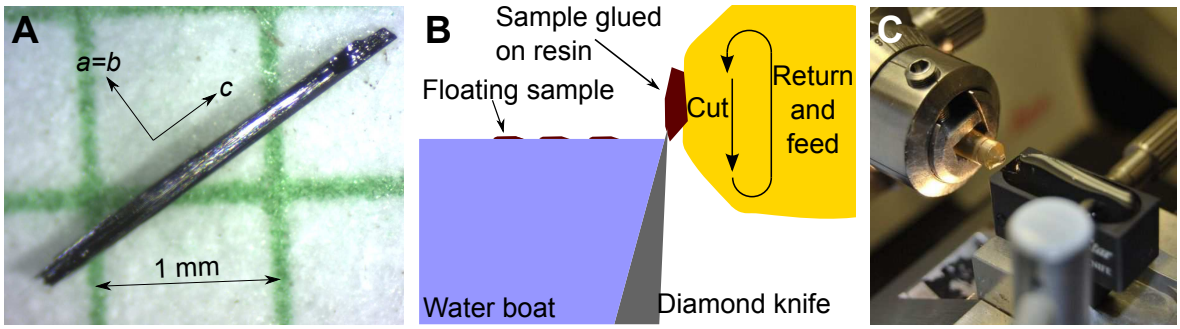

Figure 3.16: (a) A bulk Cu(Me,Br-DCNQI)$_2$ needle with crystal axes indicated. (b) A sketch of the sample glued to a resin cone which approaches a diamond knife in an ultramicrotome. Cut crystal slices float on water. (c) Photograph of the microtome arm, with the resin and sample mounted onto it. The diamond knife and water boat are mounted below. Figure adjusted from ref. [93].

To prepare the samples, a microtome arm (with a resin to which a needle fragment is glued) approaches a diamond knife with step sizes of 50 nm (sketched in figure 3.16b). Slices cut from the fragile soft crystal (compared to inorganic crystals, which are held together by stronger intermolecular forces), are then floated on water. Although the organic radical ion salt should be soluble in water, we found that this is the only effective liquid. Subsequently, these slices are picked up with a TEM grid, to which they stick upon drying. The product, a UED proof free-standing 50 nm Cu(Me,Br-DCNQI)$_2$ single crystal, was previously shown in figure 3.6. Its thickness corresponds to only about twenty unit cells along the *a*,*b* axes, with typical slice lengths and widths of 100 µm, leading to the extremely high aspect ratio of 1:2000.

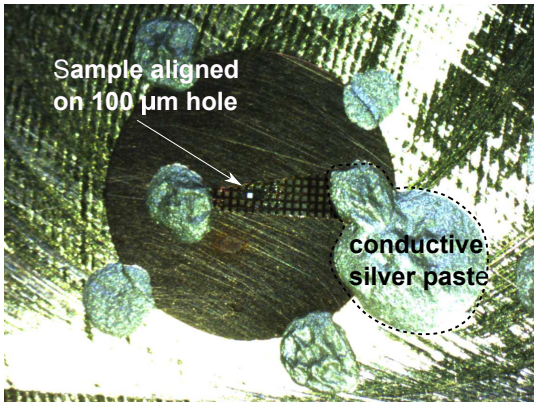

Figure 3.17: Chopped sample grid with a grid hole covered in a monocrystalline slice glued on an aperture.

A high quality crystal slice is often surrounded by broken, polycrystalline, by-product. To eliminate undesirable diffraction from these low quality sample areas, the sample is mounted onto a 100µm aperture in the sample holder with vacuum compatible conductive silver paste – ensuring good thermal conductivity. Hereby, bad sample areas are blocked out from the electron beam. This final product (figure 3.17) is then loaded into our ultra high vacuum chamber, aligned into the electron beam, after which diffraction patterns are generated (section 3.5.1).

Succesful microtoming requires patience, precision and a lengthy experiental training period. The difficulty in preparing samples for UED implementation exposes the biggest reason as to why only a handful of successfull experiments on complex samples have been performed to date, as sample availability is limited, combined with notori-

ously difficult preparation methods. The challenging microtoming task was performed by Ms Nancy Payne, who reported on an extensive 'recipe' for the process [61].

3.5 Experimental Procedures

3.5.1 Steady State Diffraction Patterns

Prepared samples are loaded into the ultra-high vacuum chamber ($p_{300K} \approx 10^{-9}$ mbar) using a sample loader, diminishing the need to break the vacuum. Steady-state room temperature electron diffraction patterns are subsequently acquired to determine the quality of the crystal. 'Good' patterns show single peaks (for monocrystalline samples), exhibit low background scattering, and have round Bragg peaks with sufficient diffracted intensity. An example of such a pattern that is acquired from a sample is shown in figure 3.18(left).

Samples have been through many damaging processes before patterns are taken: they consist of only twenty unit cells along the thin cut, are mounted on a mesh with tension, were cut with a knife, and were floated on water. To confirm that the sample – despite everything – still exhibits structural properties of the bulk, the pattern is compared with a calculated electron diffraction pattern (details on the electron diffraction calculation method are explained in section 4.1.3 and 4.2.2). For the simulated pattern (figure 3.18, right), the known Cu(Me,Br-DCNQI)$_2$ structure from X-ray crystallography measurements is used[2]. In this particular example, a best match of the simulation for the experiment was found by tilting the sample around the a (or b) axis with 3° in the simulation (no tilt around c). So, by comparing simulations with experiments, the orientation of the sample with respect to the electron beam can be determined, which will turn out to be useful for our data interpretation in chapter 4. Furthermore, the good agreement between the experiment and simulation in figure 3.18 indicates that

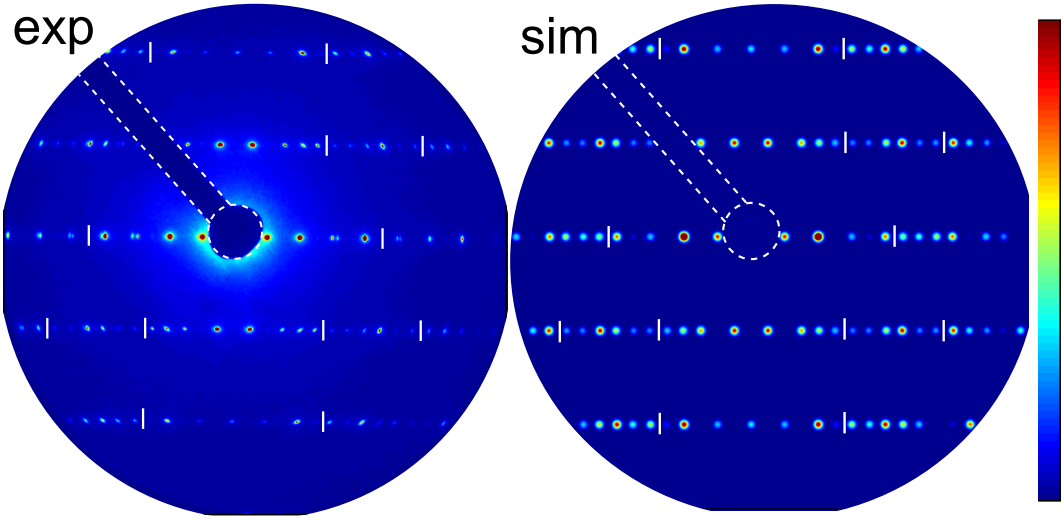

Figure 3.18: Measured electron diffraction pattern of Cu(Me,Br-DCNQI)$_2$ (left), with a simulated pattern based on the known Cu(Me,Br-DCNQI)$_2$ bulk structure (right). White lines are included to facilitate easy comparison.

[2]The X-ray crystallography measurements were done by Dr. Vincent Smit and Dr. Olufemi Olaoye in the group of Prof. Len Barbour in the chemistry department of Stellenbosch University

the sample slices still have the same structure as the bulk (and they indeed still show the metal-to-insulator transition as was shown in figure 2.3).

To enter the insulating phase of high quality UED proof Cu(Me,Br-DCNQI)$_2$ samples, crystals are cooled. To achieve sufficient cooling, our UED system is equipped with a closed cycle helium cryostat. Samples are thermally coupled to the cold finger of the cryostat via a copper braiding, but mechanically decoupled from the helium compressor and expander head. Section 4.1.3 will discuss the problems with sample deterioration upon cooling, which – firstly – are caused by condensation of water molecules onto the sample when operating at cryogenic temperatures. Performing the experiment in an ultra high vacuum helps overcome this problem. Secondly, it is crucial that the samples are cooled at a low, well controlled, cooling rate (< 0.5 K/min), which can be set by the controller of the cryostat system. Despite heat absorption in the cold finger and the copper braiding (which has a large surface area) that thermally connects the cryostat cold finger to the sample mount, a minimum sample temperature of $T_{\text{sample}} \approx 30$ K is achievable, measured with a silicon diode at the bottom of the sample mount. With the phase transition of the system under investigation being at $T_{\text{MI}} = 155$ K, this is more than sufficient.

During the (slow) cool down procedure, electron diffraction patterns are continuously acquired from the cooling samples. This allows tracking of the evolution of contraction or expansion of the sample (observed by shifting Bragg peaks), changes in structure factor (observed by Bragg intensity redistributions) and the appearance of super structures (observed by the appearance of new Bragg peaks) upon cooling. Cool down data on Cu(Me,Br-DCNQI)$_2$ from our UED machine is presented in section 4.1.

3.5.2 Time Resolved Diffraction patterns

Temporal Sampling Once the sample enters the low temperature phase, a time resolved UED experiment can be started. To ensure sufficient sampling in the time domain, temporal time steps in an UED experiment should ideally be much lower than the temporal resolution (1 ps in our case). The mechanical delay stage (labelled in figure 3.1), employed to tune the optical delay between pump and probe pulses, operates at a minimum step size of 2.50 µm. So, every step on the delay stage corresponds to an optical delay of 5.00 µm, which in time corresponds to 17 fs. With smallest stepsizes in this work taken being 250 fs, this is clearly beyond sufficient.

Temporal Overlap To select the appropriate temporal window for an experiment, temporal overlap needs to be determined. Sufficient sampling before 'time zero' ($t < t_0$) ensures effective probing of the starting structural arrangement of the sample. Furthermore, sufficient sampling at $t > t_0$ ensures that all relevant dynamics, including the final structural product, are captured. The most accurate way to determine time zero, is to observe Bragg peak dynamics in a sample upon photo-excitation. However, we utilise the generation of photo-electrons on a grid (as previously shown in figure 3.4a) to determine an estimate of the delay stage position corresponding to time zero (which turns out to be accurate within a single ps). When the optical pulses, which pump the grid, arrive *after* the defocussed electron pulses get to the grid (that is: negative delay times), an unaffected shadow image of the TEM grid is observed. However, when the optical pump pulses arrive *before* the electron pulses (positive delay times), a distortion of the grid is observed. This dependence of the delay stage position on the

observation of the electron beam distortion is shown in figure 3.19, and it is evidently an effective way to determine t_0.

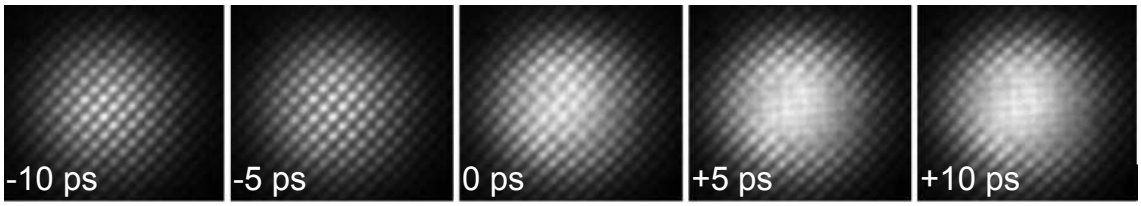

Figure 3.19: An electron shadow image of a TEM grid pumped by a laser pulse, an electron beam distortion observed for $t > t_0$.

Spatial Overlap Fluence calculations and the estimation of the temperature rise in the sample upon pumping in section 3.2 are based on the center of the pump beam overlapping with the center of the sample. Therefore, accurate determination of spatial overlap is necessary. Furthermore, imperfect spatial overlap of the pump beam with the sample would lead to an inhomogeneous intensity profile of the pump on the sample, thereby resulting in inhomogeneous pumping of the sample area. To optimise for the best possible spatial overlap, again the generation of photo-electrons on a grid is employed. Firstly, the defocussed electron beam is aligned such that when it is focussed (by increasing the current through the magnetic lens), the electron beam is focussed through the center of the shadow image of the grid. Once perfect electron beam alignment is ensured, the position of the pump beam spot on the grid (observed by grid distortion due to photo-electrons) is moved (using the final mirror before the vacuum) such that it exactly hits the center of the mesh. Subsequently, the sample position is centered on the focussed electron beam, while neither the pump or the probe alignment are adjusted.

Once spatial overlap is achieved using this method, most of the beam is transmitted through the sample. The transmitted beam hits the surface of the magnetic lens in the vacuum (which can be seen through a vacuum window). The observation of the beam on the lens serves as a (less accurate) confirmation that our beam is indeed going through the sample.

Running the Experiment Before a time resolved UED experiment can be started, the following conditions need to be met:

- The sample has entered the low temperature insulating phase,
- The probe beam electron current has been set appropriately,
- The pump fluence has been set appropriately,
- Spatial and temporal overlap have been optimised,
- The desired starting position of the mechanical delay stage has been determined ($t < t_0$)

All experimental components (the CCD camera, the mechanical delay stage, and a pump beam shutter) are communicating with one LabView program, developed and reported on by Dr. Kerstin Haupt[93]. When the experiment is started, the first pumped image is acquired (an integration time of 30 seconds per image is typically chosen) for

the starting position of the delay stage. When acquisition of the first image is completed, a shutter closes the pump beam, after which an unpumped image is acquired (only one unpumped image is taken for a full temporal sweep). The delay stage then moves one stepsize forward (as chosen by the user), shortening the optical path length of the pump beam line. Image acquisition and the forward movement of the delay stage are then alternated, until the delay stage position corresponding to the final temporal step has been reached[3]. Once the full temporal sweep is finished, the delay stage moves back to its starting position and repeats the identical experiment, until it is interrupted by the user. Many repetitions of the same experiment facilitate the collection of significant signal for temporal signatures close to the noise level. Every few hours, the measurement should be interrupted to check the pump beam fluence and probe beam electron current, and adjustments need to be made accordingly. Spatial and temporal drifts of the pump and/or probe beam are not observed, so the adjustment of either of these is typically not needed during an experiment.

Our best temporally sampled experiment with highest signal-to-noise ran for 30 hours, acquiring a total of 175 temporal sweeps. With an integration time per pattern of 30 s, and a repetition rate of 200 Hz, this corresponds to about $\sim 10^9$ electrons (or 1 nC) for each time step (so $>$10 nC for the whole experiment). During the experiment, the same crystals went through $\sim 20 \cdot 10^6$ repetitions of the observed transition.

[3]The software allows to chose different sampling intervals for different temporal ranges (i.e. small temporal steps around t_0 to resolve fast dynamics, increased stepsize for $t \gg t_0$ for slower dynamics)

4. Results

Being equipped with knowledge of the compelling ultrafast conductivity properties of $Cu(DCNQI)_2$ from chapter 2, combined with the belief that our home-built ultrafast electron diffractometer introduced in chapter 3 has the required specifications to tackle our proposed study on the ultrafast structural dynamics in the material, the experimental results are presented in this chapter. Crucial for the interpretation of the results in this chapter is the expertise to interpret transient diffraction patterns into real space molecular dynamics.

The R_1,R_2-DCNQI compound of choice for ultrafast conductivity studies on $Cu(DCNQI)_2$ systems by Karutz et. al. were dimethyl compounds, a particularly attractive candidate with predictibly adjustable physical properties by increasing deuteration of hydrogens in small, well-defined steps (see section 2.4). For practical reasons, we have opted for Cu(Me,Br-DCNQI)$_2$ as the very first system of this kind to perform UED experiments on. In this compound, the bromine restgroup (which has a smaller volume than CH_3) induces a significantly larger chemical pressure. This pushes the metal-to-insulator transition temperature up to T_{MI} = 155 K, as opposed to $T_{MI} < 80$ K in the various dimethyl compounds. Being able to do UED experiments at higher temperatures aids in negating the significant challenge imposed by working at cryogenic temperatures in ultra high vacuum systems, such as condensation and sample breakage[55][17]. Despite the collapse of the conductive phase in the Me,Br compound not being as dramatic as the one in dimethyl systems (see figure 4.1 – a discontinuous conductivity drop of 'only' >1 order of magnitude), the same superlattice is held responsible for the effect. Therefore, this chemical composition is an ideal compromise for feasible experimental implementation, as it is still the lowest operation temperature in an UED experiment on an organic compound so far (section 3.1).

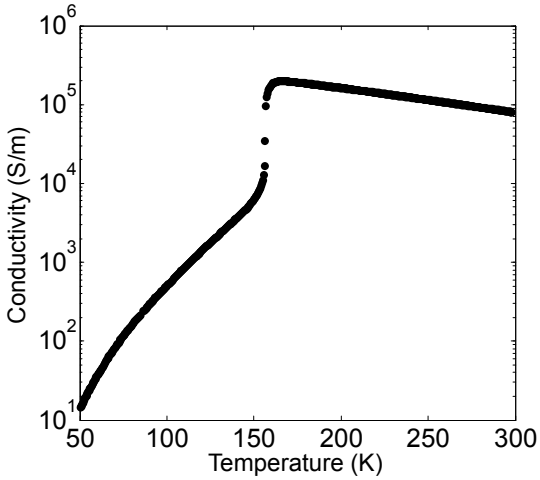

Figure 4.1: Anisotropic conductivity of a Cu(Me,Br-DCNQI)$_2$ bulk needle along the crystal *c*-axis, measured by Florian Hüwe

This chapter will start off by demonstrating the data obtained during the slow cool-down procedure. Our observations upon cooling, and their agreement with previous work, indeed confirms that we enter the insulating phase when below T_{MI}. Secondly, the ultrafast structural response upon photoexcitation, namely the optical lifting of the trimerised superstructure, will be discussed. Lastly, this chapter will conclude with the identification of the ultrafast molecular motions that are responsible for the ultrafast photo-induced transitions, interpreted by comparison of experimentally observed Bragg peak intensity changes with electron diffraction simulations.

4.1 Steady State Cool Down Data

Crystal slices loaded into the ultra high vacuum are cooled at < 0.5 K/min, while electron diffraction patterns are continuously obtained and usually integrated over temperature intervals of 5 – 10 K. This section demonstrates three observations upon cooling: the appearance of the trimerised superstructure, a contraction of the crystal c-axis, and an intensity redistribution of Bragg reflection intensities in the diffraction pattern.

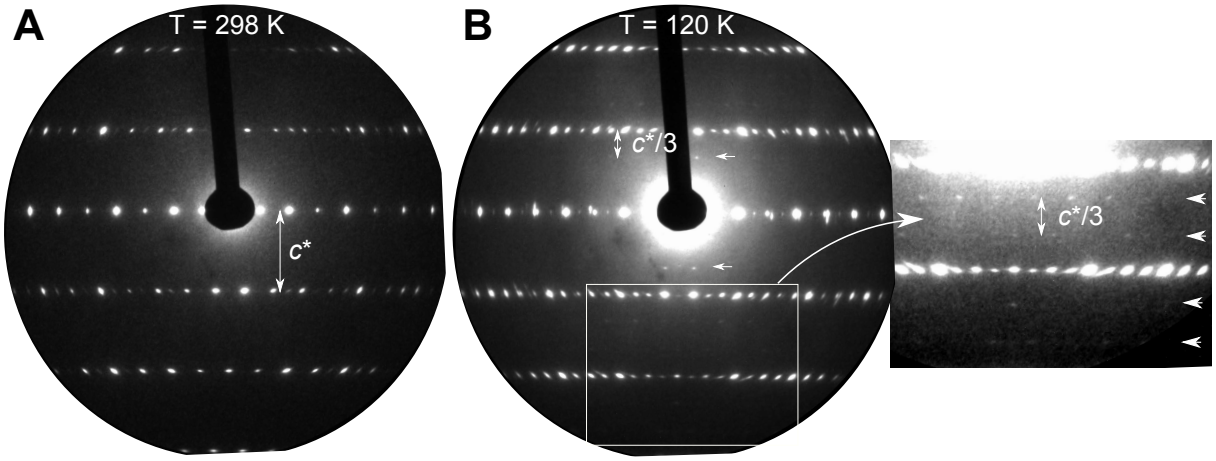

Figure 4.2: (a) A hot (T_{sample} = 298 K) and (b) cold (T_{sample} = 120 K) electron diffraction pattern. Reflections associated with the threefold superstructure are indicated with white arrows. A zoomed in, rescaled, cut-out of the pattern is shown on the right, demonstrating the presence of $c^*/3$ peaks throughout the whole pattern.

4.1.1 Observation of the Superstructure

The most obvious signature of the insulating phase is the periodic lattice distortion, which introduces a threefold periodicity along the c-axis. As explained in chapter 2 and shown in figure 4.2b, this is directly observed in an electron diffraction pattern by $c^*/3$ peaks. The metal-to-insulator transition upon cooling is a discontinuous, first-order, transition. We however, consistently in our 18 cool downs, find that when the $c^*/3$ reflections appear (at a temperature of 145 $\pm$ 10 K), its intensity grows upon cooling – typically over a temperature range of few tens of Kelvin – before levelling off. The FWHM peak width is at the signal-to-noise limit for a quantitative analysis in our Cu(Me,Br-DCNQI)$_2$ samples. In a contaminated Cu(DCNQI)$_2$ sample of

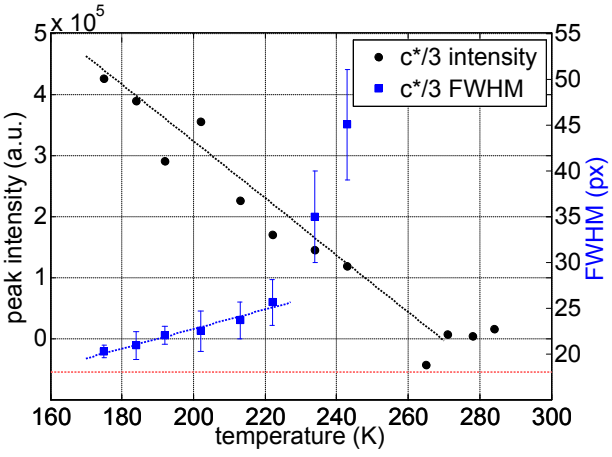

Figure 4.3: The temperature dependence of the integrated intensity (black) and FWHM (blue) of a $c^*/3$ peak in a contaminated sample. The dashed lines are to guide the eye, and the red dashed line indicates the average Bragg peak FHWM (18 pixels).

uncertain composition, which started showing the $c^*/3$ peaks at 240 K, an indication of related peak intensity growth and peak width decrease has been detected in a cool down procedure, which is shown in figure 4.3. This result indicates the growth of trimerised domains below T_{MI} (within the range of our transverse coherence length of about 19 nm) rather than an increase in the trimer modulation amplitude in the crystal lattice.

In an X-ray measurement on Cu(MCl-DCNQI)$_2$ by Moret et. al.[19], the observed $c^*/3$ reflection also increase in intensity upon further cooling below T_{MI}. In seperate X-ray measurements, performed by Kato et. al. on Cu(Me,Br-DCNQI)$_2$[23], the opposite is observed: a discontinuous development of the $c^*/3$ reflections without an amplitude increase upon further cooling is reported. The cooling technique in the latter work, which employed a stream of cold liquid N_2, caused the cooling throughout the entire crystal domain to be homogeneous, explaining the discontinuity.

The inhomogeneous cooling in our sample, due to imperfect thermal contact of the sample to the TEM grid and cold finger, causes the discontinuous instantaneous growth of $c^*/3$ peaks to be 'smeared out' over a larger temperature range. However, the metal-to-insulator transition can still be considered as first order: as discussed in the chapter 2, ESR measurements deduced that a "critical volume" of 20% trimerised sample is required to induce the abrupt conductivity drop (see figure 2.17)[42]. For example, in Karutz' measurement, the conductivity of a bulk needle still drops six orders of magnitude within 1 K upon cooling, despite inhomogeneous cooling through thermocoupling by two contacts at both ends of a bulk needle[43].

4.1.2 Crystal Contraction

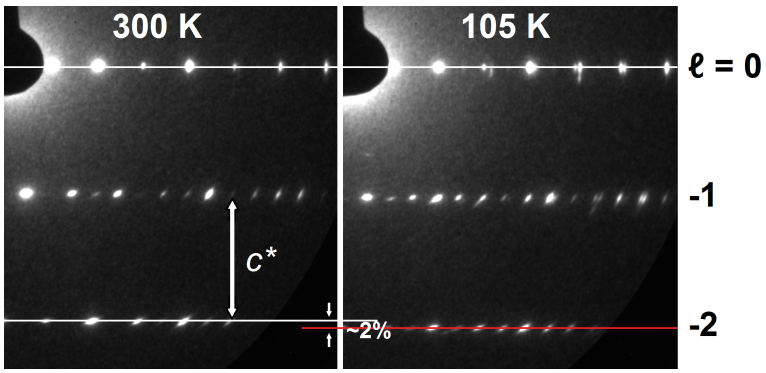

Figure 4.4: The diffraction lines in a cold temperature diffraction pattern (right) are displaced outwardly with respect to the diffraction lines at hot temperature (left), indicated by the displacement of the red line w.r.t. the white line.

An outward shift of the Bragg reflections along the c^*-direction is observed when samples are cooled down: in figure 4.4, the displacement of higher order diffraction lines is clearly noticeable. In a total of 18 cooldowns, an average contraction of the crystal c-axis of $1.65 \pm 0.41\%$ from room temperature to $100 - 130$ K is found, consistent with both Karutz et. al. [43] and Kato. et. al. [23], who report contractions of 2.0 % in deuterated Cu(Me,Me-DCNQI)$_2$, and $1.8\% - 2.1\%$ in Cu(Me,Br-DCNQI)$_2$, respectively. While most of the contraction occurs gradually over the entire temperature range, Karutz reports a sudden contraction of about 0.4 % about 5 K *above* the abrupt

drop in conductivity (that is T_{MI}) in deuterated Cu(Me,Me-DCNQI)$_2$, and Kato also reports a sudden contraction of 0.015 Å (0.4%) for Cu(Me,Br-DCNQI)$_2$, also about 5 K above the end of the metallic phase. Previous X-ray experiments have confirmed that the sudden contraction holds a strong association with the phase transition, as it facilitates the sudden increase of the molecular α angle (by the flattening of crystal layers), confirming the close relationship of the contraction with the distortion of the tetrahedral configuration[23][26]. For example, the X-ray structures of Cu(Me,Br-DCNQI)$_2$ (obtained in the Barbour group) show an increase of 2.87 degrees in alpha from 300 K to 130 K, facilitating the total reduction of the unit cell c-axis by 1.82%.

When tracking the contraction along the c-axis as a function of temperature in our steady state electron diffraction data in our samples, the following behaviours are observed and displayed in figure 4.5:

- In six out of our 18 cooled down samples that show a trimerisation, only a single 'step' (large contraction of up to >1% at a narrow temperature range) is observed. In *all* cases, the trimer appears exactly where the contraction versus temperature flattens off below the step (blue curve in figure 4.5 is a representative example). This happens at a temperature of 144 ± 13 K.
- In six cooled down samples, a gradual contraction along the entire temperature range is observed (red curve in figure 4.5), showing the superstructure at 146 ± 9 K.
- In the remaining six cases, the sample undergoes two steeper contraction steps (black curve in figure 4.5), the second step always less pronounced than the first, with *all* these samples showing a trimer, *always* at the second step (148 ± 9 K).

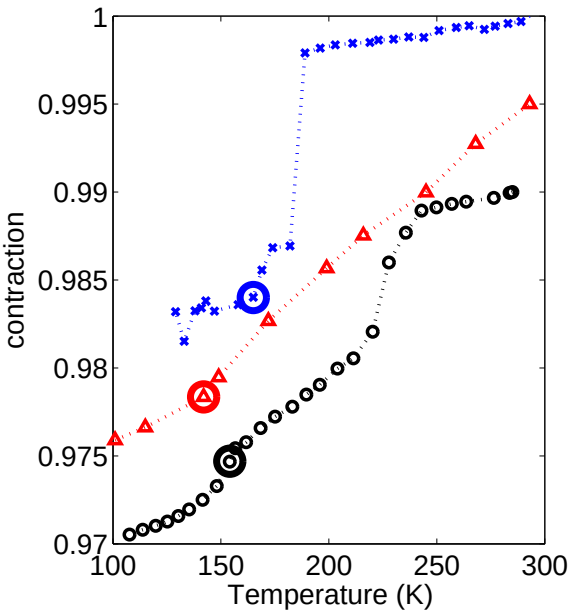

Figure 4.5: Contraction as a function of temperature for three representative samples. Circles indicate the temperature at which the $c^*/3$ reflections first appeared. Graphs have been shifted in y with 0.005 w.r.t. each other.

The three examples in figure 4.5 all fit into the above mentioned categories, but in essence there are a lot of in-between cases (the contraction graphs of all 18 cool-downs are attached in appendix A.2). However, no matter under which of the above three categories a sample falls (or in between which two), the first $c^*/3$ reflection appearance is always associated with an increase in contraction steepness (not always very pronounced, see figures A.5, A.6 and A.7), and always below the largest step, as previously observed by Moret and Kato.

4.1.3 Bragg Reflection Intensities

Changes in atomic arrangements lead to a change in the structure factor, i.e. an intensity redistribution in the diffraction pattern. As previously mentioned, the biggest distortion parameters in this crystal is the molecular angle α (see figure 2.1). To predict the change in structure factor due to the distortion of the tetrahedral structure, and therefore the expected changes observed in our experiment, simulations are done by CrystalMaker and SingleCrystal software. The program allows to visualise and understand diffraction properties of crystals, by simulating electron diffraction patterns from single crystals[94].

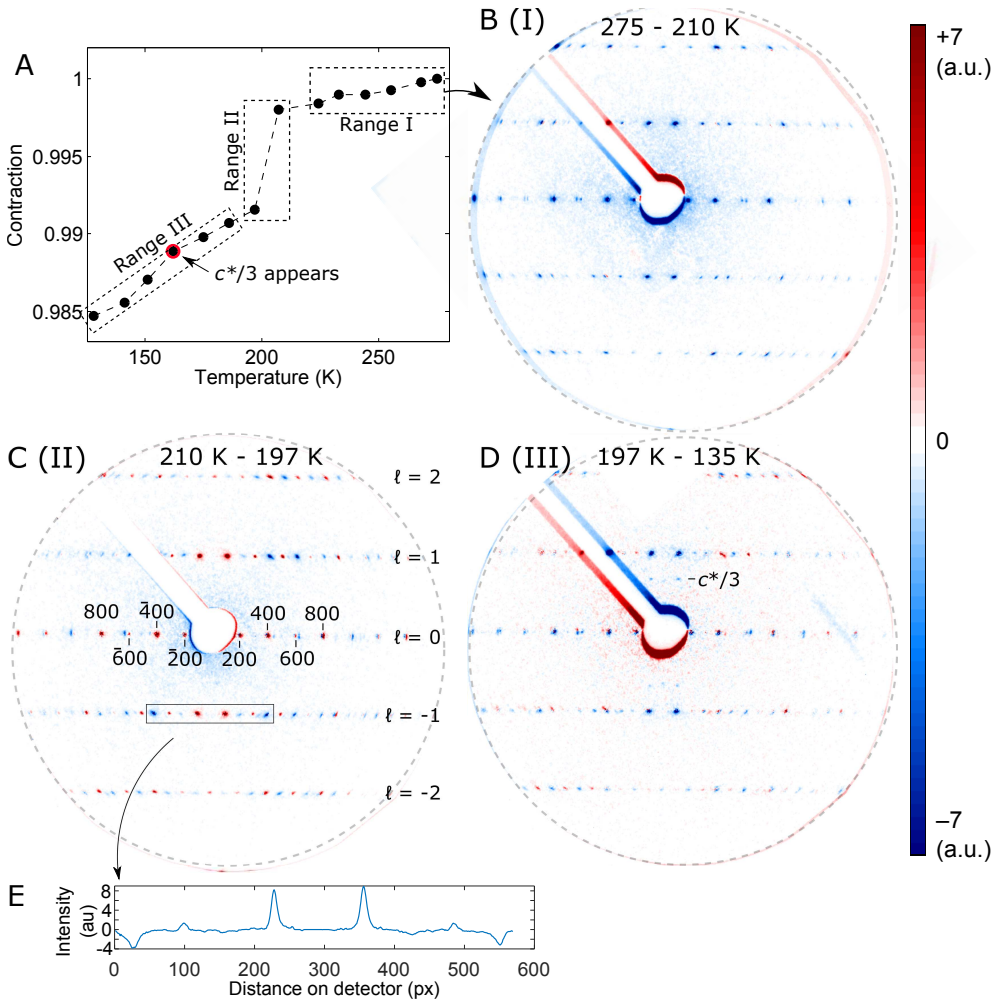

Figure 4.6: (a) The contraction of a Cu(Me,Br-DCNQI)$_2$ sample as a function of temperature. (b) The intensity difference map of the electron diffraction patterns acquired at 270 and 210 K. (c) The difference map of 210 K and 197 K diffraction patterns. (d) The difference map of 197 and 135 K diffraction patterns. (e) An integrated intensity line-out of the selected box, demonstrating the significance with which the difference signals can be obtained w.r.t. the noise.

As an example, a sample that contracts with 1.5% upon cooling from room temperature to 130 K is shown in figure 4.6a. Displayed in fig 4.6b-d are three intensity difference maps corresponding with three contraction ranges: a low contraction slope at high temperatures (range 1), a steep contraction step at 200 K (range 2), and the low contraction slope at temperatures below 200 K (range 3). The diffraction difference maps are created by simply subtracting the average of two diffraction patterns from

each other, each taken at a different sample temperature. Each of these two (steady-state) patterns are an integration over $\sim 5 \cdot 10^5$ shots of $\sim$1 fC each. The colder pattern is subtracted from the warmer pattern: $I_\Delta = I_{\text{hot}} - I_{\text{cold}}$. A blue peak indicates an increase in intensity upon cooling, whereas red indicates a decrease in intensity upon cooling. Contraction along c (that is the outward shift of the diffraction peaks along the c^* direction upon cooling) has been artificially removed such that the Bragg peaks overlap and we isolate the intensity change from the shift. An integrated line-out (figure 4.6e) demonstrates the significance of these difference signals with respect to the background noise.

In the difference map corresponding with the first range (fig. 4.6b), only blue peaks are observed – and nothing else is happening on top of that – which is due to the Debye-Waller effect. The same is observed in the third range (d). The second range, however, shows a characteristic intensity redistribution (c). Two signatures in this intensity difference map are interpreted through electron diffraction simulations:

- The strong red peaks shown in figure 4.6c in the zeroth order diffraction line (ℓ = 0) are a signature of the outward displacement of the Me and Br restgroup, away from the aromatic ring (this will be discussed at the end of section 4.2.2).
- The alternating ('checkerboard') red-blue signature in the higher diffraction orders ($\ell = \pm 1, \pm 2$) are a signature of sample deterioration upon cooling, as will be discussed below.

$Cu(DCNQI)_2$ crystals breaking up when cooled is a well known effect that has been observed and statistically characterised by Pinteric et. al.[17]. In their work, bulk $Cu(DCNQI)_2$ samples were cycled through the metal-to-insulator transitions many times. The more often samples underwent the transition, the greater the chance of the needle losing the transition properties altogether due to breakage. Keeping in mind that the sample contracts 2% along c, which is a big change throughout the entire crystal, it is perhaps not surprising that ultrathin crystal slices (under tension) suffer.

Bragg Intensity Redistribution due to Sample Deterioration In figure 4.7a and b, the measured electron diffraction patterns corresponding to 210 K (just before the step in figure 4.6a) and 197 K (directly after the step in figure 4.6b) are shown. The difference between the two – previously shown in figure 4.6c – is reprinted in figure 4.7c. In order to simulate electron diffraction patterns (figure 4.7d-f), predetermined structure files (which entail all atomic positions within a unit cell, as well as their space group) are necessary. These structure files were obtained for a sample at 300 K and 130 K by the Barbour group through X-ray crystallography. The best-match simulation for the 210 K experimental pattern, making use of the previously obtained 300 K structure file, is shown in figure 4.7d. A simulation based on the 130 K structure file, is shown in figure 4.7e. For both these simulations, the same conditions (the orientation of the sample w.r.t. the electron beam, the sample thickness, and the electron beam coherence) are applied. When comparing figure 4.7e to figure 4.7b, it is evident that the changes from the hot to the cold experimental diffraction pattern are not in agreement with the changes observed in the simulated pattern. The disagreement of the simulated difference map and the experimental difference map (figure 4.7c and f) affirms this conclusion.

The thickness of the sample in the electron diffraction pattern simulations needs to be set to unrealistically low values (around 18-22 Å, which is only a single unit cell,

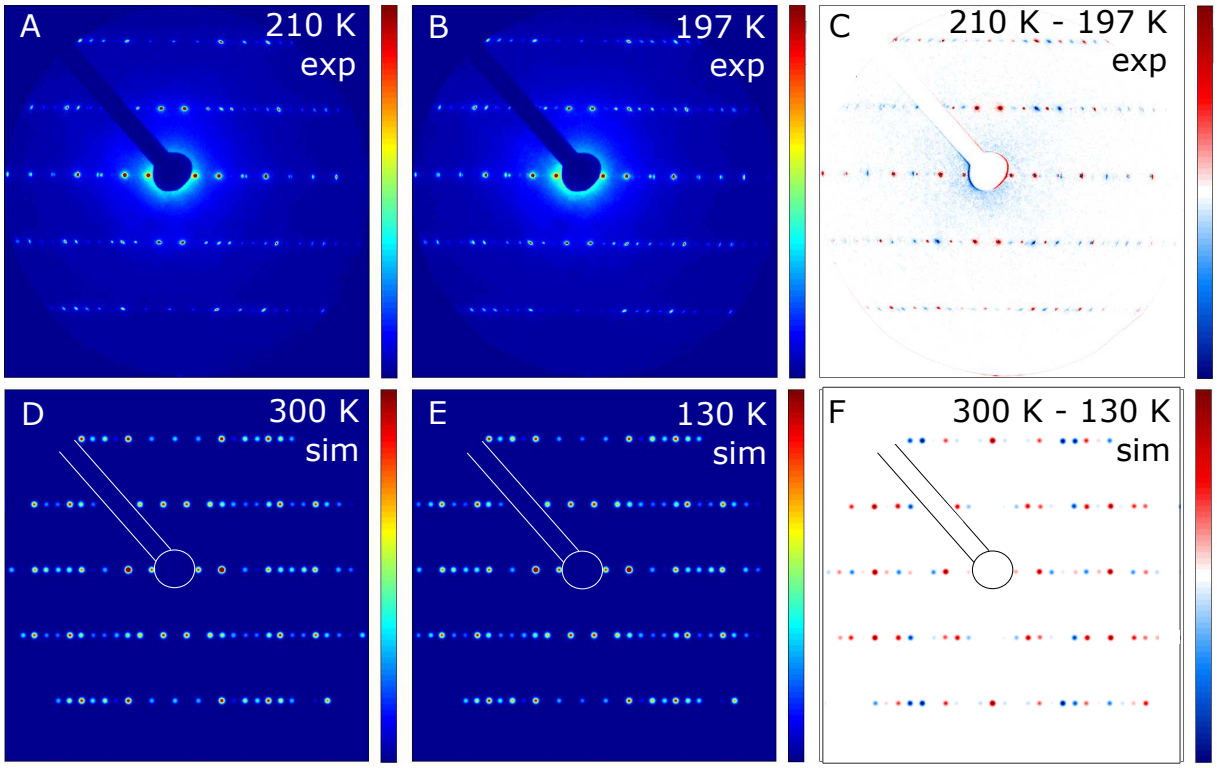

Figure 4.7: (a,b) Measured Cu(Me,Br-DCNQI)$_2$ patterns at 210 K and 197 K, respectively. (c) Intensity difference map $I_{210K\,\mathrm{exp}} - I_{197\,\mathrm{exp}}$. (d,e) Simulated diffraction patterns based on 300 K and 130 K Cu(Me,Br-DCNQI)$_2$ structure file, respectively. (f) Intensity difference map $I_{300K\,\mathrm{sim}} - I_{130K\,\mathrm{sim}}$

while our real samples are 20 times thicker) to get good agreement with experiments. This is necessary, as the software incorrectly assumes the electron beam to be highly coherent. To compensate for real-life imperfect coherence conditions in our experimental electron beam, reducing the sample thickness (and therefore the amount of material to scatter off) diminishes constructive and destructive interference, effectively mimicking conditions of worse coherence.

The most prominent changes in the experimental diffraction signals upon cooling are the following: when the sample is at room temperature, the $2a^*$ peaks (or equivalently $2b^*$ peaks, see figure 4.8 for labels) along the diffraction lines are the strongest. Upon cooling, the diffraction intensity shifts from the $2a^*$ to the $1a^*$ peaks. This 'peak doubling' is explained by worsening coherence conditions. In figure 4.8, a strong case of the peak doubling effect is chosen for illustrative purposes. In figure 4.8a, the ℓ = -2 diffraction line of a pattern taken at room temperature only shows peaks associated with $2a^*$. This is matched with a simulation in figure 4.8b, where a high simulated sample thickness is chosen. Large simulated sample thicknesses improve simulated effective coherence, thereby fully suppressing the 'doubling' peaks. When the sample is

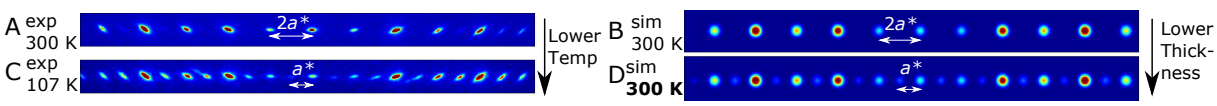

Figure 4.8: (a) Room temperature electron diffraction pattern of Cu(Me,Br-DCNQI)$_2$ (ℓ = -2). (b). Best match simulation, based on 300 K structure file. (c) Electron diffraction of same sample at 107 K. (d) Best match simulation, also based on the **300 K** structure file, confirming that these changes are not due to changes in molecular structure.

(experimentally) cooled, the 'doubled' a^* start to come through, as shown in 4.8c. To reproduce this result in a simulation (fig. 4.8d) the simulated thickness of the sample is reduced to 19 Å (while still using the 300 K structure file), effectively worsening the coherence, causing the doubled peaks to no longer be fully suppressed due to destructive interference.

The observed cooling deterioration in our data complicates the observation of an intensity redistribution directly associated with a change in structure factor due to atomic rearrangement, as this signature is now hidden under damage related changes. Furthermore, the inevitable sample deterioration emphasises the complexity of doing measurements at cryogenic temperatures on delicate organic mono-crystalline 50 nm sample slices, reiterating that Cu(Me,Br-DCNQI)$_2$ with a relatively high T_{MI} is the most suitable compound to do challenging UED experiments on.

c^*/3 Reflections in Simulations In none of the presented simulated electron diffraction patterns so far, the $c^*/3$ peaks are present. Nevertheless, in the X-ray experiments performed at the Barbour group (as well as in Kobayashi's X-ray experiments[18]), the $c^*/3$ peaks were visible, confirming that the sample is indeed in the insulating phase. However, in the structure refinement procedure for X-ray data acquired at T_{sample} = 130 K, the optimised insulating structure always results in a structure file with a space group that does not include the trimerisation. In an attempt to optimise on the new trimerised space group, the sample was cooled further to 90 K, leading to an optimised structure with the correct (trimerised) space group. Unfortunately, due to sample breakage during the cooling procedure, the overall quality of the X-ray diffraction worsened, making the overall structure of the optimised structure file unreliable. It is for this reason, that simulations based on a structure file that includes the trimerisation are not presented in this chapter. This means that molecular arrangement in the T_{sample} = 130 K structure file (which in reality has undergone the trimerisation) is an *average* of the molecular arrangement of the three layers. Unfortunately, the arrangement of the individual 3 layers in the formation of the superstructure are unknown, but the averaged structure is still sufficient to predict changes in structure factor in our time resolved measurements as will be shown in section 4.2.2.

The Insulating Phase of Cu(Me,Br-DCNQI)$_2$ The sudden contraction, and therefore the sudden increase in N–Cu–N angle – the distortion parameter closely linked to the superstructure phase transition – observed in our cool down data, combined with the observation of the superstructure below such a contraction (consistent with previous X-ray experiments) is the indisputable proof that we have entered the insulating phase of our crystal. Photo-exciting the crystal when below T_{MI} (the metal-to-insulator phase transition temperature) is the next step in tracking the ultrafast structural response in the system.

4.2 Ultrafast Structural Response

4.2.1 Response of the Superstructure

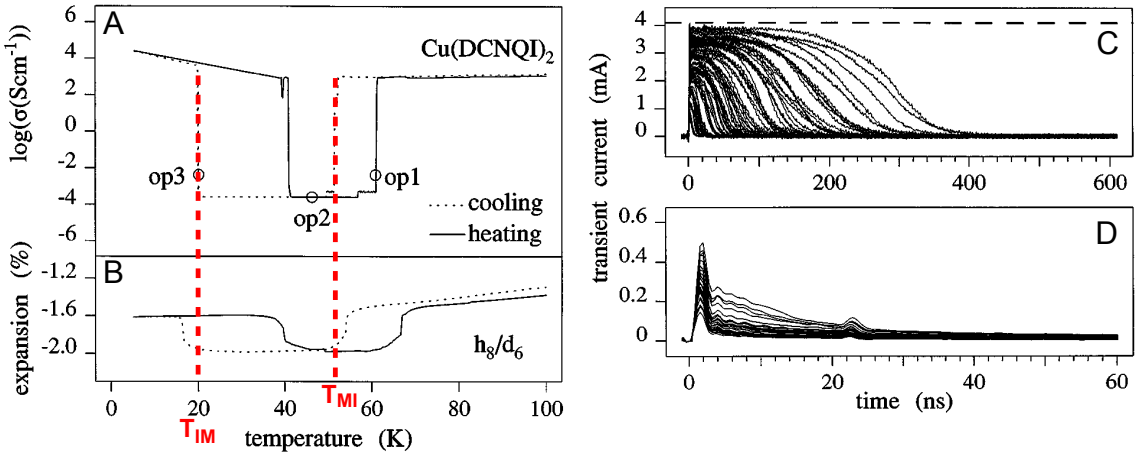

Figure 4.9: The temperature dependent conductivity (a) and expansion (b) for Cu(h_8/d_6-DCNQI)$_2$. The transition temperatures (T_{MI} and T_{IM}) and the operation points (op1, op2 and op3) are indicated. (c) Transient current response of for photo-excitation at 533 nm for op1 (dashed line at 4 mA indicates the current at the fully conductive phase) and for op2 (d). Different plots indicate different fluences. Figure taken from [43].

Before turning to the UED results, we take note of work done by Karutz. et. al., where transient macroscopic conductivity measurements were performed on h_8/d_6-(70%/30%)-Cu(DCNQI)$_2$[1], a compound with T_{MI} = 55 K and a re-entry to the conductive phase at T_{IM} = 20 K[43]. An electric field is applied between two electrical contacts glued to a bulk needle of this compound, with the crystal being optically pumped (with a 30 ps λ = 533 nm laser pulse) at two operation points (see figure 4.9a and b). Firstly, operation point 1 (op1), which is in the hysteresis temperature window and very close to the transition temperature T_{MI}, and secondly slightly below T_{MI} and outside the hysteresis temperature window at operation point 2 (op2). At op1, a full and long lived ($>$ 100 ps) increase of transient conductivity – up to the conductivity magnitude at $T > T_{MI}$ – is observed (figure 4.9c), which is interpreted as a reversed structural Peierls transition. On the other hand, when photo-excited at op2, a short-lived transient current of much lower magnitude is observed (figure 4.9d), which is assigned to 'conventional' short-lived photoelectrons.

Both interpretations for the two short-lived and long-lived switching regimes are indirectly inferred by observing the macroscopic conductivity, and exclusion of other possible mechanisms (such as heating, a pressure wave, and dielectric break down). Furthermore, questions raised regarding the ultimate speed of this transition remain unanswered as the temporal resolution of the transient current measurements is 35 ps.

To unequivocally determine whether the structural phase transition (the lifting of the trimerisation and therefore the closing of the bandgap) has occurred, and to determine whether specific motions are responsible for the completion of the phase transition, we now turn to our ultrafast structural changes observed upon photoexcitation.

[1] a Cu(Me,Me-DCNQI)$_2$ derivative where 70% of the hydrogen atoms in the methyl restgroups are 'normal' hydrogens, and 30% are deuterium.

We utilise an ultrashort laser pulse, which is the output of the NOPA described in section 3.2, to pump the sample at λ = 620 nm – which is within the resonance of the DCNQI cation. In the first experiment, the sample is cooled 40 K below the first appearance of the trimer: $\Delta T_{MI} = T_{MI} - T_{sample}$ = 40 K. This is called **point A**, see figure 4.10. In the second experiment, the sample is cooled 10 K below the first appearance of the trimer ($\Delta T_{MI} = T_{MI} - T_{sample}$ = 40 K), which is called **point B** (see figure 4.10). The temporal response of the $c^*/3$ reflections (as indicated in figure 4.11a) for photoexcitation at point A is plotted in figure 4.11b. Here, we observe that at $t < t_0$, no changes in the $c^*/3$ reflections intensity are observed ($\Delta I/I_0 = 0$). After t_0, these signals completely disappear, but they reappear at later delay times (see inset figures of figure 4.11). The transient data was fitted with the sum of a single exponential decay and a single exponential rise (with each their own time constants τ_1 and τ_2) after t_0, whereas before t_0, the change in the diffraction data is set as zero:

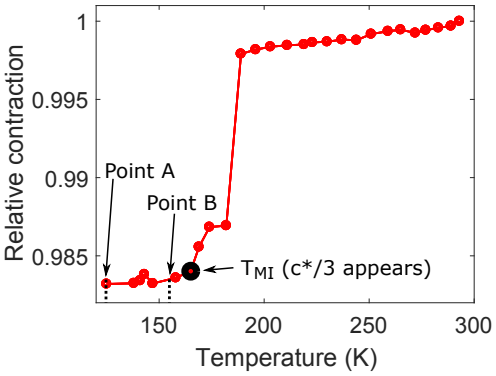

Figure 4.10: A temperature dependent contraction graph, indicating the two temperatures at which the UED experiments were performed (point A and point B) with respect to T_{MI}, the phase transition temperature.

$$\frac{\Delta I(t)}{I_0} = \begin{cases} 0, & \text{for } t < t_0 \\ c_1(1 - e^{-t/\tau_1}) + c_2(1 - e^{-t/\tau_2}), & \text{for } t \geq t_0, \end{cases} \tag{4.1}$$

where c_1 and c_2 are the amplitudes of the decaying and rising exponential function, and τ_1 and τ_2 are the time constants of the decay and the rise time. As discussed in chapter 3, the system response (mostly determined by the electron pulse duration) will lead to the 'rounding off' of sharp temporal features (like the discontinuity of equation 4.1 at $t = t_0$), which means that dynamics happening faster than the system response are smeared out. To account for the system response in our data fitting, the function in equation 4.1 is convoluted with a Gaussian function, whose FWHM is determined by the system response: in this case 1.2 ps for a 1 fC electron bunch (see section 3.3.3). The resulting fit is plotted in figure 4.11b. It is clearly evident that the $c^*/3$ reflections are 100% suppressed within the temporal resolution: a time constant of 1.2 ps is obtained from the data fitting procedure (which serves as an upper limit for the real time constant). The rise time fitted is 6.5 ps.

As the observable here is the super-structure associated with the band gap and the insulating phase, we clearly observe that the crystal turns into the conducting phase within $\sim$ 1 ps by undergoing the reversed Peierls transition, with the insulating phase fully recovering on an ultrafast time scale of 6.5 ps.

Shown in figure 4.11c is a different experiment, conducted at point B. Here, the response of the superstructure is drastically different: upon photo-excitation, the insulating trimerised phase is – again – lifted on an ultrafast time scale, but the photo-induced metallic phase is now optically locked in: the recovery time of the insulating phase is $>$ 100 ps.

As no recovery of the optically suppressed $c^*/3$ reflections is present in this data, it is only fitted with a single decaying exponential without rise:

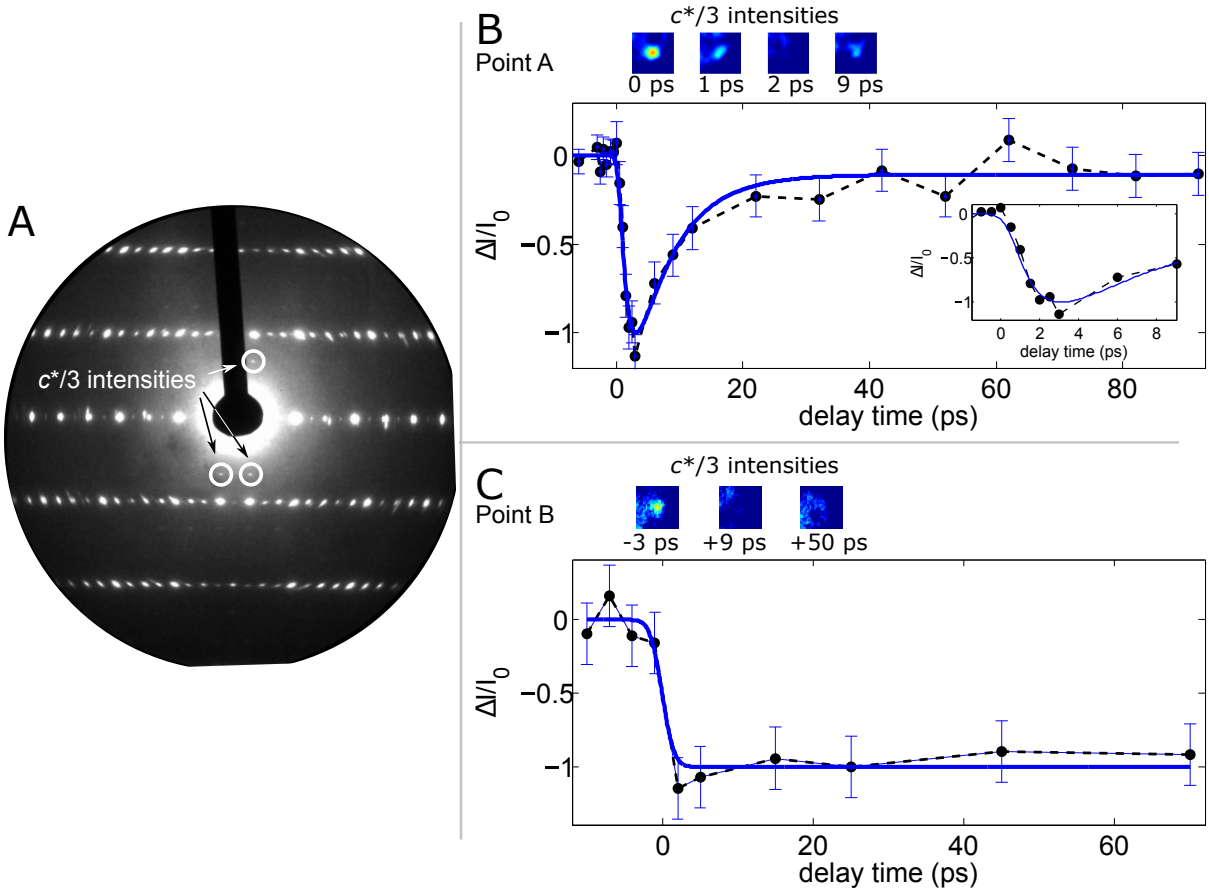

Figure 4.11: (a) The relative intensity change of the $c^*/3$ reflections, as a function of delay time at point A. Inset figures are cut-outs of the trimer peaks for different delay times. Inset plot is a zoom-in in the vicinity t_0. (b) The relative intensity change as a function of delay time for point B.

$$\frac{\Delta I(t)}{I_0} = \begin{cases} 0, & \text{for } t < t_0 \\ c_1(1 - e^{-t/\tau_1}), & \text{for } t \geq t_0. \end{cases} \tag{4.2}$$

No time constants were extracted, as this fit (shown in figure 4.11c) serves as a guide to the eye, as temporal sampling was done in 3 ps intervals. Again, the trimer is 100% suppressed within our temporal resolution.

It is important to mention that the pump fluence for the experiment at point A was set to 1.93 mJ/cm^2, leading to an estimated effective temperature increase of 70 K (see section 3.2 for the fluence and effective temperature increase determination). For the experiment at point B, a pump fluence of 1.02 mJ/cm^2 was used, leading to an effective temperature rise of 36 K. This means that *the effective temperature rise in both experiments causes the samples to end up at approximately the same final temperature (T_{MI} + 20 K)*, but depending on the starting position in the phase diagram, the temporal responses are different.

The full suppression at point B must happen on the same time scale τ_1 as the suppression at point A (where the ultrafast lifting of the trimer is better sampled, with a better system response time) as the same driving mechanisms are responsible for the structural transition. The mechanisms responsible for the $\leq$ 1.2 ps transition in **both** experiments (which leads to the conclusion that τ_1 are the same in both cases) are the following:

- At $t < t_0$, the Periodic Lattice Distortion (PLD), associated with a Charge Density Wave (CDW) is present (both sketched in figure 4.12a).
- For $t > t_0$, upon photo-excitation with a 150 fs laser pulse, the perturbation of the electronic structure smears out the electron density modulation (e^--e^--scattering, figure 4.12b). The time constant for this process for $Cu(DCNQI)_2$ is unknown, but based on previous results on inorganic counterparts it is in the order of $\sim$ 10 fs, much shorter than our temporal resolution.
- In the order of a few 100 fs time constant (still below temporal resolution), the electron energy is transferred to the lattice through electron-phonon coupling, until a thermal equilibrium between the electrons and lattice is reached (figure 4.12c).
- Lastly, well before the next laser pulse arrives 5 ms later, the sample is cooled (through thermocoupling and radiation to the environment) back to its starting state.

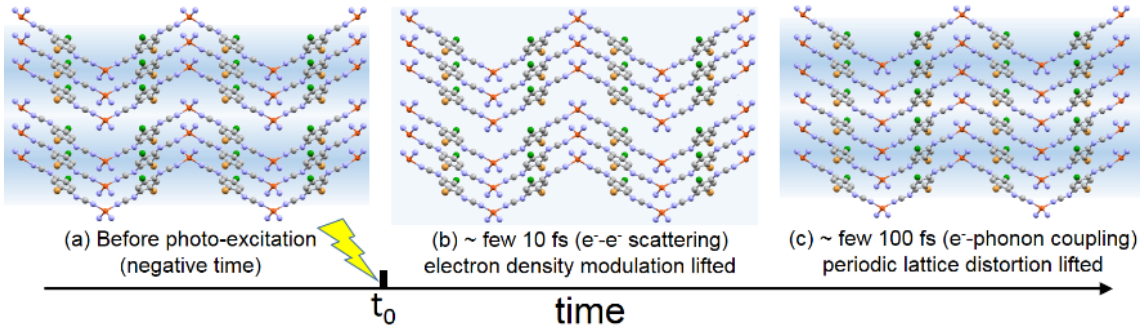

Figure 4.12: Schematic cartoon of processes occurring at times faster than our temporal resolution: (a) The CDW and PLD are present before $t = t_0$, (b) the electronic structure absorbs energy, thereby thermalising the electron gas. (c) Energy is transferred to the lattice, and the PLD is melted. The blue backgrounds illustrate the electron density.

The ultrafast, sub-ps, time scale of the photo-excited lifting of the insulating trimerised phase, as was shown in figure 4.11, reveals the high cooperativity between the electronic and lattice structure in $Cu(DCNQI)_2$, with strong electron-phonon coupling being the responsible switching mechanism.

Superstructure Switching: Two Regimes The kinematics of the $c^*/3$ reflections show two distinctly different behaviours: one where the full metal-to-insulator transition is optically locked in (at point B), and one where the insulating phase is shortly perturbed (at point A). A second UED experiment performed at conditions similar to point B, but on a different sample (while using slightly different experimental conditions) is shown in figure 4.13 (no fits). The good agreement confirms the repeatability of the ultrafast recovery of the optically suppressed insulating phase.

Two distinctive regimes in $Cu(DCNQI)_2$ compounds have been previously observed by Karutz et. al., where for strong excitation values at conditions similar to point B, the sample can be fully switched to high conductivity. In the case of conditions similar to point A, irrespective of the pump fluence (with tested fluence strengths up to the sample damage threshold), the sample can not be fully switched[2]. The transient

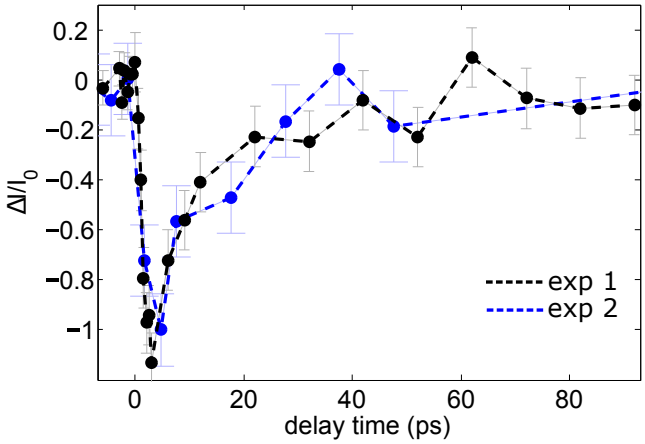

Figure 4.13: Experimental data of $c^*/3$ switching from figure 4.11a (black), plotted with an experiment performed under similar conditions (blue), demonstrating the repeatability of the experiment.

conductivity measurements of Karutz were performed on needles, with thicknesses in the order of 100 µm. With an optical penetration depth of only $\sim$ 100 nm, all light is absorbed in the surface layers of the bulk. Despite this, full conductivity is achieved when pumped close to the phase boundary. The stark contrast between the two switching regimes observed by both Karutz's transient conductivity measurements and our UED experiments, is highly indicative of a threshold switching mechanism. In the one case, the full crystal switches through a cascade effect and the photoinduced conductive phase is long-lived. In the other case, the insulating phase (and in our measurements also clearly the periodic distortion of the lattice) is only shortly perturbed in the first layers upon photo-excitation.

A benefit of doing our UED experiment on 50 nm thick crystal slices, is the homogeneous pumping of the entire crystal volume. When the full surface layer volume is probed in the case of the short-lived photo-induced conductivity increase full suppression, we uncovered that – in fact – a full suppression of the superstructure occurs in this regime, despite the ultrafast recovery thereof. This is in contrast to Karutz, who only observes a minor transient current increase attributed to photo-conductivity and *not* the structural phase transition for conditions similar to point A. However, for their transient conductivity, the temporal resolution was 35 ps (smearing out the transient conductivity response), so the conductivity increase could have been underestimated.

[2]Note that our ΔT_{MI}s of 10 K (point B) and 40 K (point A) are significantly larger than Karutz's ΔT_{MI}s of 5 and 10 K. However, similarity in the two distinctive ΔT_{MI}s is observed due to the phase transition of Cu(Me,Br-DCNQI)$_2$ being at 155 K, 95 K higher than in h_8/d_6-(70%/30%)-Cu(DCNQI)$_2$, effectively scaling up the respective ΔT_{MI}s.

4.2.2 Response of the Structure

Reciprocal lattice information obtained in UED experiments allows for the extraction of real space molecular motions. In this section, two different lattice responses – responsible for the two distinctively different pathways of the transition – are discussed.

The lack of many observable diffraction orders and the absence of phase information in the electron diffraction patterns obtained in UED experiments, limits the real space structural atomic arrangements that are extractable from data, and most certainly does not allow for structural analysis like in X-ray crystallography. However, by utilising priorly known structural knowledge – obtained by steady-state X-ray crystallography – it is still possible to extract changes from a known structure (in our case the real space molecular motions responsible for the different trimer lifting regimes) from UED data. By taking the known structure files as a starting point, and by trying to reconstruct the time resolved electron diffraction intensity changes by doing electron diffraction simulations, we interpret the kinematics of the Bragg reflections (beyond the already interpreted $c^*/3$ reflection) in our UED data.

Electron Diffraction Simulations as a Tool to Interpret UED Data The effect of molecular motions on calculated structure factors (generated with CrystalMaker) are determined using a trial-and-error method (translations of atoms and groups of atoms are guessed), and compared to the experimental intensity distribution. When a feasible solution that fits the experimental data is found, the amplitudes of the corresponding molecular motions are determined by matching the relative Bragg peak intensity change of the experiment with those of the simulations. This is achieved by tuning the amplitude of the motion in the simulation until the simulated relative Bragg peak intensity change is exactly that of the experiment. It should, however, be noted that the extracted numbers serve as an indication of the magnitude of the translations, rather than it being a hard claim of the exact amplitudes.

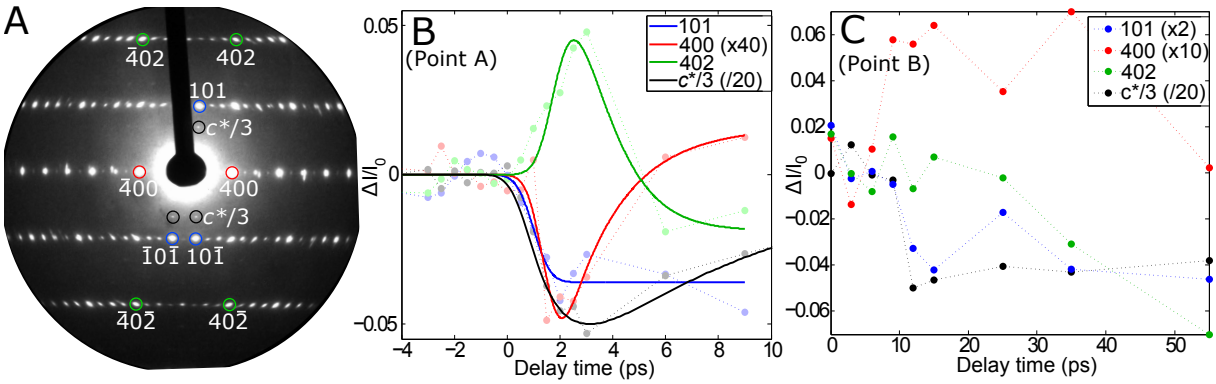

Figure 4.14: (a) Electron diffraction pattern of Cu(Me,Br-DCNQI)$_2$, indicating representative Bragg reflections that demonstrate detectable transient responses. (b) Kinematics of the selected Bragg reflections for the experiment at point A and (c) point B (note different temporal windows).

Bragg Peak Kinematics Bragg reflections that show an ultrafast response upon photo-excitation, by means of an intensity change, are labelled in figure 4.14a. Figure 4.14b and c show the relative intensity changes of those selected peaks for the two measurements. In the first case (point A), the changes observed are short-lived,

as displayed in figure 4.14b. {402} reflections (the combination of $\bar{4}02$, 402, $\bar{4}0\bar{2}$ and $40\bar{2}$ reflections) increase intensity within our temporal resolution, and subsequently decrease in intensity within – again – approximately within our temporal resolution of 1 ps. {400} reflections mirror this behaviour, by decreasing in intensity, and increasing in intensity immediately after. {101} reflections, however, show a long-lived intensity drop.

In the second experimental case (point B) the same reflections show a distinctively different behaviour (figure 4.14c, note the different time window) {400} reflections have a long-lived rise in intensity, whereas the {101} and {402} reflections exhibit a long-lived drop in intensity. For both experiments, the previously shown transient of the $c^*/3$ peaks are also plotted in the respective graphs.

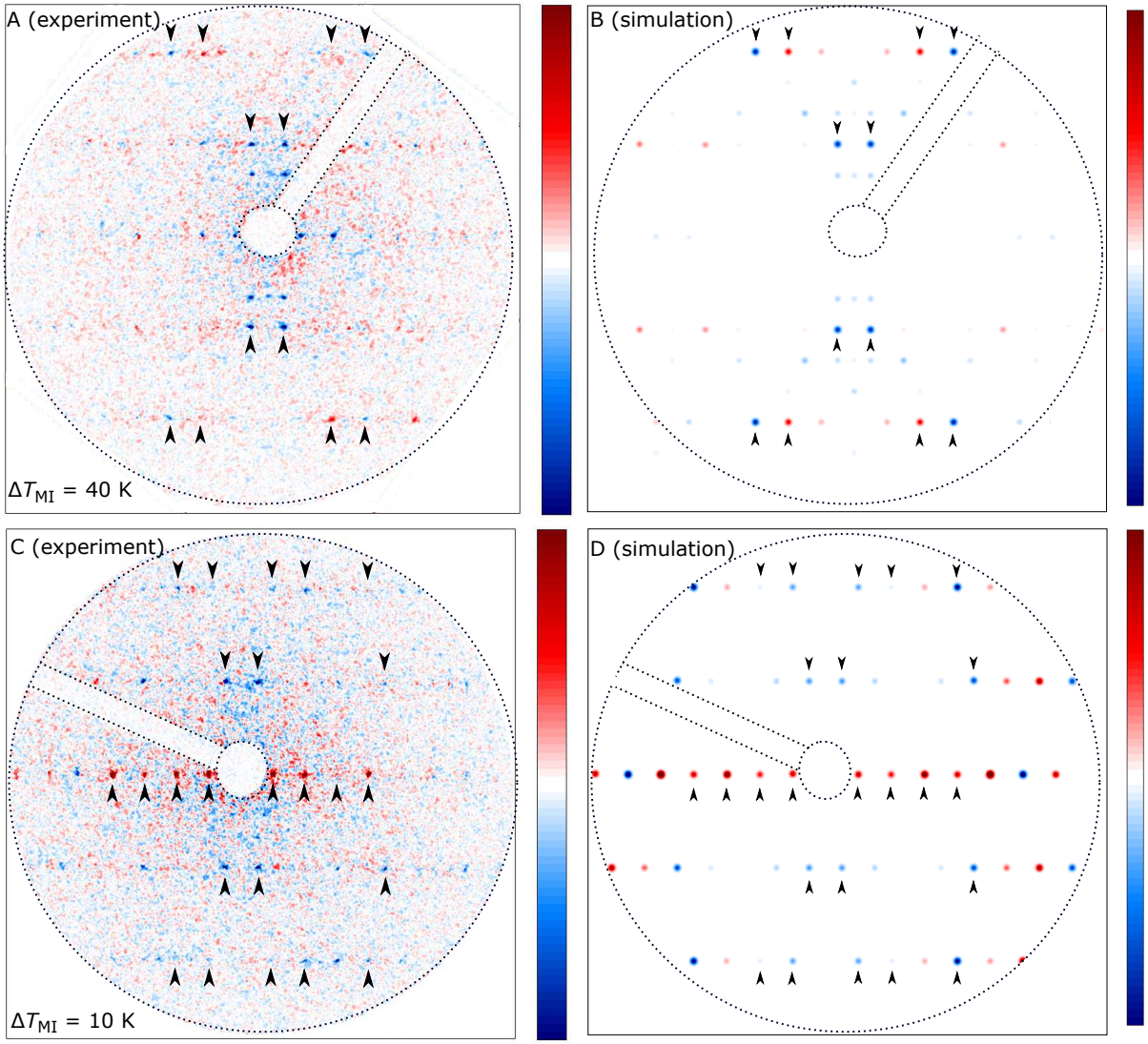

Figure 4.15: (a) Temporal difference map for ΔT_{MI} = 40 K experiment, $I_\Delta = I_{t_0 \leq t \leq 3ps} - I_{t<t_0}$, with (b) the best match structure factor differences, calculated based on displacements of atoms within the unit cell. (c) Temporal difference map for ΔT_{MI} = 10 K experiment, $I_\Delta = I_{t_0 \leq t \leq 80ps} - I_{t<t_0}$, with (d) the best match calculated structure factor changes.

To get a comprehensive overview of the ultrafast response of the intensity distribution along the $\ell = 0, \pm 1, \pm 2$ diffraction lines for both experiments, time resolved inten-

sity difference maps are generated and displayed in figure 4.15 by subtracting the pattern before photo-excitation with the pattern after photo-excitation: $I_\Delta = I_{t<t_0} - I_{t>t_0}$.

Point A The difference map in the case of pumping at point A is shown in figure 4.15a. To generate this image, an average of all patterns taken before t_0 was generated, as well as an average of all patterns for 0 ps $\leq t \leq$ 3 ps. To generate the temporal difference map, the difference between the averaged images was taken. The temporal interval for the averaged image of 0 ps $\leq t \leq$ 3 ps was chosen, as this is the range in which the changes observed in the Bragg peaks are most prominent (as displayed in the graph of figure 4.14b).

The simulated intensity difference map for the translations of atoms (with the known Cu(DCNQI)$_2$ structure from X-ray crystallography taken as a starting point) that resulted in a best match with our experimental data is shown in figure 4.15b. Arrows in figures 4.15a and b highlight the good agreement between calculation and experiment by accentuating the obvious similarities.

Point B The experimental difference map in the second case of $\Delta T_{MI} = 10$ K is shown in figure 4.15c, where in this case *all* patterns taken at $t > t_0$ are included for averaging, as the changes observed in Bragg peaks live longer than the temporal range of the measurement. The best agreement simulated intensity difference map is shown in figure 4.15d.

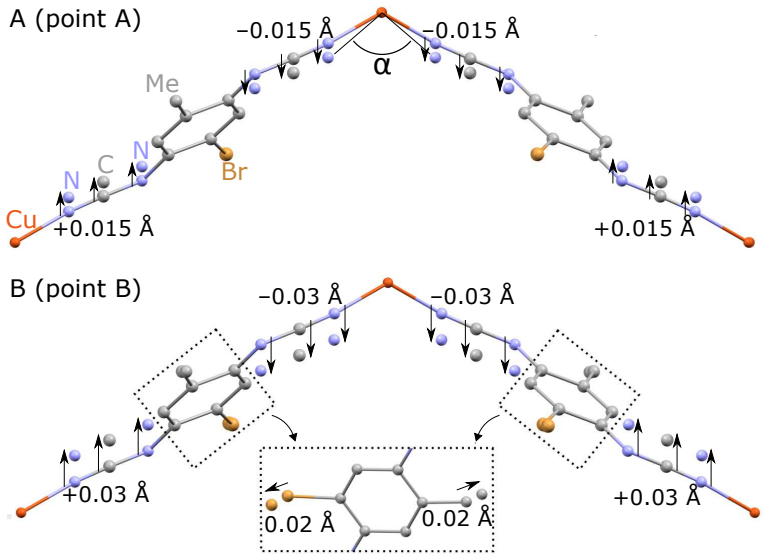

Figure 4.16: (a) The best match simulated short-lived molecular displacements of atoms within a Cu(Me,Br-DCNQI)$_2$ unit cell occurring when photo-excited at point A. (b) The best match simulated long-lived molecular displacement of atoms when photo-excited at point B.

Extracted Modes and their Accuracy Shown in figure 4.16 are the displacements of atoms for the calculated intensity changes that were shown in figure 4.15. In the case of the sample being photo-switched at point A (figure 4.16a), the cyano group (N-C-N chain) attached to the copper and the benzene ring translates $\sim$ 0.015 Å along the c axis, away from the nearest copper (see arrows in figure 4.16a), which decreases the N–Cu–N angle α. The decreased α immediately reverts back to its starting situation,

this all within 4 ps. In the case of photo-excitation at point B (figure 4.16b), an identical translation of the cyano is found – but with an amplitude about twice as big – which is joined by a translation of the CH_3 and Br (R_1 and R_2) of about 0.020 Å, away from the aromatic ring. This new molecular arrangement is stable as no recovery is observed for at least 80 ps.

No minimisation procedures (where all N, C and N's have the freedom to translate individually, all with their own amplitudes) have been implemented to optimise for a best simulation-to-experiment match. Furthermore, the simulated electron diffraction patterns are calculated for a situation where the whole crystal domain is homogeneously trimerised. As it is not known what percentage of the sample has undergone the trimerisation, amplitudes of atomic displacement based on a fully transitioned crystal domain would serve as an upper limit for the real atomic displacements. Nonetheless, the applied translation of the mentioned N, C and N atoms systematically reduces the intensity in the $\{101\}$ and $\{602\}$ reflections only, while it increases the $\{402\}$ reflections only (regardless of the amplitude of the displacement). Furthermore, moving the R_1 and R_2 restgroups (CH_3 and Br) away from the aromatic ring dramatically increases most Bragg reflections in the $\ell = 0$ diffraction order, while it decreases selected peaks in the higher ℓ diffraction orders (the movement of the restgroups displayed in the inset of figure 4.16b is the movement that was chosen to have the best match of simulated Bragg intensity changes with those observed in the experiment at point B[3]). Therefore, the molecular motions suggested in this work serve as an excellent indication as being responsible for the characteristic intensity shifts of a systematic selection of peaks, with two distinct molecular motions (translation of the cyano group, and the translation of the ligands) occurring in the crystal upon photo-excitation for two operation regimes successfully deduced.

Although it was not possible to extract structural information in the cool down data from section 4.1.3 due to the peak-doubling effect as a consequence of sample deterioration, the deterioration leaves the zeroth order ($\ell = 0$) unaffected. The cool-down difference map taken over the discontinuous contraction upon cooling, as was shown in figure 4.6c), also shows a sudden increase of the $\{200\}$, $\{400\}$, $\{600\}$ and $\{800\}$ reflections (similar to the time resolved experiment at point B). This is indicative that the outward translation of the methyls and bromines also occur in thermal equilibrium. Here, however, we have found the order of importance of these motions in a non-equilibrium situation.

[3]Note that for the experiment at point B, the best simulated match with experiments is found by a superposition of the cyano group translation and the R_1, R_2 translation.

4.3 Conclusion

The UED experiments on Cu(Me,Br-DCNQI)$_2$ were performed at two starting positions in the phase diagram. In both cases, the distinct molecular motions that drive the lifting of the three-fold lattice periodicity (within 1 ps, in the entire crystal volume) were identified. Firstly, when photoexcited far below the transition temperature (point A, 40 K below T_{MI}, with a pump fluence corresponding to an estimated crystal temperature rise of 70 K), the trimer is lifted by the translational movement of the cyano groups, which decreases the N–Cu–N angle (α). Due to this decrease in α, the distortion of the tetrahedral crystal structure is reduced. This decreased tetrahedral distortion causes the lowering of energy of the highest Cu 3d level (d_{xy}), which in turn decreases the formal charge of the DCNQIs to below $-2/3e$. In that circumstance, a commensurate trimerisation cannot occur, and the lifting of the trimer within 1 ps is observed (by the disappearance of the $c^*/3$ reflections). However, as there are no other structural modifications that support this reduction in tetrahedral distortion, the tetrahedral distortion relaxes back to the normal situation with a time constant of $\sim$1 ps. The re-establishment of the trimerisation follows with a slightly slower time constant of 6.5 ps, revealing that the tetrahedral distortion governs the trimerisation.

Secondly, when the material is photo-excited just below the transition temperature (10 K below T_{MI}, point B, with the pump fluence leading to an estimated temperature rise of 38 K), an additional outward translational motion of the methyl and bromine groups, on top of the translation of the cyano group (whose amplitude in this case is about twice as big). This additional translation of the subtituents effectively increases the substituent bulkiness. As previously discussed in chapter 2, an increase in R_1,R_2 substituent bulkiness decreases the internal pressure effect, which worsens the thermal stability of the trimerised insulating phase. This situation of a photo-induced increase in R_1,R_2 bulkiness causes an internal pressure drop, which assists the persistent decrease in α. Thereby, the detrimerised metallic phase is optically locked, as it lives for longer than 100 ps.

The presence or absence of this photo-induced internal pressure decrease is responsible for the two distinctly different insulator-to-metal switching pathways (for point A and point B) previously also observed by Karutz et. al. in ultrafast transient conductivity measurements[43] (for op1 and op2, see figure 4.9). There, conventional photoconductivity under conditions corresponding to point A was found upon excitation with a laser pulse, while the full conductive phase was re-established upon excitation at point B.

5. Summary and Outlook

Summary The intriguing physics occurring in organic molecular solids with delocalised π electrons, and the fact that they fulfil functions in biological systems and find applications in electronic devices, has instigated synthesis and experimental exploration of such materials. An example of a useful property is the first-order metal-to-insulator Peierls transition in some Cu(DCNQI)$_2$ (DCNQI: dicyanoquinonediimine) compounds, which is accessible through cooling or increasing (effective) pressure. This dramatic metal-to-insulator transition, which occurs at a material-specific temperature and/or pressure, is caused by the opening of a band gap at the Fermi level due to the creation of a superstructure in the crystal c-axis (which is a trimerisation of the crystal layers) – associated with a Charge Density Wave formation in the electron density. The trend observed is that a decrease in temperature or an increase in pressure brings about a larger distortion of the tetrahedral crystal structure (characterised by the N–Cu–N angle, α). An increase in distortion (which is an increase in α) lifts the energy level of the highest Cu 3d level (d_{xy}), which has hybridised with the DCNQI LUMO (as they both have similar energy levels). The lifting of d_{xy} increases the charge transfer from the Cu to the DCNQI, until it gets to $\delta = -2/3e$. In that situation, a Peierls transition occurs, which opens a band gap at one-third of the LUMO (which is at the Fermi level), turning the material into an insulator.

Interestingly, the reversed transition can be switched with an ultrashort laser pulse. We investigated these photoinduced ultrafast structural lattice dynamics in Cu(Me,Br-DCNQI)$_2$. This study enabled us to directly see the closing of the bandgap through the detrimerisation, and it enabled us to watch the structural dynamics that drive the transition. We chose ultrafast electron diffraction (UED) as our method of investigation, which had proven to be successful for a handful of studies on other complex organic solids. We used our home-built ultrafast electron diffractometer to follow the reversed Peierls transition of monocrystalline Cu(Me,Br-DCNQI)$_2$ slices (thickness of 50 nm) in transmission mode. Pump pulses (which are the output of a noncollinear optical parametric amplifier, with a pulse duration of 150 fs) initiated the insulator-to-metal transition at two positions in the phase diagram: point A (which was 40 K below the phase transition) and point B (10 K below the phase transition). Concurrently, time-delayed ultrashort electron pulses (1.2 ps pulse duration, pulse charge of 1 fC) probed the crystal structure by generating electron diffraction patterns. Hereby, a full transient of all relevant structural dynamics was obtained.

The time resolved UED data for both experiments was compared with electron diffraction simulations. The known structure from X-ray crystallography was taken, and the effect of feasible alterations to this structure on the calculated diffraction pattern were compared with the experimental data. This revealed that the responsible

structural order parameter, the N–Cu–N angle (α), decreases upon photoexcition in both cases, thereby destroying the trimerised insulating phase (observed by the disappearance of $c^*/3$ reflections). At point A, the detrimerised configuration is not stable, and α goes back to its ground state within $\sim$1 ps, while the re-trimerisation follows with a time constant of 6.5 ps. However, when photoexcitation at point B, the decrease in α is assisted by an increase in CH_3 and Br bulkiness, which affects the internal pressure conditions. The presence of this ultrafast, photo-induced, effective internal pressure decrease is required to fully photoswitch, and optically lock, metallic conductivity properties for long times.

Outlook This study has successfully disclosed the molecular dynamics of $Cu(DCNQI)_2$ that govern the sub-picosecond dynamic response by tracking the temporal evolution of the Peierls gap (by lifting of trimerisation) and the associated molecular motions. Despite the studied transition having $\sim$3N degrees of freedom (N=156 atoms in the unit cell of $Cu(DCNQI)_2$), it was possible to isolate distinct molecular motions, which allowed us to view the event on its primary timescales as it occurred. Challenging experiments like these, open up the ability to explore dynamics in other complex molecules, and contribute to a better understanding of the forces at play during phenomena occurring in, for example in this case, fascinating π-orbital systems. Another example possibly suitable for an ultrafast structural dynamics study, are molecular superconductors (e.g. Bechaard salts, $(TMTSF)_2ClO_4$), who lose all electrical resistance below a critical temperature (T_c). It would be interesting to identify the modes that drive the transition to the superconductive phase. The fact that for transitions like these, the evolution of the structural order parameter over time (which in our case was N–Cu–N, α) can be identified and tracked, exposes the possibilities of future studies where an atomic level view of molecular dynamics in solids can aid in understanding the transition mechanisms between states.

With already a handful of challenging UED experiments on organic matter under the belt[95] (not limited to first-order transitions only[96]), the possibility to – in future – investigate dynamics in even larger complex molecular systems, such as proteins, is underlined. An ambitious objective for ultrafast structural dynamics experiments in biological systems is to determine the structure-function correlation, from which we can learn how proteins perform their jobs given to them by Mother Nature[97]. By watching proteins work at their fundamental spatio-temporal limit, the modes occurring in proteins, which are coupled to the reaction forces, can be identified. When successful, the motions that occur for those respective to-be-executed biological functions are identifiable; information that can not be extracted from static structures. Of course, preparing samples suitable for structural dynamics experiments, for example by crystallising them, is a big challenge. Firstly, the synthesis of such crystals is not trivial, and secondly, molecules must not be constrained in such a way that they behave differently in a lattice environment. Therefore, work on organic samples in the liquid or gas phase, although compromising on structural information, might provide the solution in the future. Moreover, reactions in such proteins must have a well-defined start in time, for example by laser-excitation. Technological challenges in these suggested experiments will be the low number of scattering events (in the case of liquids and gasses, where bright electron sources will be needed), and the possible irreversibility

of the (biological) process and therefore the need to perform single shot experiments, as radiation damage may destroy proteins within a single shot. Moreover, structural changes occurring while proteins perform their task may also happen on much slower unknown time scales (ns, µs, or ms). Lastly, a highly coherent electron source is needed to successfully probe the large size of molecular units in the case of proteins. In short, to achieve these ambitious research goals, continuous improvement in sample preparation techniques, as well as continued development of improved ultrashort electron sources, is needed.

Complimentary to ultrashort electron probes for structural dynamics, are the developments in ultrashort X-ray sources from synchrotrons, and more recently X-ray free-electron lasers (XFELs). Two impressive XFELs – at Linac Coherent Light Source (LCLS) at Standford's Linear Accelerator Center (SLAC) and since this year (2017) the European XFEL[98] – are currently operational as a result of large international collaborations. The intensities of X-ray pulses produced in these XFELs are $\sim 10^{12}$ times brighter than those produced by conventional synchrotron light sources. This is a huge advancement, especially for the field of chemical biology, as large and pure single crystals will no longer be required for a beam of such outstanding quality. Many proteins do not form crystals of sizes suitable for X-ray crystallography, or do not perform their main function in a crystal environment. However, in XFEL experiments, poorly diffracting or small crystals can be afforded, or proteins can potentially even be kept in a more natural environment. Although these samples would still suffer from radiation damage upon exposure to X-rays, this might not a problem as the snapshot by the ultrashort X-ray pulse ($\tau \approx 1$ fs) will be taken before the molecule is destroyed (diffract-before-distroy principle). Hereby, acquisition of single shot snapshots during ultrafast reactions, where limitations of crystal size and radiation damage are improved, are achievable[99]. Therefore, this technique – which is currently still in the emerging phase – has the potential to succesfully extend the well-established X-ray crystallography methods (which is the workhorse of structural biology) to the time-resolved femtosecond regime, ultimately enabling the potential to acquire molecular movies of functional biomolecules. Once XFELs have matured, and technological hurdles are out of the way, the technique would still be complimentary to electron source based technologies. Electron diffraction and microscopy techniques have the advantage of being table-top set-ups, and succesful work on ultrafast structural dynamics experiments on organic molecular solids has employed electrons. Furthermore, electrons have three times more elastic scattering events than X-rays (compared to inelastic scattering events), while they deposit about 1000 times less energy than X-rays and therefore have larger sample damage thresholds[100].

With the wide variety of complementary technologies continuously emerging, exciting time-resolved work on organic solids that involve a structure-function relation can be expected in the future, for example molecular movies of protein regulation or the unwinding of DNA[97].

A. Appendix

A.1 Non-Copper DCNQI Radical-Anion salts

$M^{1+}(R_1,R_2\text{-DCNQI}^{\frac{1}{2}-})_2$, where the M^{1+} = Ag^{1+}, Li^{1+}, Na^{1+}, K^{1+}, NH_4^{1+} or Tl^{1+}), all exhibit one-dimensional conductivity along the crystal *c*-axis at room temperature ($\sigma_{RT} \approx 70 - 100$ S/m, except for Li; $\sigma_{RT} \approx 300$ S/m[48]), but are all significantly less conductive than the Cu counterparts ($\sigma_{RT} \approx 700 - 2000$ S/m). The metallic cations are monovalent (1+), resulting in a formal charge of -1/2 of DCNQI. This full charge transfer results in poor electron affinity of the cation, thereby strictly limiting the path of conductivity to the DCNQI chains. This strongly one-dimensional characteristic in non-copper salts leads to a ratio of conductivities parallel and perpendicular to the stacking *c*-axis of 1:5000 (as opposed to ∼1:5 for Cu counterparts). As previously discussed, this strongly one-dimensional behaviour may lead to the stabilisation of a CDW/PLD phase.

Upon cooling, all non-copper compounds undergo a second-order (continuous) metal-to-insulator phase transition at T_{MI} = 70 – 180 K, where the exact temperature depends on the metallic cation (typical curves are shown in figure A.1). Temperature-dependent conductivity measurements on a large variety of the R_1,R_2 substituents (R_1, R_2 = CH_3, Cl, CH_3O, Br and combinations thereof) on non-copper DCNQI salts showed that conductivity, as well as T_{MI}, are rather independent of the variation of these substituents (with the exception of larger CH_3O groups, which lowers the transition temperature, see curve E and F in figure A.1). This is in stark contrast with Cu salt, where the bulkiness of the substituents sensitively governs the N–Cu–N angle (α), which greatly affects the amount of charge transfer and therefore transition temperature. In non-copper salts, however, the metallic cation mostly seems to determine the temperature-dependent conductivity properties. The observed insensitivity of chemical composition of the DCNQI molecule to the material properties is perhaps not surprising, as all these chemical varieties form isomorphous crystals, with no significant changes in structure upon

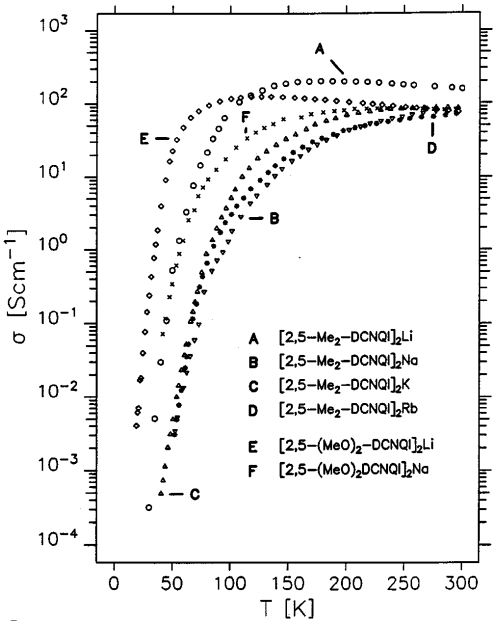

Figure A.1: Temperature dependent conductivity of single crystal $M(2,5\text{-}Me_2DCNQI)_2$ and $M(2,5\text{-}(MeO)_2DCNQI)_2$ for selected M. Figure taken from ref [101].

minor chemical alterations, ultimately resulting in expected similar material properties. The sensitivity of minor adjustments of the ligands of Cu salts is due to the overlap of the DCNQI LUMO with the Cu 3d, which is absent in non-copper salts.

$4k_F$ and $2k_F$ transitions With the DCNQIs having accepted 1/2 electron for most M $\neq$ Cu salts, the band is quarter filled (δ = 0.25), making the material a conductor. If a Peierls transition is responsible for the transition to the insulating phase upon cooling, the opening of a band gap must occur at E_F, which for a quarter filled band is expected at $2k_F = \pi/(2c)$ (equation 2.3). Hence, a tetramerisation is expected. However, a dimerisation was observed in an X-ray diffraction study, corresponding to the opening of a band gap at $4k_F$[19], thereby implying that $\delta = 0.5$. The higher band filling is due to strong electron-electron repulsion, which is explained by the extended Hubbard model (which describes strongly correlated electrons in reduced dimensions)[102].

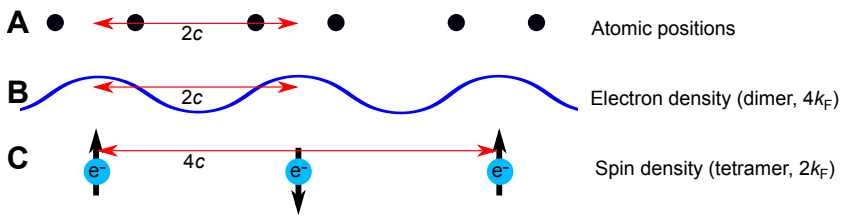

Figure A.2: (a) A dimerised ($2c$) atomic chain. (b) The associated charge density wave, with only one electron per high charge density site (c). At low temperature, the spins are alternating (antiferomagnetic), which an associated spin density period of $4c$

In case of the anticipated (but not occurring) tetramerisation, 4 crystal layers along the crystal c axis would move closer together, thereby grouping two electrons in a site of high electron density in the CDW. However, due to strong electron-electron repulsion within that site (parameter 'U' in extended Hubbard model), combined with electron-electron repulsion from neighbouring sites (parameter 'V'), only one electron is 'allowed' in a site of high electron density. In other words, the strong on-site Coulomb repulsion between electrons split the band into the so-called upper and Lower Hubbard bands. This effectively raises the band occupation from δ=0.25 to δ=0.50, leading to the observed $4k_F$ dimerisation. This dimerisation (sketched in figure A.2a) is associated with a periodic electron density (figure A.2b), with only one electron in each site of high density (figure A.2c). The presence of unpaired electrons (in both conducting and insulating phase) gives rise to paramagnetic properties, observed by high Electron Spin Resonance (ESR) susceptibilities (shown figure A.3b).

The magnetic susceptibilities of Ag(CIM-DCNQI)$_2$ and Ag(BrM-DCNQI)$_2$ (figure A.3b) show a linear dependence at high temperature, with a 'Curie tail' at low temperature (below the Curie temperature, neighbouring spins align, resulting in ferromagnetism). In the case of Ag(DM-DCNQI)$_2$, however, the susceptibility drops at 87 K, which is below the metal-to-insulator transition temperature (T_{MI} = 100 K, figure A.3a). A similar susceptibility drop at low temperature was also observed in Li(DM-DCNQI)$_2$[104]. The reduction of susceptibility, indicative of the vanishing of spin order, is due to the formation of local singlets[105], whereby two unpaired electrons are now paired. This is because at lower temperature, a para-magnetic state is realised, whereby the spins of the unpaired electrons alternate (as indicated in figure A.2c). This ultimately leads to the magneto-elastic coupling of electrons with opposing spins.

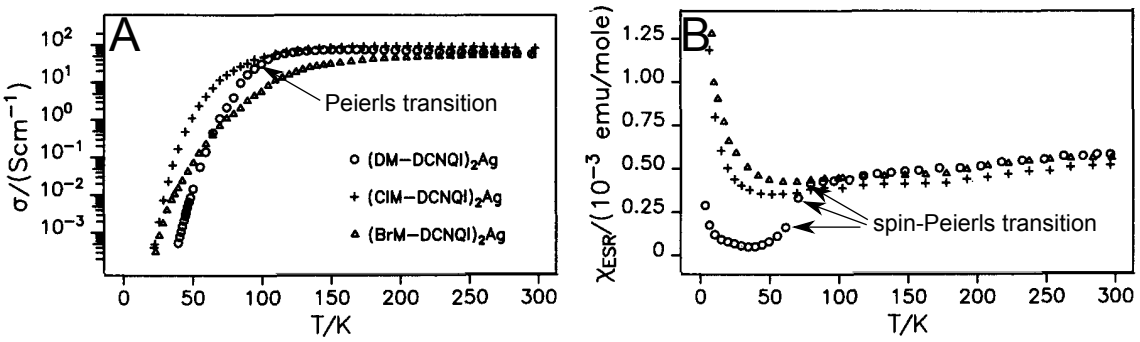

Figure A.3: (a) Temperature dependent conductivity and (b) ESR susceptibility of Ag-salts. Figure adjusted from ref [103].

Now, a 'dimerisation of the dimerisation' (i.e. a tetramerisation) occurs (with electrons forming pairs, with the total spin being zero, making the material non-magnetic), but only if the gain in magnetic energy exceeds the elastic energy required to induce the structural distortion. This magnetic counterpart of a Periodic Lattice Distortion (PLD) formation in a Peierls transition is called a 'spin-Peierls' transition.

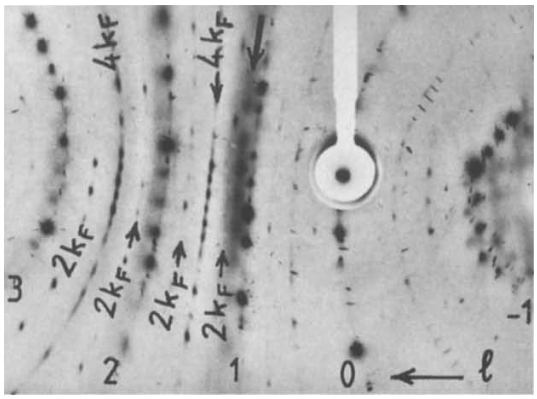

Figure A.4: X-ray diffraction pattern taken of Ag(2,5-DM-DCNQI)$_2$, taken at 20 K, showing a dimerisation ($4k_F$) and tetramerisation ($2k_F$). Figure taken from ref [19]

.

A.2 Contraction upon cooling

As mentioned in section 4.1.2, 50 nm thin Cu(Me,Br-DCNQI)$_2$ crystal slices contract upon cooling. All 18 cool downs that we performed are grouped and plotted in the following three figures:

- Figure A.5 shows the contraction against temperature for cool-downs that show one discontinuous contraction step upon cooling,
- Figure A.6 shows the contraction against temperature for cool-downs that show a continuous contraction upon cooling,
- Figure A.7 shows the contraction against temperature for cool-downs that show two discontinuous contraction steps upon cooling.

The circles in each of the figures indicates the temperature (T_{MI}) at which the $c^*/3$ reflections, associated with the insulating phase of the material, were observed.

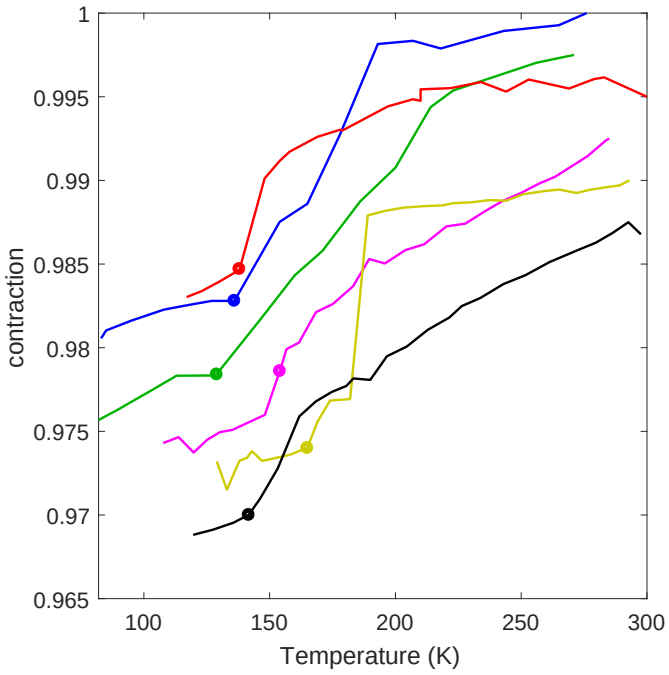

Figure A.5: Six Cu(Me,Br-DCNQI)$_2$ cool-downs that exhibit a single, discontinuous, contraction step of the c crystal axis upon cooling. Circles in plots indicate T_{MI}: temperature of first $c^*/3$ reflection appearance.

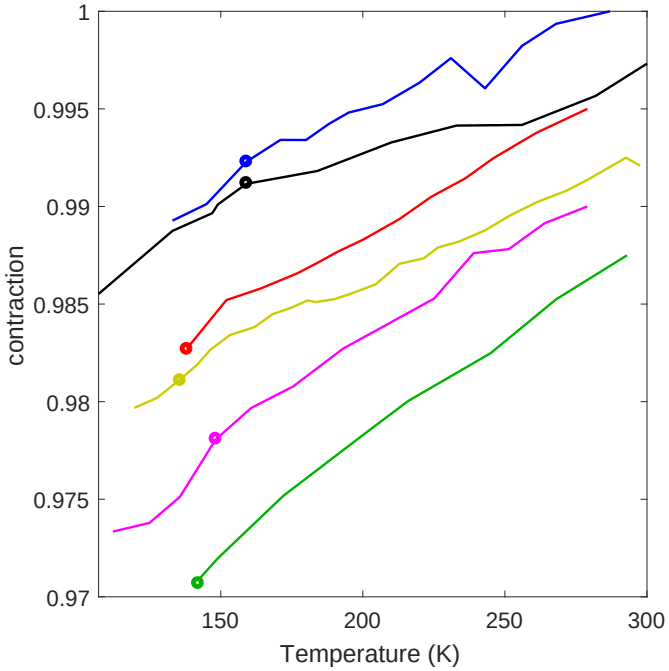

Figure A.6: Six Cu(Me,Br-DCNQI)$_2$ cool-downs that exhibit a continuous contraction of the c crystal axis upon cooling. Circles in plots indicate T_{MI}: temperature of first $c^*/3$ reflection appearance.

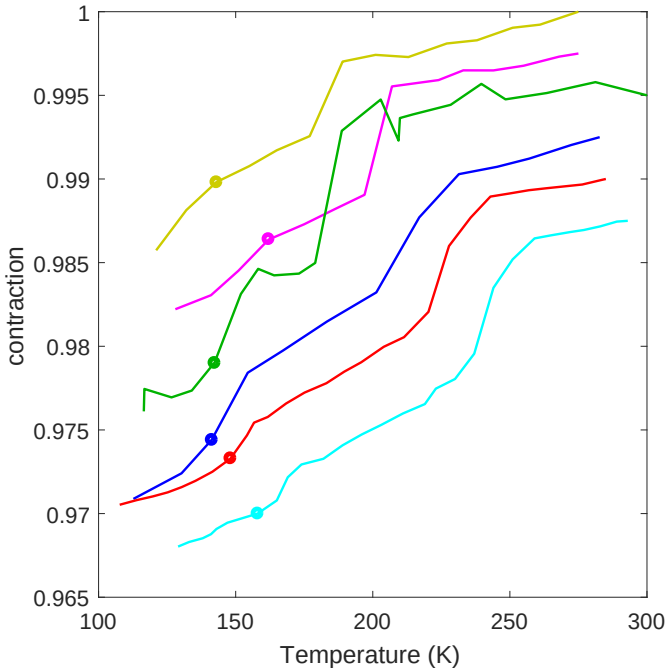

Figure A.7: Six Cu(Me,Br-DCNQI)$_2$ cool-downs that exhibit two, discontinuous, contraction steps of the c crystal axis upon cooling. Circles in plots indicate T_{MI}: temperature of first $c^*/3$ reflection appearance.

Bibliography

[1] Fraxedas, J.: *Molecular organic materials: from molecules to crystalline solids*. Cambridge University Press, 2006.

[2] Vladsinger: Benzene representations. original created by vladsinger, image licensed under the creative commons attribution-share alike 3.0 unported license, original image was cropped and forth 'd' image was added by author. 2009.
Available at: https://commons.wikimedia.org/wiki/File:Benzene_Representations.svg

[3] Desiraju, G.R. and Parshall, G.W.: Crystal engineering: the design of organic solids. *Materials science monographs*, vol. 54, 1989.

[4] Sebastian, L., Weiser, G. and Bässler, H.: Charge transfer transitions in solid tetracene and pentacene studied by electroabsorption. *Chemical Physics*, vol. 61, no. 1-2, pp. 125–135, 1981.

[5] McKeown, N.B.: *Phthalocyanine materials: synthesis, structure and function*. 6. Cambridge University Press, 1998.

[6] Ferlay, S., Mallah, T., Ouahes, R., Veillet, P. and Verdaguer, M.: A room-temperature organometallic magnet based on prussian blue. *Nature*, vol. 378, no. 6558, p. 701, 1995.

[7] Sato, O., Iyoda, T., Fujishima, A. and Hashimoto, K.: Photoinduced magnetization of a cobalt-iron cyanide. *Science*, vol. 272, no. 5262, p. 704, 1996.

[8] Tamura, M., Nakazawa, Y., Shiomi, D., Nozawa, K., Hosokoshi, Y., Ishikawa, M., Takahashi, M. and Kinoshita, M.: Bulk ferromagnetism in the β-phase crystal of the p-nitrophenyl nitronyl nitroxide radical. *Chemical Physics Letters*, vol. 186, no. 4-5, pp. 401–404, 1991.

[9] Kitaigorodsky, A.: *Molecular crystals and molecules*, vol. 29. Elsevier, 2012.

[10] McCoy, H.N. and Moore, W.C.: Organic amalgams: Substances with metallic properties composed in part of non-metallic elements. 2. *Journal of the American Chemical Society*, vol. 33, no. 3, pp. 273–292, 1911.

[11] Akamatu, H., Inokuchi, H. and Matsunaga, Y.: Electrical conductivity of the perylene–bromine complex. *Nature*, vol. 173, no. 4395, pp. 168–169, 1954.

[12] Tanaka, H., Okano, Y., Kobayashi, H., Suzuki, W. and Kobayashi, A.: A three-dimensional synthetic metallic crystal composed of single-component molecules. *Science*, vol. 291, no. 5502, pp. 285–287, 2001.

[13] Jerome, D., Mazaud, A., Ribault, M. and Bechgaard, K.: Superconductivity in a synthetic organic conductor (tmtsf) 2pf 6. *Journal de Physique Lettres*, vol. 41, no. 4, pp. 95–98, 1980.

[14] Law, K.Y.: Organic photoconductive materials: recent trends and developments. *Chemical Reviews*, vol. 93, no. 1, pp. 449–486, 1993.

[15] Thomas, G.A., Schafer, D.E., Wudl, F., Horn, P.M., Rimai, D., Cook, J.W., Glocker, D.A., Skove, M.J., Chu, C.W., Groff, R.P., Gillson, J.L., Wheland, R.C., Melby, L.R., Salamon, M.B., Craven, R.A., De Pasquali, G., Bloch, A.N., Cowan, D.O., Walatka, V.V., Pyle, R.E., Gemmer, R., Poehler, T.O., Johnson, G.R., Miles, M.G., Wilson, J.D., Ferraris, J.P., Finnegan, T.F., Warmack, R.J., Raaen, V.F. and Jerome, D.: Electrical conductivity of tetrathiafulvalenium-tetracyanoquinodimethanide (ttf-tcnq). *Phys. Rev. B*, vol. 13, pp.

5105–5110, Jun 1976.
Available at: https://link.aps.org/doi/10.1103/PhysRevB.13.5105

[16] Aumüller, A., Erk, P., Klebe, G., Hünig, S., von Schütz, J.U. and Werner, H.-P.: A radical anion salt of 2, 5-dimethyl-n, n-dicyanoquinonediimine with extremely high electrical conductivity. *Angewandte Chemie International Edition*, vol. 25, no. 8, pp. 740–741, 1986.

[17] Pinterić, M., Vuletić, T., Lončarić, M., Petukhov, K., Gorshunov, B., von Schütz, J.U., Tomić, S. and Dressel, M.: Mott–peierls phase in deuterated copper-dcnqi systems: a comprehensive study of longitudinal and transverse conductivity and ageing effects. *Journal of Physics: Condensed Matter*, vol. 15, no. 43, p. 7351, 2003.

[18] Kobayashi, A., Kato, R., Kobayashi, H., Mori, T. and Inokuchi, H.: The organic π-electron metal system with interaction through mixed-valence metal cation: Electronic and structural properties of radical salts of dicyano-quinodiimine,(dme-dcnqi) 2cu and (mecl-dcnqi) 2cu. *Solid state communications*, vol. 64, no. 1, pp. 45–51, 1987.

[19] Moret, R.: Structural instabilities in molecular conductors: Silver and copper salts of dicyanoquinonediimine,(dcnqi) 2x (x= ag or cu). *Synthetic Metals*, vol. 27, no. 3-4, pp. 301–307, 1988.

[20] Rossnagel, K.: On the origin of charge-density waves in select layered transition-metal dichalcogenides. *Journal of Physics: Condensed Matter*, vol. 23, no. 21, p. 213001, 2011.

[21] Kittel, C.: *Introduction to solid state physics*. Wiley, 2005.

[22] Peierls, R.E.: *Quantum theory of solids*. 23. Oxford University Press, 1955.

[23] Kato, R., Kobayashi, H. and Kobayashi, A.: Crystal and electronic structures of conductive anion-radical salts,(2, 5-r1r2-dcnqi) 2cu (dcnqi= n, n'-dicyanoquinonediimine; r1, r2= ch3, ch3o, cl, br). *Journal of the American Chemical Society*, vol. 111, no. 14, pp. 5224–5232, 1989.

[24] Bauer, D., von Schütz, J.U., Wolf, H.C., Hünig, S., Sinzger, K. and Kremer, R.K.: Alloyed deuterated copper-dcnqi salts: Phase transitions and reentry of conductivity, giant hysteresis effects, and coexistence of metallic and semiconducting modes. *Advanced Materials*, vol. 5, no. 11, pp. 829–834, 1993.

[25] Sinzger, K., Huenig, S., Jopp, M., Bauer, D., Bietsch, W., von Schuetz, J.U., Wolf, H.C., Kremer, R.K. and Metzenthin, T.: The organic metal (me2-dcnqi) 2cu: Dramatic changes in solid-state properties and crystal structure due to secondary deuterium effects. *Journal of the American Chemical Society*, vol. 115, no. 17, pp. 7696–7705, 1993.

[26] Kato, R.: Conductive copper salts of 2, 5-disubstituted n, n-dicyanobenzoquinonediimines (dcnqis): structural and physical properties. *Bulletin of the Chemical Society of Japan*, vol. 73, no. 3, pp. 515–534, 2000.

[27] Schmeisser, D., Graf, K., Göpel, W., Von Schütz, J., Erk, P. and Hünig, S.: The electronic structure of (2-x-5-m-dcnqi) 2cu. *Chemical physics letters*, vol. 148, no. 5, pp. 423–428, 1988.

[28] Inoue, I., Kakizaki, A., Kobayashi, A., Kato, R., Kobayashi, H., Namatame, H. and Fujimori, A.: Electronic structure of the organic conductor (dme-dcnqi) 2cu studied by photoemission spectroscopy. *Physica C: Superconductivity*, vol. 185, pp. 2691–2692, 1991.

[29] Akaki, O., Chainani, A., Takahashi, T., Kashimura, Y. and Kato, R.: Temperature-dependent core-level x-ray photoemission spectroscopy of the organic conductors (mecl-dcnqi)2 cu,(mebr-dcnqi)2cu, and (di-dcnqi)2cu. *Physical Review B*, vol. 57, no. 19, p. 11846, 1998.

[30] Kobayashi, A., Mori, T., Inokuchi, H., Kato, R. and Kobayashi, H.: The organic π-electron metal system with interaction through mixed-valence metal cation: Electronic and structural properties of highly conducting anion radical salts (2, 5-r1, r2-dcnqi) 2cu (dcnqi= n, n-dicyanoquinonediimine; r1, r2= ch3, ch3o, cl, br). *Synthetic Metals*, vol. 27, no. 3-4, pp. 275–280, 1988.

[31] Tomic, S., Jerome, D., Aumuller, A., Erk, P., Hünig, S. and von Schutz, J.: Pressure-temperature phase diagram of the organic conductor (dm-dcnqi) 2cu. *Synthetic Metals*,

vol. 27, no. 3-4, pp. 281–288, 1988.

[32] Nogami, Y., Date, T., Oshima, K. and Arimoto, O.: Single crystal x-ray study of pressure-induced metal-insulator transition in (dmedcnqi) 2cu. *Synthetic metals*, vol. 86, no. 1-3, pp. 2073–2074, 1997.

[33] Kobayashi, H., Miyamoto, A., Kato, R., Sakai, F., Kobayashi, A., Yamakita, Y., Furukawa, Y., Tasumi, M. and Watanabe, T.: Mixed valency of cu, electron-mass enhancement, and three-dimensional arrangement of magnetic sites in the organic conductors (r 1, r 2-n, n-dicyanoquinonediimine) 2 cu (where r 1, r 2= ch 3, ch 3 o, cl, br). *Physical Review B*, vol. 47, no. 7, p. 3500, 1993.

[34] Hünig, S., Sinzger, K., Jopp, M., Bauer, D., Bietsch, W., von Schütz, J.U. and Wolf, H.C.: Deuterium-induced phase transition of an organic metalan unusual isotope effect. *Angewandte Chemie International Edition in English*, vol. 31, no. 7, pp. 859–862, 1992.

[35] Aonuma, S., Sawa, H. and Kato, R.: Chemical pressure effect by selective deuteriation in the molecular-based conductor, 2, 5-dimethyl-n, n-dicyano-p-benzoquinone immine-copper salt,(dme-dcnqi) 2 cu. *Journal of the Chemical Society, Perkin Transactions 2*, , no. 7, pp. 1541–1549, 1995.

[36] Aonuma, S., Sawa, H., Okano, Y., Kato, R. and Kobayashi, H.: Synthesis of dme-dcnqi-d7 and deuterium-induced metal-insulator transition of (dme-dcnqi-d7) 2cu. *Synthetic metals*, vol. 58, no. 1, pp. 29–38, 1993.

[37] Kato, R., Aonuma, S., Sawa, H., Hiraki, K. and Takahashi, T.: Unexpected isotope effect in 13c-substituted (- c≡ n) molecular conductor (dme-dcnqi) 2cu (dme-dcnqi= 2, 5-dimethyl-n, n-dicyanoquinonediimine). *Synthetic metals*, vol. 68, no. 2, pp. 195–198, 1995.

[38] Hünig, S. and Herberth, E.: N, n -dicyanoquinone diimines (dcnqis): Versatile acceptors for organic conductors. *Chemical reviews*, vol. 104, no. 11, pp. 5535–5564, 2004.

[39] Kobayashi, H., Miyamoto, A., Moriyama, H., Kato, R. and Kobayashi, A.: Suppression of the metal instability and continuous change of the carrier density in (mebr-dcnqi) 2cu1-x li x. *Chemistry Letters*, vol. 20, no. 5, pp. 863–866, 1991.

[40] Yamamoto, T., Tajima, H., Yamaura, J.-I., Aonuma, S. and Kato, R.: Reflectance spectra and electrical resistivity of (me 2-dcnqi) 2 li 1-x cu x. *Journal of the Physical Society of Japan*, vol. 68, no. 4, pp. 1384–1391, 1999.

[41] Kato, R., Sawa, H., Aonuma, S., Tamura, M., Kinoshita, M. and Kobayashi, H.: Preparation and physical properties of an alloyed (dme-dcnqi) 2cu with fully deuterated dme-dcnqi (dme-dcnqi= 2, 5-dimethyl-n, n-dicyanoquinonediimine). *Solid state communications*, vol. 85, no. 10, pp. 831–835, 1993.

[42] Von Schütz, J., Gomez, D., Schmitt, H. and Wachtel, H.: Conductivity without spin-signal, spin signal without conductivity-switchable radical ion salts of deuterated cu (dcnqi) 2. *Synthetic metals*, vol. 86, no. 1-3, pp. 2095–2096, 1997.

[43] Karutz, F., Von Schuetz, J., Wachtel, H. and Wolf, H.: Optically reversed peierls transition in crystals of cu (dicyanoquinonediimine) 2. *Physical review letters*, vol. 81, no. 1, p. 140, 1998.

[44] Sawa, H., Tamura, M., Aonuma, S., Kinoshita, M. and Kato, R.: Charge-transfer-controlled phase transition in a molecular conductor,(dme-dcnqi) 2cu–doping effect–. *Journal of the Physical Society of Japan*, vol. 63, no. 12, pp. 4302–4305, 1994.

[45] Takahashi, T., Yokoya, T., Chainani, A., Kumigashira, H., Akaki, O. and Kato, R.: Cooperative effects of electron correlation and charge ordering on the metal-insulator transition in quasi-one-dimensional deuterated (d m e- d c n q i) 2 cu. *Physical Review B*, vol. 53, no. 4, p. 1790, 1996.

[46] Yamakita, Y., Furukawa, Y., Kobayashi, A., Tasumi, M., Kato, R. and Kobayashi, H.: Vibrational studies on electronic structures in metallic and insulating phases of the cu complexes of substituted dicyanoquinonediimines (dcnqi). a comparison with the cases of

the li and ba complexes. *The Journal of chemical physics*, vol. 100, no. 4, pp. 2449–2457, 1994.

[47] Tajima, H., Aonuma, S., Sawa, H. and Kato, R.: Infrared reflectance spectra of dcnqi salts. *Synthetic metals*, vol. 86, no. 1-3, pp. 2101–2102, 1997.

[48] Mori, T., Inokuchi, H., Kobayashi, A., Kato, R. and Kobayashi, H.: Electrical conductivity, thermoelectric power, and esr of a new family of molecular conductors, dicyanoquinonediimine-metal [(dcnqi) 2 m] compounds. *Physical Review B*, vol. 38, no. 9, p. 5913, 1988.

[49] Tamura, M., Sawa, H., Aonuma, S., Kato, R. and Kinoshita, M.: Magnetic study of metal-insulator-metal transitions in (dme-dcnqi-α, α'-d 2) 2cu. *Journal of the Physical Society of Japan*, vol. 63, no. 2, pp. 429–432, 1994.

[50] Kobayashi, H., Kato, R., Kobayashi, A., Nishio, Y., Kajita, K. and Sasaki, W.: Magnetic susceptibilities of (dme-dcnqi) 2cu and (dbr-dcnqi) 2cu. *Journal of Physics and Chemistry of Solids*, vol. 51, no. 6, pp. 533–537, 1990.

[51] Von Schütz, J., Bair, M., Gross, H., Langohr, U., Werner, H.-P., Wolf, H., Schmeiβer, D., Graf, K., Göpel, W., Erk, P. *et al.*: The conducting salts of n, n-dicyanoquinonediimine (dcnqi). *Synthetic Metals*, vol. 27, no. 3-4, pp. 249–256, 1988.

[52] Gómez, D., Schmitt, H., Von Schuetz, J., Wachtel, H. and Wolf, H.: Pressure and light effects on the phase transition of deuterated cu (2, 5-dimethyl-dicyanoquinonediimine) 2. *The Journal of chemical physics*, vol. 104, no. 11, pp. 4198–4203, 1996.

[53] Schmitt, H., Von Schuetz, J., Wachtel, H. and Wolf, H.: Light, pressure, and stress induced phase transitions of deuterated cu (dcnqi) 2 radical ion salts. *Synthetic Metals*, vol. 86, no. 1, pp. 2257–2258, 1997.

[54] Von Schütz, J., Bauer, D., Wachtel, H. and Wolf, H.: Transient/persistent switching of cu-dcnqi by light and pressure. *Synthetic Metals*, vol. 71, no. 1, pp. 2089–2090, 1995.

[55] Smit, A.B.: *A new femtosecond electron diffractometer for structural dynamics experiments at cryogenic temperatures*. Ph.D. thesis, Stellenbosch: Stellenbosch University, 2014.

[56] Gao, M., Lu, C., Jean-Ruel, H., Liu, L.C., Marx, A., Onda, K., Koshihara, S.-y., Nakano, Y., Shao, X., Hiramatsu, T. *et al.*: Mapping molecular motions leading to charge delocalization with ultrabright electrons. *Nature*, vol. 496, no. 7445, p. 343, 2013.

[57] Liu, L.C., Jiang, Y., Mueller-Werkmeister, H.M., Lu, C., Moriena, G., Ishikawa, M., Nakano, Y., Yamochi, H. and Miller, R.D.: Ultrafast electron diffraction study of single-crystal (edo-ttf) 2 sbf 6: Counterion effect and dimensionality reduction. *Chemical Physics Letters*, 2017.

[58] Jean-Ruel, H., Gao, M., Kochman, M.A., Lu, C., Liu, L.C., Cooney, R.R., Morrison, C.A. and Miller, R.D.: Ring-closing reaction in diarylethene captured by femtosecond electron crystallography. *The Journal of Physical Chemistry B*, vol. 117, no. 49, pp. 15894–15902, 2013.

[59] Ishikawa, T., Hayes, S.A., Keskin, S., Corthey, G., Hada, M., Pichugin, K., Marx, A., Hirscht, J., Shionuma, K., Onda, K. *et al.*: Direct observation of collective modes coupled to molecular orbital–driven charge transfer. *Science*, vol. 350, no. 6267, pp. 1501–1505, 2015.

[60] Jiang, Y., Liu, L.C., Müller-Werkmeister, H.M., Lu, C., Zhang, D., Field, R.L., Sarracini, A., Moriena, G., Collet, E. and Miller, R.: Structural dynamics upon photoexcitation in a spin crossover crystal probed with femtosecond electron diffraction. *Angewandte Chemie*, vol. 129, no. 25, pp. 7236–7240, 2017.

[61] Payne, N.E.: *Studying the structural phase transition of organic Cu(DCNQI)2 with ultrafast electron diffraction*. Ph.D. thesis, Stellenbosch: Stellenbosch University, 2017.

[62] Pedrotti, F.L. and Pedrotti, L.S.: Introduction to optics 2nd edition. *Introduction to Optics 2nd Edition by Frank L. Pedrotti, SJ, Leno S. Pedrotti New Jersey: Prentice Hall, 1993*, 1993.

[63] Huewe, F.: *Electrothermal Investigation on Charge and Heat Transport in the Low-Dimensional*

Organic Conductor (DCNQI)2Cu. Ph.D. thesis, Wuerzburg: Julius-Maximilians-University Wuerzburg, 2017.

[64] Janzen, A., Krenzer, B., Heinz, O., Zhou, P., Thien, D., Hanisch, A., Meyer zu Heringdorf, F.-J., Von Der Linde, D. and Horn von Hoegen, M.: A pulsed electron gun for ultrafast electron diffraction at surfaces. *Review of scientific instruments*, vol. 78, no. 1, p. 013906, 2007.

[65] Kassier, G.H.: *Ultrafast electron diffraction: source development, diffractometer design and pulse characterisation*. Ph.D. thesis, Stellenbosch: University of Stellenbosch, 2010.

[66] Kassier, G.H., Haupt, K., Erasmus, N., Rohwer, E., Von Bergmann, H., Schwoerer, H., Coelho, S.M. and Auret, F.D.: A compact streak camera for 150 fs time resolved measurement of bright pulses in ultrafast electron diffraction. *Review of Scientific Instruments*, vol. 81, no. 10, p. 105103, 2010.

[67] Aidelsburger, M., Kirchner, F.O., Krausz, F. and Baum, P.: Single-electron pulses for ultrafast diffraction. *Proceedings of the National Academy of Sciences*, vol. 107, no. 46, pp. 19714–19719, 2010.

[68] Hommelhoff, P., Sortais, Y., Aghajani-Talesh, A. and Kasevich, M.A.: Field emission tip as a nanometer source of free electron femtosecond pulses. *Physical review letters*, vol. 96, no. 7, p. 077401, 2006.

[69] Ropers, C., Solli, D., Schulz, C., Lienau, C. and Elsaesser, T.: Localized multiphoton emission of femtosecond electron pulses from metal nanotips. *Physical review letters*, vol. 98, no. 4, p. 043907, 2007.

[70] Barwick, B., Corder, C., Strohaber, J., Chandler-Smith, N., Uiterwaal, C. and Batelaan, H.: Laser-induced ultrafast electron emission from a field emission tip. *New Journal of Physics*, vol. 9, no. 5, p. 142, 2007.

[71] Hoffrogge, J., Paul Stein, J., Krüger, M., Förster, M., Hammer, J., Ehberger, D., Baum, P. and Hommelhoff, P.: Tip-based source of femtosecond electron pulses at 30 kev. *Journal of Applied Physics*, vol. 115, no. 9, p. 094506, 2014.

[72] Vogelgesang, S., Storeck, G., Schramm, S., Rossnagel, K., Schäfer, S. and Ropers, C.: Ultrafast low-energy electron diffraction traces phase-ordering kinetics of charge density waves. *arXiv preprint arXiv:1703.10589*, 2017.

[73] van Mourik, M., Engelen, W., Vredenbregt, E. and Luiten, O.: Ultrafast electron diffraction using an ultracold source. *Structural Dynamics*, vol. 1, no. 3, p. 034302, 2014.

[74] Franssen, J., Frankort, T., Vredenbregt, E. and Luiten, O.: Pulse length of ultracold electron bunches extracted from a laser cooled gas. *Structural Dynamics*, vol. 4, no. 4, p. 044010, 2017.

[75] Hastings, J., Rudakov, F., Dowell, D., Schmerge, J., Cardoza, J., Castro, J., Gierman, S., Loos, H. and Weber, P.: Ultrafast time-resolved electron diffraction with megavolt electron beams. *Applied physics letters*, vol. 89, no. 18, p. 184109, 2006.

[76] Li, R., Tang, C., Du, Y., Huang, W., Du, Q., Shi, J., Yan, L. and Wang, X.: Experimental demonstration of high quality mev ultrafast electron diffraction. *Review of Scientific Instruments*, vol. 80, no. 8, p. 083303, 2009.

[77] Murooka, Y., Naruse, N., Sakakihara, S., Ishimaru, M., Yang, J. and Tanimura, K.: Transmission-electron diffraction by mev electron pulses. *Applied Physics Letters*, vol. 98, no. 25, p. 251903, 2011.

[78] Weathersby, S., Brown, G., Centurion, M., Chase, T., Coffee, R., Corbett, J., Eichner, J., Frisch, J., Fry, A., Gühr, M. *et al.*: Mega-electron-volt ultrafast electron diffraction at slac national accelerator laboratory. *Review of Scientific Instruments*, vol. 86, no. 7, p. 073702, 2015.

[79] Mo, M., Shen, X., Chen, Z., Li, R., Dunning, M., Sokolowski-Tinten, K., Zheng, Q., Weathersby, S., Reid, A., Coffee, R. *et al.*: Single-shot mega-electronvolt ultrafast electron diffraction for structure dynamic studies of warm dense matter. *Review of Scientific Instruments*,

vol. 87, no. 11, p. 11D810, 2016.

[80] Musumeci, P., Moody, J., Scoby, C., Gutierrez, M. and Westfall, M.: Laser-induced melting of a single crystal gold sample by time-resolved ultrafast relativistic electron diffraction. *Applied Physics Letters*, vol. 97, no. 6, p. 063502, 2010.

[81] Sokolowski-Tinten, K., Shen, X., Zheng, Q., Chase, T., Coffee, R., Jerman, M., Li, R., Ligges, M., Makasyuk, I., Mo, M. *et al.*: Electron-lattice energy relaxation in laser-excited thin-film au-insulator heterostructures studied by ultrafast mev electron diffraction. *Structural Dynamics*, vol. 4, no. 5, p. 054501, 2017.

[82] Buck, A., Nicolai, M., Schmid, K., Sears, C.M., Sävert, A., Mikhailova, J.M., Krausz, F., Kaluza, M.C. and Veisz, L.: Real-time observation of laser-driven electron acceleration. *Nature Physics*, vol. 7, no. 7, p. 543, 2011.

[83] van Oudheusden, T., Pasmans, P.L.E.M., van der Geer, S.B., de Loos, M.J., van der Wiel, M.J. and Luiten, O.J.: Compression of subrelativistic space-charge-dominated electron bunches for single-shot femtosecond electron diffraction. *Phys. Rev. Lett.*, vol. 105, p. 264801, Dec 2010.
Available at: https://link.aps.org/doi/10.1103/PhysRevLett.105.264801

[84] Siwick, B.J., Dwyer, J.R., Jordan, R.E. and Miller, R.D.: Ultrafast electron optics: Propagation dynamics of femtosecond electron packets. *Journal of Applied Physics*, vol. 92, no. 3, pp. 1643–1648, 2002.

[85] Gao, M., Jean-Ruel, H., Cooney, R.R., Stampe, J., de Jong, M., Harb, M., Sciaini, G., Moriena, G. and Miller, R.J.D.: Full characterization of rf compressed femtosecond electron pulses using ponderomotive scattering. *Opt. Express*, vol. 20, no. 11, pp. 12048–12058, May 2012.
Available at: http://www.opticsexpress.org/abstract.cfm?URI=oe-20-11-12048

[86] Chatelain, R.P., Morrison, V.R., Godbout, C. and Siwick, B.J.: Ultrafast electron diffraction with radio-frequency compressed electron pulses. *Applied Physics Letters*, vol. 101, no. 8, p. 081901, 2012.

[87] Van Oudheusden, T., De Jong, E., Van der Geer, S., t Root, W.O., Luiten, O. and Siwick, B.: Electron source concept for single-shot sub-100 fs electron diffraction in the 100 kev range. *Journal of Applied Physics*, vol. 102, no. 9, p. 093501, 2007.

[88] Gerbig, C., Senftleben, A., Morgenstern, S., Sarpe, C. and Baumert, T.: Spatio-temporal resolution studies on a highly compact ultrafast electron diffractometer. *New Journal of Physics*, vol. 17, no. 4, p. 043050, 2015.

[89] Siwick, B.J., Green, A.A., Hebeisen, C.T. and Miller, R.D.: Characterization of ultrashort electron pulses by electron-laser pulse cross correlation. *Optics letters*, vol. 30, no. 9, pp. 1057–1059, 2005.

[90] Erasmus, N.: *Ultrafast structural dynamics in 4Hb-TaSe2 observed by femtosecond electron diffraction*. Ph.D. thesis, Stellenbosch: Stellenbosch University, 2013.

[91] Flöttmann, K. *et al.*: Astra: A space charge tracking algorithm. *Manual, Version*, vol. 3, p. 2014, 2011.

[92] Halbach, K. and Holsinger, R.: Superfish-a computer program for evaluation of rf cavities with cylindrical symmetry. *Part. Accel.*, vol. 7, no. LBL-5040, pp. 213–222, 1976.

[93] Haupt, K.A.: *Phase transitions in transition metal dichalcogenides studied by femtosecond electron diffraction*. Ph.D. thesis, Stellenbosch: Stellenbosch University, 2013.

[94] Crystalmaker software ltd.. crystalmaker and singlecrystal software.
Available at: http://www.crystalmaker.com/singlecrystal/index.html

[95] Miller, R.D.: Femtosecond crystallography with ultrabright electrons and x-rays: Capturing chemistry in action. *Science*, vol. 343, no. 6175, pp. 1108–1116, 2014.

[96] Miller, R.D.: Mapping atomic motions with ultrabright electrons: The chemists' gedanken experiment enters the lab frame. *Annual review of physical chemistry*, vol. 65, pp. 583–604,

2014.

[97] Sciaini, G. and Miller, R.D.: Femtosecond electron diffraction: heralding the era of atomically resolved dynamics. *Reports on Progress in Physics*, vol. 74, no. 9, p. 096101, 2011.

[98] Altarelli, M., Brinkmann, R., Chergui, M., Decking, W., Dobson, B., Düsterer, S., Grübel, G., Graeff, W., Graafsma, H., Hajdu, J. *et al.*: The european x-ray free-electron laser. *Technical design report, DESY*, vol. 97, pp. 1–26, 2006.

[99] Fromme, P.: Xfels open a new era in structural chemical biology. *Nature chemical biology*, vol. 11, no. 12, p. 895, 2015.

[100] Dwyer, J.R., Hebeisen, C.T., Ernstorfer, R., Harb, M., Deyirmenjian, V.B., Jordan, R.E. and Miller, R.D.: Femtosecond electron diffraction:making the molecular movie. *Philosophical Transactions of the Royal Society of London A: Mathematical, Physical and Engineering Sciences*, vol. 364, no. 1840, pp. 741–778, 2006.

[101] Hünig, S., Kemmer, M., Meixner, H., Sinzger, K., Wenner, H., Bauer, T., Tillmanns, E., Lux, F.R., Hollstein, M., Groß, H.-G. *et al.*: 2, 5-disubstituted n, n-dicyanobenzoquinonediimines (dcnqis): Charge-transfer complexes and radical-anion salts and copper salts with ligand alloys: Syntheses, structures and conductivities. *European Journal of Inorganic Chemistry*, vol. 1999, no. 5, pp. 899–916, 1999.

[102] Lin, H., Campbell, D. and Clay, R.: Broken symmetries in the one-dimensional extended hubbard model. *Chinese Journal of Physics*, vol. 38, no. 1, pp. 1–23, 2000.

[103] Werner, H.-P., Von Schütz, J., Wolf, H., Kremer, R., Gehrke, M., Aumüller, A., Erk, P. and Hünig, S.: Radical anion salts of n, n-dicyanoquinonediimine (dcnqi): Conductivity and magnetic properties. *Solid state communications*, vol. 65, no. 8, pp. 809–813, 1988.

[104] Hiraki, K. and Kanoda, K.: Comparative study on the magnetism and conductivity of (di-dcnqi) 2m,(m= li, cu, ag). *Synthetic metals*, vol. 86, no. 1-3, pp. 2103–2104, 1997.

[105] Hiraki, K. and Kanoda, K.: Wigner crystal type of charge ordering in an organic conductor with a quarter-filled band:(di- dcnqi) 2 ag. *Physical review letters*, vol. 80, no. 21, p. 4737, 1998.